DLR

DEPARTMENT OF SYSTEM ANALYSIS SPACE SEGMENT

Lunar Water Extraction: Design, Optimization, and Development for Future Space Exploration

Author:
Mart Heitkamp
S1585592
462

UNIVERSITY OF TWENTE.

DEPARTMENT OF FLUID ENGINEERING

Colophon

Preface

The inspiration for this study began with a shared desire in extracting water from Lunar regolith, specifically the phase transitions that must occur for successful extraction. During my initial research, I noticed that much of the existing work focused primarily on either the thermal properties of regolith or on simplified sublimation models. This observation opened an opportunity for me to explore and integrate the entire sequence of essential processes—sublimation, deposition, and finally, liquefaction—offering a more complete insight into water extraction on the Moon. This work, therefore, aims to provide a comprehensive model that aligns with LUWEX's standards and demonstrates the functionality of a full-scale process needed for Lunar water extraction.

Only two years ago, I first encountered the world of aerospace. After completing a successful internship at the German Aerospace Center (DLR), I felt the need to return to this field. Fortunately, the University of Twente offered me the chance to advance my Master's education in Mechanical Engineering, which led to my return to DLR for this thesis work. Working within the LUWEX project has been a great opportunity, allowing me to collaborate with fellow researchers invested in the potential of Lunar resources. The chance to be part of such a significant project has been both a privilege and a source of inspiration. As part of this experience, I attended conferences and engaged with the aerospace community. The Space Resources Week in Luxembourg was particularly eye-opening, presenting challenges and insights into the field of Lunar resource utilization. The Space Tech Expo in Bremen also broadened my perspective, gathering experts from across the space industry.

Participating in a large-scale project allowed me to observe and contribute to the development phases that are essential to aerospace engineering, including the experimental phase of the Lunar water extraction system. Being part of the team that built and tested a prototype was challenging. The team encountered design flaws in the setup, pushing me and us to confront new, uncharted territories and unknowns still present in aerospace. Personally, this has been the most rewarding part of my journey—the thrill of contributing to a field where so much remains to be explored.

I would like to express my deepest gratitude to Luca Kiewiet for his invaluable guidance and mentorship throughout my thesis. Working alongside him was not only an educational journey but a thoroughly enjoyable experience. His passion for aerospace and deep expertise as a researcher served as a constant source of motivation. I wish him all the best as he completes his PhD thesis. I am also appreciative of the LUWEX team and colleagues for welcoming me into the project and allowing me to participate in every crucial phase of the water extraction process. Special thanks to Paul Zabel and the SMU-group for giving me the opportunity to return to the German Aerospace Center (DLR) in Bremen, where I gained invaluable hands-on experience. I extend my thanks to Arne van Garrel from the University of Twente for his consistent guidance, insights, and support throughout the duration of my graduation project.

During my time at DLR, I had the privilege of engaging in thorough discussions on aerospace topics with Christoph Kalis and Daniel Reppert. These conversations were not only intellectually stimulating but also fostered a sense of camaraderie. I am truly grateful for their support and for the moments we shared.

Looking ahead, I am optimistic that as LUWEX moves beyond its experimental phase, this study will serve as a foundational piece of evidence proving that Lunar water extraction is not just feasible but can be optimized for future space missions. This project represents a significant step forward in bridging research and practical application in space exploration. Although my journey in aerospace is still relatively new, the past two years have been immensely rewarding and have solidified my passion for the field. I eagerly look forward to continuing this path, contributing my skills, and supporting the future of space exploration.

Summary

Major strides in space technology and exploration have confirmed the presence of water on the Moon, a discovery that has profound implications for sustaining human life and supporting a long-term space environment. Water is vital not only for human survival but also for its potential to generate rocket fuel through electrolysis, a process that separates water into hydrogen and oxygen, which are key components for propulsion. Lunar water exists both as isolated molecules and in the form of ice within the regolith, making it a crucial element of ISRU strategies aimed at creating self-sufficient Lunar bases and enhancing the feasibility of long-term space missions.

The extraction of water from lunar ice involves complex processes, including sublimation, deposition, and liquefaction, each presenting unique challenges. These phase changes must be managed under the extreme conditions of the Moon's environment, where minimal atmospheric pressure, significant temperature variations, and specific material properties can affect the efficiency of water capture and subsequent storage. Strategies for water extraction need to be meticulously designed to address these challenges, ensuring that the transitions between phases are optimised for maximum efficiency and effectiveness.

Sublimation, the process in which solid ice transitions directly to water vapour, poses particular challenges on the Moon due to the extremely low atmospheric pressure. In such an environment, sublimation occurs at a much slower rate unless temperature control is carefully optimised. A key strategy to overcome this challenge involves stirring the icy-regolith mixture, which promotes better heat distribution throughout the sample. As the regolith moves, its effective thermal conductivity increases, leading to faster heat transfer and faster sublimation. The increased particle interactions that result from stirring contribute to a higher sublimation rate. However, the magnitude of these rates does not lead to significant pressure build-up, as even at the maximum sublimation rates, the operational pressures remain below the triple point of water (611.73 Pa). This ensures that the water remains in the vapour phase, preventing unwanted phase transitions. The results summarised in table 10.1 demonstrate the time and maximum rates of sublimation, deposition, and liquefaction under different operational conditions. Sublimation, powered by constant heating, achieves a maximum rate of 252 g/h after 16.4 hours. While this is effective, the challenge of managing the delicate balance between temperature and pressure remains.

Deposition, the reverse of sublimation, where vapour directly transitions into solid ice, was successfully optimised in the cold trap. By carefully tuning the control parameters, the highest deposition rates were achieved, ensuring that the cold trap could match the high sublimation rates from the earlier stage. The 1D model used for this process showed expected behaviour, with the deposition rate stabilising at approximately 50 grams per hour before gradually approaching zero after about 0.7 hours. Given the significant discrepancy between the sublimation and deposition rates, the current cold trap design requires modification. By implementing a larger control volume to mitigate the effects of free molecular flow, the efficiency of connecting sublimation to deposition would be enhanced, leading to optimal water vapour capture. This phase is crucial to ensure that once the maximum ice growth is reached, the delamination process can begin. During delamination, only 7% of the initially deposited ice is lost through sublimation, allowing the remaining 93% to be retained in the liquefaction chamber for subsequent processing.

Liquefaction, the transformation of solid ice back into liquid water, proved to be an efficient process, even at low heat fluxes. The time required for liquefaction was relatively short compared to the time needed to heat the ice to the required phase transition temperature. However, achieving this phase transition more efficiently can be further improved by increasing the power input during liquefaction or enhancing the thermal properties of the liquefaction chamber. One effective solution involves polishing the copper inlay inside the chamber to increase its surface emissivity, which improves heat transfer and accelerates the liquefaction process.

Overall, these results highlight the successful management of sublimation, deposition, and liquefaction processes, even under the extreme conditions of the Lunar environment. The optimised strategies not only enhance the efficiency of water extraction but also provide valuable insights for the development of future systems aimed at harvesting water from the Lunar surface. The continuous refinement of these processes, particularly through careful control of heat fluxes and surface properties, promises to further improve the performance of water extraction systems, ensuring their viability for long-term Lunar exploration.

Contents

Nomenclature

Abbreviations

LUWEX	Validation of Lunar Water Extraction and Purification Technologies for In-Situ Propellant and Consumables Production
DLR	Deutsches Zentrum für Luft- und Raumfahrt / German Aerospace Center
ISRU	In-Situ Resource Utilization
SMU	Synergetic Material Utilization
UT	University of Twente
WES	Water Extraction System
LWES	Lunar Water Extraction System
WCS	Water Capturing System
WLS	Water Liquefaction System
PSR	Permantly Shadowed Region
TVAC	Thermal Vacuum Chamber
COMSOL	Comsol Multiphysics Software
MATLAB	Matlab / Mathworks
CFD	Computational Fluid Dynamics
PCI	Phase Change Interface

Physics Constants

G	Gravitational constant	$6.67430 \times 10^{-11}\,\mathrm{m^3\,kg^{-1}\,s^{-2}}$
c	Speed of light in a vacuum	$299\,792\,458\,\mathrm{m\,s^{-1}}$
h	Planck constant	$6.62607015 \times 10^{-34}\,\mathrm{J\,Hz^{-1}}$

Number Sets

$\mathbb{H}$	Quaternions
$\mathbb{C}$	Complex numbers
$\mathbb{R}$	Real numbers

List of Figures

List of Tables

1 | Introduction

The celestial body closest to Earth, the Moon, has captivated scientific interest for centuries. Recent advances in space exploration have revealed the presence of Lunar ice. This ice, may have resided on the Moon for millions or even billions of years. The significance of this discovery extends beyond its scientific intrigue; it holds profound implications for future manned Lunar exploration.

A proposed robotic sample return mission emerges as a pivotal undertaking in bringing Lunar ice back to Earth for study. The potential subsequent human mission aims for more detailed sampling, guiding humanity in an era of interaction with this Lunar resource. The mere existence of Lunar ice provides a unique opportunity for scientists to refine models elucidating the impacts on the Lunar surface.

1.1 Problem Statement

The allure of Lunar ice transcends its scientific implications, delving into the realm of practicality for future human Lunar endeavours. The Moon stands as a dangerous landscape without water sources, making the transport of water from Earth economically unfeasible, with costs of up to 100000 euros per kilogramme NASA [2020]. Consequently, Lunar ice deposits become a strategic and invaluable resource, potentially earmarked as

"the most valuable piece of real estate in the solar system,"

according to [Feldman, 1998]. As the exploration of Lunar ice progresses, it becomes connected with the evolution of space technologies and a growing understanding of the Lunar environment. The last decade has brought forth revelations about the presence of water on the Moon, highlighting its pivotal role as a crucial resource for supporting human life and enabling sustainable space exploration. In this context, the development of In-Situ Resource Utilisation (ISRU) technologies becomes essential, with Lunar water being a potential resource for deep space missions.

Extracting water from the Lunar surface opens up possibilities for splitting it into hydrogen and oxygen through electrolysis, crucial components for rocket propellants. Thermal water extraction involves applying heat to Lunar regolith to sublimate the ice within. Past studies demonstrate the feasibility of water extraction from Lunar regolith by modelling the Lunar regolith-ice mixture as a porous medium [Piquette et al., 2017, Brisset et al., 2020, Kiewiet et al., 2022, Cole et al., 2023, Wasilewski, 2021b], forming the baseline for this thesis.

This research aims to optimise Lunar water extraction systems by examining the interconnected processes of heat transfer, sublimation, ice deposition, and liquefaction. A primary focus is placed on the efficient design and integration of thermal and phase transition mechanisms necessary to capture, convert, and store water in a form usable for life-support systems and fuel synthesis on the Moon. Central to this objective is the development of multi-physics models capable of simulating the parameters that impact each phase transition process. These models leverage advanced Computational Fluid Dynamics (CFD) to explore the flow behaviour of water vapour, heat transfer, diffusion properties, and the dynamics at the ice-vapour interface, all crucial factors for effective extraction of water from Lunar regolith.

The experimental component of the project faces inherent scheduling constraints, as each stage of testing involves prolonged heating times due to the low thermal conductivity of Lunar regolith. Initial studies and experiments underscore this limitation, highlighting the need for design innovations that can mitigate the duration of heating. An enhancement to the extraction design introduces a mechanism for the agitation of regolith particles, substantially reducing heating time by improving effective thermal conductivity through particle movement. This movement aids in reaching the sublimation threshold temperature more rapidly, allowing the solid ice within the regolith to transition into water vapour. Following successful sublimation and outgassing, the water vapour must then be captured, with the final objective being the efficient transition to a liquid state for astronaut use and other mission-critical applications. Given the primary focus on producing liquid water, the study excludes water capture in the gaseous state.

The models developed in this research serve as predictive tools for identifying parameters with the most significant influence on each stage of water extraction. Through iterative refinement of these parameters and experimental validation, the study seeks to yield an optimised extraction system ready for deployment in Lunar exploration missions. A critical challenge within this investigation is the unique and extreme environment of the Moon, especially within the permanently shadowed regions (PSRs) at the Lunar poles where water ice is most abundant. These regions exhibit near-cryogenic temperatures, which significantly impact both the design and operational capacity of any ISRU technology deployed. Furthermore, the reduced Lunar gravity—approximately one-sixth of Earth's gravity—presents additional constraints on material handling and fluid dynamics. This research addresses these environmental factors in the optimisation of ISRU technology, focusing on enhancing the feasibility and reliability of a Lunar water extraction system suitable for long-term space exploration.

1.2 Objective

The primary objective of this work is to model and simulate three distinct phase transition processes—sublimation, deposition, and liquefaction, within the framework of thermal water extraction methods using COMSOL Multiphysics. This study aims to evaluate each process against a performance metric developed to provide insights into their efficiency and potential improvements. By systematically analysing the impact of design choices, operational parameters, and material properties, this work seeks to improve these processes and propose design recommendations aligned with the LUWEX standards. The corresponding research question guiding this thesis is as follows:

> **What strategies can optimise the efficiency of sublimation, deposition, and liquefaction processes in thermal water extraction systems, considering design, operational, and material factors to enhance overall performance according to LUWEX standards?**

By addressing this question, this study will contribute to a deeper understanding of the underlying mechanisms of the thermal extraction process and provide a structured approach to improving the efficiency of water extraction systems through modifications and optimised process conditions.

1.3 Research Methodology

The ISRU value chain depicted in Fig. 1.1 illustrates a staged process for extracting, processing, and utilising resources, such as water, found on the Moon, specifically in the PSRs of the Lunar South Pole. This chain, composed of five key steps, outlines a structured approach to transforming raw Lunar materials into consumable resources to support long-term human presence and other mission objectives. Each stage is sequential, ensuring that resources are systematically prepared for end-use. The Lunar South Pole represents the resource location, specifically, the PSRs which are known to contain substantial deposits of water ice. The choice of the Lunar South Pole is strategic

due to the presence of water-ice in these shaded craters, where temperatures remain extremely low. Now that this location has established, one needs to pre-process the material to eventually extraction solely water-ice. Pre-processing involves excavation. Technologies for excavation are employed to retrieve the ice-bearing regolith. Robots, drilling rigs, or other machinery may be used to break through the surface and gather the material. The refinement stage focuses on separating water ice from other elements and particles within the regolith. During this phase, the extracted material is processed to isolate the water content.

After successful excavation and refinement, the extraction stage is where heat is applied to the refined material to convert ice into water vapour, facilitating its capture and conversion into liquid water. In this phase, optimising the thermal conductivity and controlling the temperature gradients are crucial because they affect the speed and efficiency of extraction. Additionally, handling and containment systems are designed to prevent water loss during phase transitions. This thesis specifically centrers on thermal extraction methods. Alternative water production approaches, such as the hydrogen reduction of Lunar regolith [Sargeant et al., 2021], are briefly mentioned in Chapter 4 but are not subject to in-depth investigation. The same is applicable to specific heating methods for thermal extraction, which are briefly introduced in Chapter 2 and 4.

The final step involves making the extracted water available for various applications, such as life support or fuel production. Once captured and converted, water enters the supply chain for Lunar infrastructure. It can be stored for drinking, converted into oxygen for breathable air, or electrolysed to provide hydrogen and oxygen for rocket fuel. The entire ISRU value chain can be viewed as a specialised supply chain tailored to space exploration. Each step represents a critical link in the chain, where efficient transformation from one stage to the next are paramount to minimising waste and optimising resource yield. Thus, innovations in extraction, refinement, and thermal processing are essential to make this chain viable for long-term Lunar habitation and mission success. This research follows a systematically organised framework, commencing with
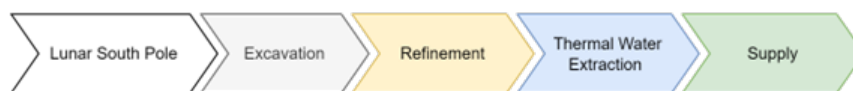
FIGURE 1.1: Simplified ISRU value chain; adapted and adjusted from [Hab, 2022] as part of LUWEX: the Lunar South Pole shows evidence of water and is planned for future Lunar lander missions [LUWEX, 2022, NASA, 2023a].

Chapter 2, which provides an extensive review of the literature covering several fundamental aspects pertinent to the extraction of Lunar resources. It examines the presence and distribution of water-ice deposits on the Moon, contrasts Lunar environmental conditions with those on Earth, discusses the significance of Lunar regolith simulants in experimental and simulation contexts, and surveys prior work in the domain of water extraction methodologies. These foundational insights lay the groundwork for the subsequent methodological and experimental stages of this study. The core of the investigation is segmented into three principal stages, each addressing a critical phase in the extraction process. Each stage leverages simulations, coupled with heat transfer and ice deposition analyses, to yield high-fidelity models of the physical phenomena involved. These stages are obtained as follows:

- STAGE I: **Sublimation** This initial stage builds directly upon the literature review, translating theory into a practical modelling framework. Data collection and preliminary simulations serve as a foundation for developing this model that describes heat transfer within Lunar regolith and subsequent sublimation of water-ice. The sublimation process— a phase transition from ice to vapour—is modelled to determine optimal heating parameters that maximise efficiency without excessive energy consumption.

- STAGE II: **Deposition** Following the sublimation and release of water vapour from the

regolith, this stage addresses the controlled capture of the vapour. Simulations examine the spatial and temporal distribution of vapour to identify conditions conducive to maximising deposition rates. The capture process involves cooling mechanisms that allow for the transition from vapour back to solid ice, where deposition models are refined to predict the most efficient conditions for maximising yield.

- STAGE III: **Liquefaction** In the final stage, the study models the liquefaction process, where captured ice undergoes a controlled phase transition to liquid water. This stage represents the culmination of the extraction process, directly aligning with the objective of supplying liquid water as a consumable resource for Lunar operations. The liquefaction model addresses the thermal inputs required for phase transition, the design of containment systems to prevent vapour loss during melting, and the energy efficiency of the process.

The comprehensive modelling efforts across these three stages are validated through the LUWEX experiment. Situated within a thermal vacuum chamber (TVAC), the experimental setup precisely replicates the harsh conditions of the Lunar surface, including low temperatures and near-vacuum pressures. The TVAC setup is instrumental in experimentally verifying the theoretical and simulation-based models, providing data that confirms or refines each phase of the water extraction process. This validation step enhances the credibility and applicability of the models, serving as a crucial link between simulation and practical deployment.

Upon validation, the insights derived from these stages enable a systematic optimisation of the extraction system. This research directly informs the design of the crucible—the containment unit specifically engineered to extract water from Lunar regolith. A refined understanding of the thermal and phase-change dynamics inherent provides critical input for optimising system parameters, including heating efficiency, material selection, and overall design. The resulting data enables iterative improvements, aligning the extraction system's performance.

In conclusion, this thesis contributes not only to the field of ISRU but also to broader efforts in sustainable space exploration, as it advances our capability to extract, store, and utilise vital resources in Lunar environment.

2 | Lunar Environment and Future Missions

On March 5, 1998, a major discovery pointed to the possible presence of water ice on the Moon, based on data from the Lunar Prospector spacecraft. This finding supported earlier data from the Clementine mission in November 1996, both suggesting that water ice might exist at the Moon's North and South poles [Feldman, 1998]. At first, it seemed that the ice was mixed with Lunar surface material—rocks, soil, and dust—at small amounts, around 0.3% to 1%. However, more detailed analysis from Lunar Prospector indicated that there could be pockets of nearly pure ice hidden beneath as much as 40 centimetres of dry surface material.

FIGURE 2.1: The Lunar South Pole; an image created by National Geographic and NASA, captured by the Lunar Reconnaissance Orbiter Camera (LROC) and ShadowCam [NASA, 2023a].

2.1 The Moon

Researchers and space agencies have conducted numerous studies to understand the surficial conditions, geology, and challenges associated with Lunar exploration. This part of the review synthesizes key findings from various studies on the Moon's surficial conditions, encompassing temperature extremes, lack of atmosphere, radiation exposure, regolith characteristics, and other relevant factors.

Characteristic	Earth's South Pole	Lunar South Pole
Temperature[a]	220 K	110 K
Pressure	10^5 Pa	10^{-11} Pa
Atmospheric Composition[b]	O_2 | N_2 | H_2O	Ar | Ne | He
Atmospheric Density	10^{19} molecules/cm^3	10^5 molecules/cm^3
Day-Night Cycle	24 hours	29.5 days[c]

[a]The averages temperatures are determined for both the Earth and the Moon. Its mean values are based on yearly values for the past 50 years.

[b]Oxygen, Nitrogen and Water are the main components in the air for planet Earth, whereas the Lunar south pole defines a significant lower density with components of amongst Argon, Neon and Helium.

[c]A Lunar day is the roughly 29.5 Earth days long period of time for Earth's Moon to complete on its axis one synodic rotation, meaning with respect to the Sun. The Lunar day is therefore the time of a full Lunar day-night cycle.

TABLE 2.1: Characteristics of the south pole on the Moon and planet Earth.

2.1.1 Solar energy

The Lunar environment differs significantly from Earth, characterized by the absence of an atmosphere on the Moon's surface. This lack allows direct penetration of solar radiation, contributing an average radiant energy flux of around 1.1 MJ/cm^2 per year to the Lunar landscape. Notably, specific polar regions feature PSRs, serving as an abundant and perpetual source of solar energy, as indicated by recent research [Speyerer and Robinson, 2013]. The South Pole boasts 26 km^2 with more than 80% illumination, while the North Pole and its surroundings have approximately 74 km^2 of equal illumination [R. Pappa, 2020].

As anticipated, solar energy emerges as a promising commodity for Lunar exportation. The collection of solar power through strategically positioned solar panels on the Lunar surface opens up possibilities for beaming this energy to various locations within Lunar space [Harris, 2008]. A key aspect of this Lunar solar power initiative involves the conversion of collected solar energy into microwaves. Subsequently, these microwaves are transmitted either directly or indirectly in the form of multiple power beams. This transmission is facilitated through the use of orbital reflectors or re-transmitters, ultimately reaching receivers on Earth with remarkable efficiency [Criswell, 2000].

This approach not only taps into the Lunar environment's unique solar potential but also establishes a viable means of harnessing and delivering Lunar-derived energy to Earth, paving the way for innovative advancements in space-based energy systems.

2.1.2 Surficial Conditions

One of the fundamental aspects of Lunar surficial conditions is the wide range of temperatures experienced on the Lunar surface. Daytime temperatures can reduce to around 127 degrees Celsius, while nighttime temperatures can reach to as low as -173 degrees Celsius. The Lunar environment is characterised by low temperatures and vacuum conditions, particularly in regions where water

ice deposits are present, such as near the Lunar poles. PSRs have formed in these areas due to a combination of the Lunar surface and the moon's obliquity. The South Pole exhibits a greater number of PSRs compared to the North Pole. These regions pose challenges in terms of accessibility, limited solar energy, and the uncertainty surrounding the presence of water. In cold traps within these PSRs, surface temperatures can reach as low as 30 K, with a maximum range below 110 K [Fanale et al., 2021], see table 2.1. Overall, Lunar surface temperatures vary from 100 to 400 K, and the temperature difference between Lunar day and night can be as large as 300 K [Johnson and Carroll, 1972, Hearth, 1989, G. Heiken, 1991]. Understanding these extremes is crucial for designing spacecraft, rovers, and habitats that can withstand such temperature differentials [Smith, 2018]. The Moon's virtually nonexistent atmosphere presents challenges for landing, mobility, and thermal regulation. This section reviews studies exploring the effects of the Lunar vacuum on spacecraft and equipment, as well as the absence of atmospheric scattering and its implications for observations and communications [Johnson, 2020, Farrell, 2011, Hodges et al., 1974].

The Moon, lacking a substantial atmosphere, experiences regular temperatures above 300 K, causing volatile substances to rapidly escape from the surface [Luchsinger et al., 2021]. These vacuum conditions involve the directed pressure of the solar wind, typically less than 10^{-9} Pa, and the pressure of randomly moving gas particles within the solar wind, less than the magnitude of 10^{-11} Pa [Johnson and Carroll, 1972]. Despite the extremely thin atmosphere, measurements have shown that during the day, around $10^4/cm^3$ molecules exist, while the number increases to a magnitude of 10^5 per cubic centimetres during nighttime [G. Heiken, 1991].

This randomly moving gas mainly comprises hydrogen and helium nuclei but also includes nitrogen, carbon, and noble gases. Interestingly, during Lunar night, the abundance of noble gases like argon decreases instead of increasing. This decrease occurs because argon can condense at the low temperatures experienced during Lunar nighttime, while neon, helium, and hydrogen do not condense. Volatile substances deposited in the Lunar regolith can disperse throughout the soil due to impacts, with their levels often influenced by soil maturity and the solar wind. Impacts on the Moon's surface can be caused by cometary material deposition, meteorites, and volcanic activity. The interaction between the Lunar surface and the solar wind leads to the formation of oxygen and hygrogen bounds and water molecules on the surface, while impacts from hydrated meteorites also contribute to water deposition [Sargeant, 2020].

The absence of a substantial atmosphere and magnetic field on the Moon exposes its surface to elevated levels of radiation. This section could explore studies on the distribution of Lunar features, such as craters, mountains, and mare regions, and their implications for exploration missions [Zuber, 2016]. However, since the Lunar South Pole is the prior region to explore further for water evidence, it is not considered furthermore (section 2.1.4).

2.1.3 Surface Composition

The Lunar regolith, a surface layer composed of fragmented rocks and dust, provides essential insights into the Moon's geological evolution. The regolith's composition, geotechnical properties, and operational challenges have been extensively studied [G. Heiken, 1991]. Visualizations of the Lunar surface, reveal a fine, powdery upper layer with particle sizes extending up to several centimetres. Although commonly referred to as Lunar soil, this term is technically inaccurate as the regolith lacks organic content and terrestrial weathering products. Consequently, regolith is a more precise descriptor for this fragmentary material [Noble, 2019].

Lunar regolith consists of rock fragments, mineral grains, volcanic and impact glasses, and unique 'agglutinates', fragments bound by glass and formed through micrometeorite impacts. Agglutinates, which can comprise up to 60-70% of some regolith samples, are a distinctive feature of the Lunar surface, created when micrometeorite impacts melt small portions of the regolith, binding mineral fragments upon cooling [Noble, 2019]. Another significant component of the regolith is spherules, small, typically spherical glass droplets formed through volcanic processes or impact events, where the molten material is ejected, cools mid-air and resettles on the surface. Regolith

particle sizes typically range from 40–800 µm, with a median size between 45–100 µm [McKay D. S. and M., 1991]. By terrestrial standards, regolith samples might resemble silty sands, but these classifications are challenging because of the unique formation processes on the Moon. Around 10% of regolith particles exceed 1 mm, 50% are larger than 100 µm, and 90% are greater than 10 µm. The finest fractions (<2 µm) are difficult to measure as smaller grains adhere to larger ones and to container walls. The bulk density of Lunar regolith starts around 1300 kg/m^3 at the surface, increases quickly to 1520 kg/m^3 at 10 cm depth, then more gradually to approximately 1830 kg/m^3 at 100 cm, and asymptotically approaches 1920 kg/m^3 below 100 cm. Even at depths with higher bulk density (10–15 cm), porosity remains around 40–50%, influenced by particle size distribution and irregular shapes, as smaller particles do not efficiently fit between larger ones. Using Apollo data, porosity ranges from about 65% at the surface to less than 40% at depth.

Geotechnical properties of the Lunar surface were quantified by Apollo missions and compiled in sources like the Lunar Sourcebook [G. Heiken, 1991]. However, Apollo probes reached only a few meters, so properties at greater depths remain less defined, transitioning from direct measurements to estimates and models [Connolly and Carrier, 2022]. Properties such as density, cohesion, shear strength, and porosity, which vary with depth, are crucial for understanding regolith behaviour [Connolly and Carrier, 2023]. One notable feature is the highly irregular, surfaces of regolith particles, providing approximately eight times the surface area of equivalent-sized spheres. This irregularity enhances soil cohesion through particle interactions. Lunar regolith evolves through
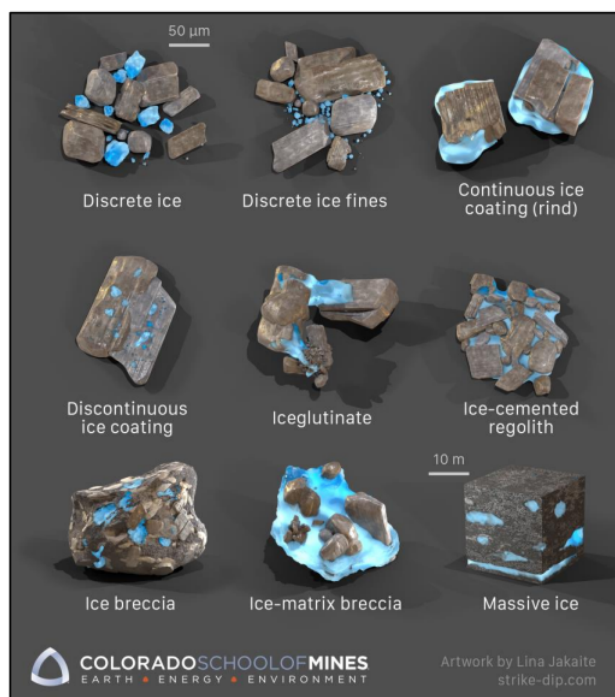
FIGURE 2.2: Possible ice formations within Lunar regolith; scale in 50 μm; an image created by L. Jakaite [Jakaite, n.d.].

exposure to the harsh space environment. This process is balanced by the formation of agglutinates, leading mature regolith to achieve a steady-state particle distribution [McKay D. S., 1974]. Piquette *et al.* demonstrated that water ice within Lunar cold traps could remain stable over extended timescales, highlighting its potential as a future resource [Piquette et al., 2017]. Further evidence for the presence of water ice on the Lunar surface is examined in the subsequent section.

2.1.4 Evidence of water

Launched in January 1998 as part of NASA's Discovery mission, the Lunar Prospector orbited the Moon, equipped with the Neutron Spectrometer designed to detect traces of water ice below 0.01% [Feldman, 1998]. The Neutron Spectrometer was particularly focused on Lunar polar regions, anticipating water ice deposits.

Analysis revealed a distinctive 4.6 percentage by weight (wt.%) ratio over the North polar region and a 3.0 wt.% division over the South. The instrument could detect water to a depth of approximately half a meter. On November 29, 1996, it was announced that data from a Clementine spacecraft experiment suggested the presence of ice on the Moon's surface, possibly at the bottom of PSR near the South Pole. Since frozen volatiles like water ice reflect radio signals in a distinctive way, scientists analysed these reflections to look for signs of ice. This raised the possibility of water ice near the South Pole. However, follow-up observations shown in Fig. 2.3, suggested that surface roughness could also explain the observed reflections, therefore nuanced previous observations.
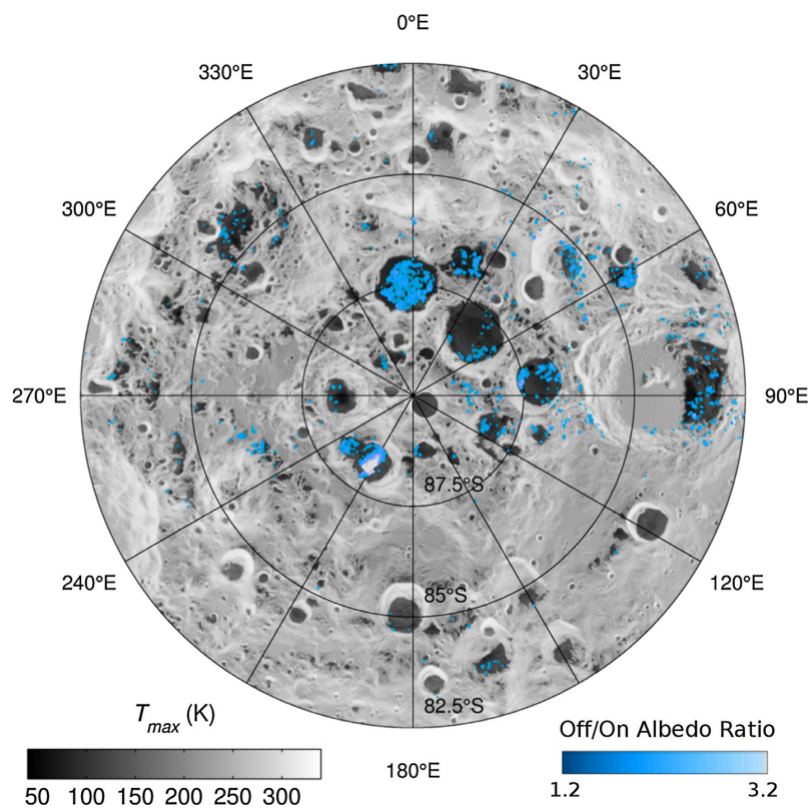
FIGURE 2.3: Locations with unusual UV albedo may indicate the presence of water ice. The colors in the data represent points where the off/on-band albedo ratio is above 1.2, and the Lyman-albedo is below 0.03. Typically, areas outside PSRs show an average ratio of around 0.9. Ratios between 1.2 and 4.0 suggest water ice concentrations from 0.1 to 2.0 wt.%. In areas where patches of pure water ice intermittently mix with dry regolith, the overall abundance could reach as high as 10% [Hayne et al., 2015].

The initially anticipated extensive ice coverage on the Moon, estimated to be between 10000 to 50000 km^2 near the North Pole and 5000-20000 km^2 around the South Pole, has been revised to a more localised perspective [Feldman, 1998, G. Heiken, 1991]. In contrast, Li et $al.$ [Li, 2018] performed the analysis based on data from the reflection spectrum. Specifically, the near-infrared absorption spectrum characteristics of ice were identified, providing direct evidence of ice on the PSRs at the Lunar poles. Surface-exposed ice with up to 30 wt.% water ice content was confirmed

in the polar regions, indicating the potential for water-ice mining within PSRs. Direct evidence of water-ice presence on the Moon was obtained from in-situ measurements by the Chinese Spacecraft Chang'E5 ([Lin et al., 2022]). LCROSS, launched with the LRO, impact results in the Cabeus crater on the Lunar South Pole showed a water ice content of 2.7 varying to 8.5 % by mass [Colaprete, 2010].

Furthermore, [Fanale et al., 2021] suggested that significant amounts of water-ice, up to 10-20% of the permanent cold trap area, could occur in micro cold traps. The regolith in these micro cold traps may contain a similar water ice mass content as the PSRs, approximately 5 % by mass. While Moon samples and remote-sensing data have shown Lunar water depletion compared to Earth, recent exploration reveals potential water reservoirs on the Moon. The predominant water resources exist in the form of mixed water ice in polar Lunar regolith, with neutron spectrometers on the Lunar Prospector providing indirect evidence of ice in polar craters. Spatially distribution of water frost in PSRs has been observed, with an estimated total mass of about $2.9 \cdot 10^{12}$ kg within the uppermost meter of PSRs [Crawford, 2015].

Laboratory measurements of Apollo 15 and 17 samples indicate water contents mostly in the 5 to 30 parts per million (ppm) range, while some pyroclastic deposits may contain as much as 1500 ppm of water [Li S, 2014]. Recent Chang'E-5 sample analysis estimated a water content of at least 170 ppm in Lunar regolith, providing insights into surface water distribution in the middle latitude of the Moon [Zhou, 2022].

2.2 Future Lunar Exploration Missions

Scientifically, the Moon serves as an invaluable time capsule, preserving the ancient history of our solar system. Unravelling its geological mysteries provides crucial insight into planetary formation and the dynamic processes that shaped the early cosmos. Additionally, the Moon's unique environment offers an ideal testing ground for developing and advancing technologies.

2.2.1 Development Requirements

Future Lunar exploration missions are crucial for scientific discovery and technological innovation. The Moon holds clues to the mysteries of our solar system's past, offering unique insights into planetary evolution. Beyond its scientific significance, Lunar exploration advances crucial technologies and paves the way for sustainable space exploration. The quest for Lunar resources, particularly water, not only sustains future human colonies but also fuels our ambition to venture deeper into the cosmos. International collaboration and public engagement amplify the impact, making Lunar exploration a pivotal frontier in our ongoing exploration of the universe.

This section delves into the persistent and forthcoming challenges associated with Lunar exploration, encompassing the development of technologies to navigate environmental constraints and explore opportunities for scientific discovery, as well as the potential for human habitation [Thangavelautham, 2022]. The uncertainties surrounding the development of ISRU technologies and water extraction underscore the importance of clearly defining assumptions to approach specific solutions with more accuracy.

Within the scope of this research, a pivotal assumption revolves around the state of water on the Moon, a facet for which comprehensive data is lacking due to the absence of conclusive information from prior Lunar exploration missions. Sowers and Dreyer [2019] assert that the economic viability of thermally extracting water from the Lunar surface depends on factors such as extracting over 18 kg of ice per square meter within a time frame of less than 44 hours. Therefore, considering a variety of scenarios is imperative to account for the diverse challenges that a future Lunar system may encounter.

2.2.2 NASA - Draper Lunar Lander (CP-12) [NASA, 2023b]

Scheduled for a 2025 touchdown in the Schrödinger basin on the Lunar far side, the Draper Lunar Lander is a NASA mission equipped with three science payloads for geophysical measurements. A vital component of NASA's Commercial Lunar Payload Services initiative, Draper Laboratories collaborates as the commercial partner, providing the launch and lander. The Schrödinger basin, displaying signs of recent volcanic activity, will host seismometers, a drill for deploying heat flow and electrical conductivity probes, and instruments studying the magnetic field and surface weathering. The SERIES 2 lander can transport up to 500 kg of payload to the Lunar surface NASA [2024]. The mission, currently in early planning stages, signifies a significant stride in Lunar exploration and scientific investigation.

2.2.3 NASA - Blue Ghost Mission 1 (TO 19D) [NASA, 2023b]

Blue Ghost Mission 1 is a Lunar lander with a scheduled 2024 mission to deliver ten payloads to the Lunar surface. This program involves a collaboration with Firefly Aerospace, responsible for both the launch and the lander. The mission's primary objectives encompass investigating Lunar interior heat flow, plume-surface interactions, magnetic fields, and capturing X-ray images of Earth's magnetosphere.

The Blue Ghost lander features a payload capacity of 155 kg. Power is derived from solar panels, offering a nominal 450 W and a peak of 650 W, with deployment options for optimal sunlight exposure. Thermal control mechanisms include heat pipes, radiators, multi-layer insulation, and active heaters.

Key technology tests include regolith sampling, satellite systems, radiation-tolerant computing, and dust mitigation. The launch is planned for 2024 aboard a two-stage Firefly Alpha vehicle, targeting a landing site in Mare Crisium on the Moon.

2.2.4 ESA - Heracles [ESA]

The Heracles mission, scheduled for a potential launch in 2028, represents a pivotal step forward in our understanding of human-robotic interaction during Lunar exploration. The mission is designed to achieve the ambitious goal of landing a spacecraft on the Moon, conducting sample collection utilising a rover remotely operated from the Lunar Gateway, and subsequently transporting these Lunar samples back to Earth. This aims to not only expand our scientific knowledge of the Moon but also to advance the capabilities of human-robotic collaboration in the challenging Lunar environment.

2.2.5 China - Chang'e 6,7 and 8

Chang'e 6, 7, and 8 are part of China's Lunar exploration program, which aims to explore the Moon, conduct scientific experiments, and potentially pave the way for future human missions. Here is a general overview of the expected objectives for each mission:

- Chang'e 6: This mission is expected to be a sample return mission. The spacecraft is designed to land on the Moon, collect soil and rock samples, and return them to Earth. The goal is to study the Lunar surface in more detail and enhance our understanding of the Moon's composition [Jones, 2023].

- Chang'e 7: This mission is anticipated to be a comprehensive one, with multiple objectives. It may include an orbiter, a lander, a rover, and potentially even a flyby mission to explore different aspects of the Moon. Specific scientific goals may include studying the Lunar surface, geological features, and potentially scouting for resources [Mann, 2019].

- Chang'e 8: The 2028 mission could carry up to 200 kg of equipment from other countries, more than 10 times the payload carried on next year's Chang'e 6 mission Chang'e 8 is likely

to touch down close to the Lunar South Pole, where China hopes to build a Lunar base in just over a decade's time [Xin, 2023].

3 | Water Extraction Methods

Several techniques for obtaining water on the Moon are available, such as extracting it from frozen water ice deposits found at the Lunar poles or PSRs, extracting it from pyroclastic glasses, or producing it by extracting oxygen and hydrogen from Lunar regolith. This study concentrates specifically on the extraction of water from water-ice deposits.

FIGURE 3.1: Water Extraction on the Moon; an image created by LUWEX team.[LUWEX, 2022]

3.1 In-Situ Water Extraction Methods

Due to constraints in the distribution of Lunar water ice resources, achieving large-scale extraction and utilization of water from icy Lunar regolith is challenging. To address the need for in-situ water extraction in future manned Lunar exploration missions, it is crucial to develop a more universally applicable and reliable method.

Two distinct approaches have been developed for different application scenarios: water extraction from icy regolith and water production by hydrogen reduction. However, current detection results indicate that water-ice resources are primarily concentrated in PSRs at the Lunar poles. The limited distribution area and challenges in energy access make it impractical for a global application of water recovery using this method.

The water extraction method from icy regolith appears more suitable for in-situ water extraction in Lunar bases located in polar regions [Zhang et al., 2023]. On the other hand, the water production method by hydrogen reduction holds broader application potential due to the widespread availability of Lunar regolith. The following section is an excerpt from the *LUWEX-CE-Study Design Document*, which outlines the development of the thermal water extraction method as part of the LUWEX project.
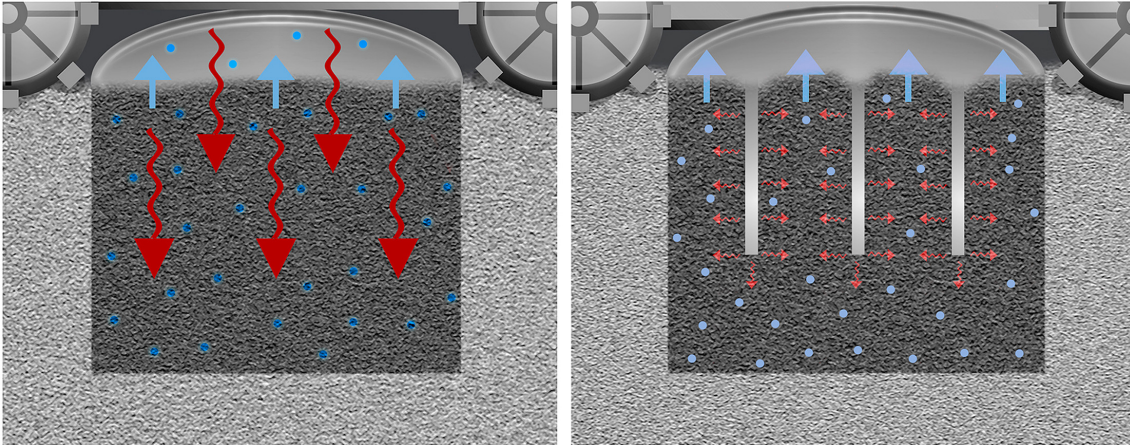
FIGURE 3.2: In-Situ Water Extraction Method; a heated dome placed on the Lunar surface, extracting water from the regolith [Brisset et al., 2020].

3.2 Thermal Water Extraction

Recovering water resources on the Lunar surface is not only a fundamental requirement for human survival but also opens avenues for in-situ conversion and the supply of oxygen and hydrogen using technologies like electrolysis. Additionally, Lunar water resources serve as crucial raw materials for diverse applications, including Moon-based scientific experiments, biological culture and Lunar construction. Consequently, acquiring in-situ Lunar water resources stands out as a pressing technical need for future Lunar exploration and base construction missions.

The majority of water resources are primarily located within icy Lunar regolith in the PSRs at the South and North Poles. In the proposed scheme depicted in fig. 3.2, sunlight on the Lunar surface is harnessed directly for heating, with reflective mirrors aiding in directing sunlight to heat mining drills or tents (see table 3.1). The approach involves sublimating ice in frozen regolith, capturing water vapour within tents, and collecting it using cold traps. Another promising method for extracting water from icy Lunar regolith involves drill-based excavation systems (see table 3.1). This technique employs a hollow auger to drill into the icy Lunar soil, followed by a heating process to

vaporise and collect the ice, thereby facilitating water resources development. Recent work by [He et al., 2021] introduced n auger-based water extraction and collection scheme using Lunar regolith simulants. The technological process includes the auger-drill descending to the surface, forming a temporary sealing space. Subsequently, the auger-drill drills holes to transport icy Lunar regolith upward, heating them with an infrared lamp. The resulting heated water vapour is then directed into a cold condenser for collection.

Study		Initial Ice [%]	Power [W]	Sample [kg]	Recovery[a] [%]	Time [h]	Reference
S I M U L A T I O N	Heating drills (25) by Brisset	1	25000	1440	35	5.5	[Brisset et al., 2020]
	Surface heating by Brisset	5	1000	1440	59	45	[Brisset et al., 2020]
	Hollow auger (Ref) by Wang	20	500	23.84	0.10	2	[Wang et al., 2023]
	Double-walled hollow tube by Wang	20	500	23.84	1.53	2	[Wang et al., 2023]
	Heating rods (5) by Song et al.	30	125	3068.47	8.7	95	[Song et al., 2021]
	Heating rods (7) by Song et al.	30	180	3068.47	24.7	271	[Song et al., 2021]
	Heating rods (9) by Song et al.	30	216	3068.47	30.8	337	[Song et al., 2021]
E X P E R I M E N T	Heated Dome by Sowers and Dreyer	12	250	0.0704	70.2	20	[Sowers and Dreyer, 2019]
	Cryogenic container by Sowers and Dreyer	5.6	250		1.29 [g]	5	[Purrington et al., 2022] [Sowers and Dreyer, 2020]
	Cryogenic container by Sowers and Dreyer	5.6	250		2.7 [g]	20	[Purrington et al., 2022] [Sowers and Dreyer, 2020]
	Cryogenic container by Sowers and Dreyer	12	250	0.0374	63.7	5	[Purrington et al., 2022] [Sowers and Dreyer, 2020]
	Cryogenic container by Sowers and Dreyer	12	250	0.0704	70.2	20	[Purrington et al., 2022] [Sowers and Dreyer, 2020]
	Yang et al.						[Yang et al., 2023]
	Microwave heating by Cole	5.6	250	0.0411	67	0.4167	[Cole et al., 2023]
	Microwave heating by Cole	14.7	250	0.0408	48	0.4167	[Cole et al., 2023]
	He et al.	10	400	4.95	22.5[g]	1	[He et al., 2021]
	He et al.	10	400	4.95	52.5[g]	2	[He et al., 2021]

[a]The recovery is calculated based on the ratio between captured water [g] and initial ice mass [g]. The initial ice mass is considered as feed whereas the captured water is the final outcome.

TABLE 3.1: Various water extraction methods have been investigated through simulations, experiments, or a combination of both approaches, courtesy of Luca Kiewiet.

Table 3.1 summarizes various studies on water extraction techniques, comparing parameters such as the initial ice percentage, power applied, sample mass, recovery percentage of water, and extraction duration. Among these studies, efficiency—measured by the water recovery percentage—is a critical factor for assessing each design's effectiveness. The heating rods method by Song et al. [2021] achieved high recovery values, particularly with nine rods, reaching up to 30.8% over an extended duration of 337 hours. In contrast, Wang et al. [2023] shows a relatively low recovery (0.10%) using a hollow auger but operated with significantly lower power and sample size, indicating it might be suited for low energy-constrained scenarios rather than high-efficiency requirements. For short-duration extraction, study by Sowers and Dreyer [2020] achieved up to 70.2% recovery within 20 hours at 250 W of power. This design stands out for its high recovery rate making it effective for water extraction. Another notable technique is using microwave heating. Cole et al. [2023] achieved a 67% recovery in only 0.42 hours with a small sample size. This combination of

high recovery and rapid sublimation suggests that microwave heating is highly efficient. In conclusion, for the highest efficiency and recovery rate within a reasonable time frame, a cryogenic container design is the best choice. It provides a balance of high water recovery and operational efficiency. For achieving rapid sublimation, microwave heating would be the alternative.

3.3 LUWEX

LUWEX, a project funded by the European Union's Horizon Europe framework program and led by the German Aerospace Centre (DLR), aims to advance technologies for Lunar Water Extraction (LUWEX). The primary objective of LUWEX is to develop and refine techniques for extracting purified water from Lunar regolith, specifically targeting icy-regolith deposits found in PSrs of the Moon. As this thesis is part of this large-scale project, it contributes directly to the LUWEX mission by exploring and optimizing processes such as sublimation, deposition, and liquefaction of Lunar water-ice.

This research aligns closely with LUWEX's goal of achieving effective ISRU technologies on the Moon, addressing key technical challenges posed by the Lunar environment. The insights gained from this study are intended to feed into the LUWEX framework, informing the development of robust water extraction systems that can withstand extreme conditions and operate efficiently in low-gravity, low-pressure environments. Through experimental validation, simulations, and detailed process modelling, this thesis provides foundational knowledge that advances LUWEX's mission to establish a sustainable source of water for future Lunar exploration missions.

3.4 Transport Phenomena and Lunar Regolith Simulant

In mathematical modelling, porous media, structural analysis, and phase transition phenomena require distinct approaches due to the complexity and unique properties of each system. Regolith is characterized by the ability to hold and transport water vapour through interconnected void spaces. Understanding fluid and heat transport within regolith is essential for applications in water extraction. With mathematical models, one can predict how regolith will transport water vapour and how it behaves under phase transitions. When successfully implemented, these model help to optimize design, efficiency and eventually cost-effectiveness.

Besides modelling, the Lunar environment needs to be simulated in order to perform accurate experiments. Replicating the Lunar vacuum, has been achieved through the use of vacuum chambers. These so-called thermal vacuum chambers (TVAC) create low-pressure environments, allowing to investigate the effects of vacuum on materials, equipment, and regolith samples. Furthermore, creating Lunar regolith simulants has been a focus of research to replicate the unique composition of the Moon's surface. These simulants, designed to mirror the granularity and composition of Lunar soil, facilitate experiments and testing of equipment intended for Lunar exploration.

3.4.1 Thermal Conductivity in Icy-Regolith

In the preceding sections, particularly in section 2.1.4, various forms of ice structures were discussed, stating the development of a robust heat transfer model. To represent the thermal properties of the ice-regolith mixture, one can employ a volumetric mixing model, which provides a framework for estimating key relationships between density, thermal conductivity, and heat capacity, as suggested in the works by [Hab, 2022, Heitkamp, 2023]. The mixture's properties are derived by combining individual thermal models for regolith and ice. Specifically, the thermal properties for dry regolith are obtained from [Martinez and Siegler, 2021, Woods-Robinson and Paige, 2019], while the thermal conductivity of ice is taken from [Bonales and Sanz, 2017], and the heat capacity of ice at very low temperatures is sourced from [Shulman, 2004]. Initial parameter values are carefully selected and optimised for the Lunar environment. Numerous studies have significantly contributed to our understanding of the thermal modelling of Lunar regolith and ice, addressing specific parameters and conditions vital for simulating water extraction on the Moon. Key references are summarized as follows:

- [Kiewiet et al., 2022] provides a comprehensive model for icy-regolith, establishing foundational parameters essential for simulating Lunar icy surfaces.

- [Huetter et al., 2008] investigates the effective thermal conductivity of dry regolith, a crucial parameter that impacts heat transfer efficiency in Lunar soil.

- [Bonales and Sanz, 2017] studies the thermal conductivity of ice, an important factor influencing the thermal response of ice under Lunar environmental conditions.

- [Shulman, 2004, Flubacher and Morrison, 1960] provide essential data on the heat capacity of ice for accurate modelling of thermal energy storage in icy-regolith.

- [Hudson and Schorghofer, 2009, Mellon and Postawko, 1997] propose mixing models that are crucial for simulating the thermal properties of heterogeneous materials, such as regolith mixed with ice.

- [Schieber, 2022] presents an integrated model for both dry regolith and ice, facilitating simulations that encompass varying material states.

- [Hörz F. and Binder, 1991] offers geological insights into Lunar composition, which enhances the contextual accuracy of regolith thermal property models.

- [Fountain and West, 1970] addresses the thermal conductivity of dry regolith, impacting the thermal insulation properties of Lunar soil.

- [Siegler, 2012, Martinez and Siegler, 2021] develop comprehensive models for dry and icy regolith, respectively, incorporating temperature-dependent properties.

- [Hao et al., 2023] examines sublimation temperatures in icy-regolith, crucial for determining phase change points from ice to vapour.

- [Nafsun, 2016] explores heat transfer in conjunction with discrete element modelling (DEM), applicable for simulating granular materials such as regolith.

These sources collectively establish a robust basis for developing accurate models of thermal properties and phase transitions in Lunar icy-regolith, enhancing simulations of water extraction mechanisms on the Moon.

3.4.2 Porous Structure of Icy-Regolith

Darcy's Law is a fundamental principle in fluid dynamics, particularly in the field of geology, that describes the flow of fluids through porous media. Darcy's Law provides a mathematical relationship between the factors influencing fluid flow in porous materials. The basic form of Darcy's Law is expressed as:

$$Q = -\frac{\kappa}{\mu_f} \cdot A \cdot \frac{\Delta P}{L}, \tag{3.1}$$

Where Q is the volumetric flow rate of the fluid, κ is the permeability of the material, μ is the dynamic viscosity of the fluid, the cross-sectional area through which the fluid flows is defined as A, ΔP is the pressure difference across the material and length over which the pressure difference is applied is L. In simple terms, Darcy's Law states that the volumetric flow rate of a fluid through a porous medium is directly proportional its permeability, the cross-sectional area through which the fluid flows, and the pressure gradient or hydraulic head gradient. Important for any porous medium is the use of porosity. Porosity represents the fraction of the total volume of a material that exists of void spaces. In a porous medium, such as regolith, porosity is an essential characteristic because it dictates the amount of fluid the material can hold:

$$\epsilon = \frac{V_{\text{void}}}{V_{\text{total}}}$$

Here the volume of the void space or pores is defined by V_{void} whereas V_{total} denotes the total volume of the material. Permeability is a measure of how easily a fluid can flow through a porous material. It depends on the size, shape, and connectivity of the pores. Materials with larger, well-connected pores have higher permeability, allowing fluids to flow through them more easily.

In contrast, materials with small, poorly connected pores have low permeability and restrict fluid flow. Furthermore, Darcy's Law assumes that the flow is viscous, see the use of μ_f. Hence the flow is determined by the Navier-Stokes equations. *Note*: the use of Darcy's law needs to be carefully considered in the flow regime of Knudsen, since it applicability might not be accurate. However, the fluid can be defined as a compressible and incompressible gas, using the ideal gas law. For information, Darcy's Law is widely used in geology to understand and model the movement of water through rocks, and other porous materials. Below studies significantly contribute to our understanding of the porous modelling of regolith-ice mixture and the use of Darcy's Law.

- [Fukusako, 1990] examines the density of ice, providing insights into the mass and phase-change behavior of water-ice in Lunar conditions.

- [Purrington et al., 2022] investigates water vapour transfer rates, focusing on factors such as permeability and porosity that affect water extraction efficiency.

- [Kossacki, 2021] examines the porosity of granular ice and the impact of vertical temperature gradients on surface recession due to sublimation.

In combination with thermal conductivity models these studies collectively establish a basis for accurate modelling of icy-regolith as a porous medium.

3.4.3 Free Molecular Flow

Before elaborating any model, it is important to determine the flow regime. At extreme vacuum conditions, the Navier-stokes equation are not valid any more. The mean free path I determined by the equation Vacuum [2024]:

$$\overline{I} \cdot p = \frac{k_B T}{\sqrt{2}\pi d_g^2},$$

(3.2)

represents the average distance a particle can travel between two consecutive collisions with other particles. In this equation, where pressure p is measured in Pascals, $\overline{I}$ and molecular diameter d_g are in meters. Notably, the mean free path exhibits a linear relationship with temperature and an inverse relationship with pressure and molecular diameter. This molecular diameter is considered relatively constant within the specified temperature and pressure ranges. The explanation for the mean free path lies in the multitude of collisions that a gas particle undergoes along its trajectory. As mentioned before, a laminar flow, for example water flowing steadily from your kitchen faucet, forming smooth, parallel layers without turbulence, is no more valid. To simplify, Knudsen describes the fluid dynamics of gas where the mean free path of the molecules is larger than the size of the chamber. Knudsen flow occurs when the mean free path I of gas molecules is comparable to or larger than the characteristic dimension of the pores L, resulting in a high Knudsen number Kn:

$$Kn = \frac{I}{L}$$

(3.3)

in which k_B is the Boltzmann constant, T is the temperature, d_g is the molecular diameter of the gas. When modelling Knudsen flow, low pressures (typical of Knudsen flow regimes), the mean free path I becomes very large relative to the pore dimensions. Small changes in pressure or temperature can cause large variations in I, which directly affects the Knudsen number. This makes setting consistent initial and boundary conditions complex, as minor variations in environmental parameters lead to substantial changes in flow behaviour. Depending on the value of Kn, different flow regimes can be identified:

- Continuum Flow (Kn < 0.01): In this regime, the mean free path is much smaller than the characteristic length. The fluid behaves as a continuous medium, and the Navier-Stokes equations can be applied. Viscous and pressure-driven flows are typical in this regime.

- Slip Flow ($0.01 \leq$ Kn < 0.1): Here, the mean free path is not negligible compared to the characteristic length. The continuum assumption still holds, but slip boundary conditions are necessary to account for molecular effects at the boundaries.

- Transition Flow ($0.1 \leq \mathrm{Kn} < 10$): The mean free path and the characteristic length are of comparable magnitude. Neither continuum flow models nor free molecular flow models are fully applicable. The flow requires the Boltzmann equation.

- Free Molecular Flow ($\mathrm{Kn} \geq 10$): For large Knudsen numbers, the mean free path is much larger than the characteristic length. Collisions between gas molecules are rare, and the flow is dominated by molecule-wall interactions.

In free molecular flow gas molecules interact more frequently with the boundaries than with each other. As a result, boundary conditions must account for rarefied gas dynamics. Inconsistent boundary conditions lead to significant inaccuracies in flow predictions, confirmed by COMSOL Multiphysics®.

The mean free path I is highly sensitive to temperature T and inversely proportional to pressure p. Given by $I = \frac{k_B T}{\sqrt{2}\pi d_g^2}$, even small changes in temperature or pressure dramatically alter I and, consequently, Kn. Maintaining stable temperature and pressure distributions is particularly difficult in 3D simulations, further complicating the modelling process. The computational load increases significantly due to the large number of particles or grid points needed to resolve free molecular flow accurately. Simulating any Knudsen flow regime described above in irregular geometries requires extremely high-resolution grids or a high number of simulated particles, both of which drive up the computational expense. Knudsen flow requires careful initialisation of pressure, temperature, and molecule distributions across the domain. Any inconsistency in these initial values propagates through the simulation, leading to instability or divergence.

3.4.4   Volumetric Mixing Model by Wasilewski [2021a]

Consider a phase transition from phase one to phase two, defined by the function $\alpha_{1 \to 2}$ shown in fig. 5.3. When ice begins to sublimate, i.e., $\theta_2 > 0$, the effective porosity of the sample increases due to the outgassing of water vapour, making porosity time-dependent. This temporal change in porosity, in turn, affects the thermal conductivity of the sample, influencing the sublimation process. Let the thermal conductivity of the regolith, ice, and water vapour mixture be described by an arbitrary function h, such that:

$$k = h(t). \tag{3.4}$$

To ensure sublimation in any thermal model outlined in any of the aforementioned source, the following condition must be satisfied:

$$\theta_2 > 0 \quad \forall h. \tag{3.5}$$

If this condition holds, an optimal thermal model is established. Now, let h be a function of the effective porosity of regolith ϵ, the pore filling fraction F, and the thermal conductivities of regolith, ice, and vapour, respectively:

$$k \sim H(\epsilon, F, k_r, k_i, k_g), \tag{3.6}$$

where k_r and k_i denote the thermal conductivities of regolith and ice, respectively, and k_g represents the radiative thermal conductivity of the vapour (water vapour). Note that h is a time-dependent function that relies on H and the aforementioned parameters. The radiative thermal conductivity component of water vapour in the gaseous state can be described as:

$$k_g = \frac{pL \cdot k_{wv}}{(pL + \overline{I})}, \quad k_g \geq 0, \tag{3.7}$$

where p and T denote system pressure and temperature, and k_{wv} is the thermal conductivity of gaseous water vapour. The total thermal conductivity can thus be expressed as:

$$k = \epsilon F k_i + k_r + k_g \to k \equiv H(p, T, \theta_1, \theta_2). \tag{3.8}$$

Here $\epsilon F k_i$ represents the thermal conductivity contribution from the ice phase, accounting for the filling fraction F and effective porosity ϵ. Understanding these interactions is essential for accurately modelling heat transfer in porous materials like icy-regolith, particularly during phase transitions. The mean pore size L in the porous medium, dependent on the phase transition from θ_1 to θ_2, can be characterized as:

$$L = L(\theta_1, \theta_2) = d_p \left(\frac{0.905}{[1 - \epsilon(1 - F \cdot \theta_1)]^{1/3}} - 1 \right), \quad L \geq 0, \tag{3.9}$$

where ψ represents porosity, indicating the volume fraction of pore space. The filling fraction F is defined as:

$$F = F(\theta_1, \theta_2) = \frac{\rho_{rb}/(1 - C_i) - \rho_{rb}}{\epsilon \rho_i}, \tag{3.10}$$

where ρ_{rb} is the bulk density of dry regolith, C_i is the initial water content in the porous mixture, and ρ_i is the particle density of ice. The filling fraction F is crucial as it indicates the fraction of pore volume filled by the vapour or liquid phase, directly affecting heat and mass transfer. Porosity ϵ, dependent on effective and particle density of the regolith, is defined by:

$$\epsilon = \epsilon(\theta_1, \theta_2) = \left(1 - \frac{\rho_{\text{eff}}}{\rho_r} \right). \tag{3.11}$$

In a heating process, the effective density varies over time, governed by phase transitions. Permeability κ, which quantifies fluid flow through the porous medium, is given by:

$$\kappa = 2 \cdot 10^{-14} \exp(12.469 \cdot \epsilon(1 - F\theta_1)), \tag{3.12}$$

highlighting how variations in filling fraction F impact pore structure and fluid transport pathways, especially during phase changes.

3.4.5 Lunar Regolith Simulant

Lunar regolith simulant is an artificial substance crafted to emulate the physical and chemical traits of the Lunar soil present on the Moon's surface. As interest in space exploration and potential Lunar missions grows, the development and utilisation of Lunar regolith simulants have become crucial for equipment testing, experimentation, and advancing our comprehension of Lunar surface conditions. This literature study refrains from delving into the fundamental aspects of Lunar regolith simulants, as extensive research has already explored their composition, production methods, applications, and relevance in space exploration. However, the primary focus here is to redesign a Lunar water extraction system capable of withstanding various simulants.

To validate the water extraction system, an experimental setup replicating Moon conditions is essential. Therefore, accurate simulation of regolith properties is crucial, encompassing particle distribution, chemical decomposition, porosity, and density to align with reality. LUWEX has access to simulants from The Exolith Lab, a specialised company producing materials that closely mimic Lunar regolith's texture and physical properties [Exolith, 2023]. These simulants are tailored to represent diverse Moon locations, including the darker mare regions and highlands. It's essential to note that these simulants portray dry regolith and do not account for water content.

3.4.6 Preparation of Icy-Regolith by LUWEX

LUNEX and LHS-1 are Lunar regolith simulants specifically developed to replicate the properties of Lunar soil for experimental research. **LUNEX** is designed to simulate the mineral composition and particle size of Lunar highland soil, making it especially useful for water extraction studies McKechnie et al. [2020]. **LHS-1**, created by the Exolith Lab at the University of Central Florida, is another highland simulant that closely matches the density, composition and abrasive characteristics of Lunar soil Cannon et al. [2019].

In addition to highland simulants such as LHS-1, the Exolith Lab also produces simulants representing the Lunar mare regions. Mare simulants replicate the basalt-rich composition of the Moon's volcanic plains, such as Mare Imbrium, which is characterized by a higher density and increased levels of iron compared to the highland areas. Mare Imbrium, one of the largest Lunar mare regions, was formed by ancient volcanic activity and has a darker composition Spudis [1996]. These variations between highland and mare simulants allows to test technologies and processes specific to each type of Lunar region, including applications near the Lunar South Pole, where ice deposits are accessible Cannon et al. [2019].

The LUWEX project benefits from access to both highland and mare simulants, enabling experimentation across diverse Lunar conditions or even combining characteristics of both regions. To prepare an icy-regolith simulant with consistent ice content and to avoid contamination from external moisture, the regolith simulant must first be thoroughly dried. The sample is heated at 383 K for a minimum of twelve hours. Once dried, it is transferred directly to a dry and vacuum environment to prevent rapid water adsorption from humid air. For experiments requiring cryogenic conditions, the dried simulant is cooled in a metal container surrounded by evaporating liquid nitrogen, which creates a dry, slightly pressurized environment that minimises moisture exposure. To ensure safe handling and prevent frost formation, tools like spoons and sieves are pre-cooled before contact with the simulant, allowing to conduct experiments safely at extremely low temperatures.

3.4.7 Thermal Vacuum Chamber

A thermal vacuum chamber (TVAC) is a specialised piece of equipment used for testing and simulating space-like environments to assess the performance and reliability of various components, instruments, or spacecraft. The primary purpose of a TVAC is to simulate the extreme conditions of outer space, including extreme temperatures and vacuum conditions to ensure the functionality and durability of components or systems intended for space missions. The chamber should be capable of achieving and maintaining a wide range of temperatures, from extremely high to extremely low, to replicate the thermal fluctuations experienced in space. The materials used in the construction of the chamber must be carefully selected to withstand extreme temperature differentials and maintain their integrity in a vacuum environment. Harvesting water from lunar regolith involves several stages, each with distinct methods. Though a variety of techniques exist, this section focuses primarily on thermal extraction, regarded as one of the most promising approaches. To clarify why thermal extraction is prioritized, the following sections will provide relevant background information.

4 | Lunar Water Extraction Design

Extracting water from Lunar regolith involves a complex processes, including heating, phase changes, and flow behaviour. Figure 4.1 presents a three-dimensional CAD model of a comprehensive design for water extraction. However, as you delve into the subsequent sections, you will discover that this model may not encompass all necessary aspects for effective extraction.
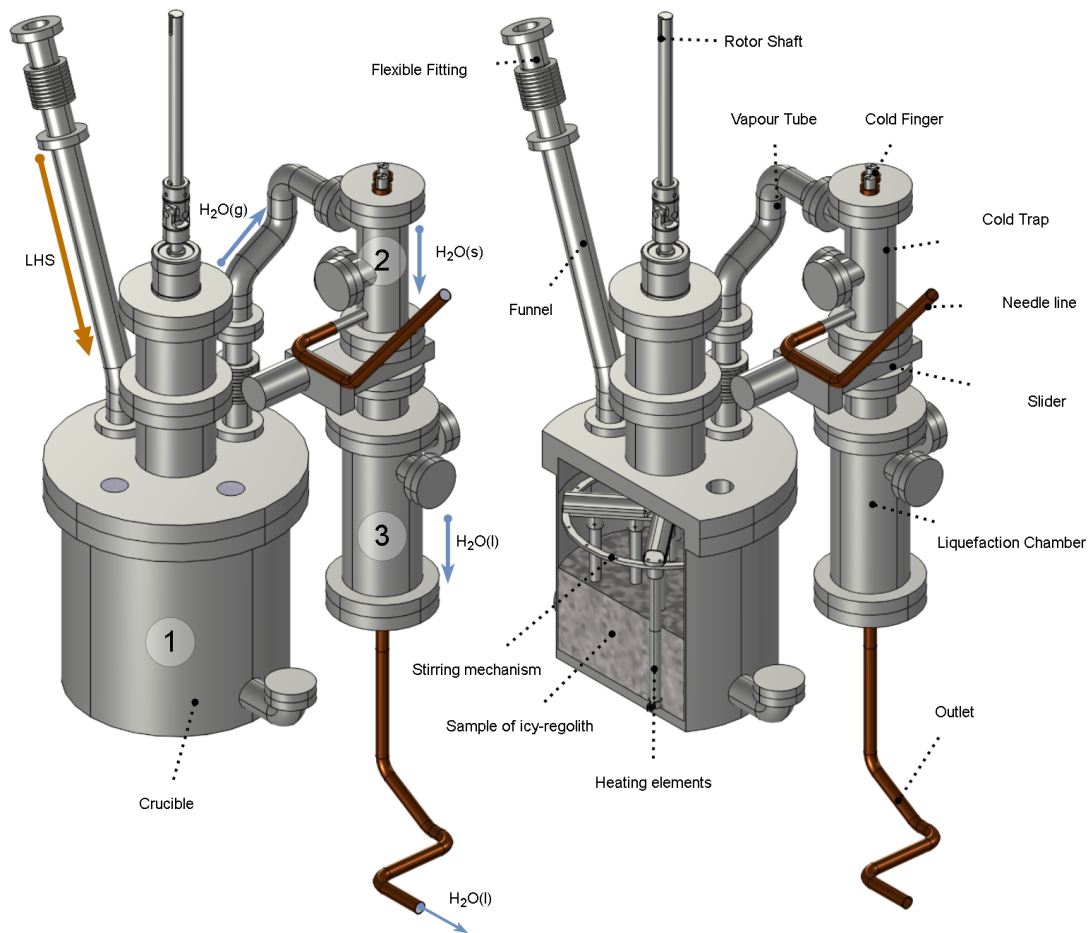
FIGURE 4.1: Three-dimensional CAD model of the Lunar water extraction system, adapted for CFD modelling. *Note*: this model is designed specifically for fluid dynamics simulations and differs from the original system's physical design.

4.1   Methodology

Harvesting water from lunar regolith involves several stages, each with distinct methods. Though a variety of techniques exist, this section focuses primarily on thermal extraction, regarded as one of the most promising approaches. To clarify why thermal extraction is prioritized, the following sections will provide relevant background information.

Aside from thermal methods, other innovative techniques have shown potential for water extraction from lunar regolith, including **chemical reduction with hydrogen** and **electrostatic beneficiation**. Electrostatic beneficiation employs electrostatic fields to isolate water-bearing particles—or specifically, oxygen—from dry regolith particles. This process attracts them to charged surfaces. However, since this technique directly isolates oxygen rather than producing water, it is generally less efficient for water extraction. Larger systems with higher power requirements would be necessary, which limits water recovery goals on the Moon Ikeya et al. [2024].

In contrast, chemical reduction with hydrogen involves treating Lunar regolith with hydrogen gas at high temperatures. This method reduces iron-oxides in the regolith, releasing a mixture of water, oxygen, hydrogen and metallic iron. Despite, hydrogen reduction primarily targets oxygen extraction and is effective mainly for iron-rich minerals like ilmenite. Since ilmenite presence near the Lunar South Pole is expected to be low, this method is limited in efficiency for water extraction. Studies, such as those by Guerrero-Gonzalez and Zabel [2023], indicate that low ilmenite concentrations would necessitate larger, heavier systems, further limiting its inefficiency as a water extraction method in polar regions.

Given these constraints, thermal water extraction remains the most promising method. This approach directly targets water-ice within the regolith, extracting it in a form that contains both hydrogen and oxygen—crucial elements. Evidence in section suggests that ice deposits are concentrated near the Lunar South Pole, making this technique suitable. The following section will delve into the specific methods of thermal extraction and the heating approaches required for its implementation.

4.1.1   Thermal Water Extraction

Two primary approaches to water extraction from Lunar regolith are in-situ and excavative methods. **In − situ** water extraction involves directly heating the surface of Lunar regolith, which requires a specific type of enclosure due to exposure to the Lunar environment. Since in-situ extraction is open to ambient conditions, creating a barrier between the heated surface and the surrounding environment is essential. This can be achieved with a dome or tent, designed to minimize heat loss to the surroundings and maximize heat penetration into the Lunar surface. With such an enclosure, the heating method can be enhanced through tools like drills or heated boring equipment to improve efficiency.

In contrast, water extraction by **excavation** involves first excavating the Lunar regolith and subsequent placing it inside a closed container. Here, heat is applied to sublimate water-ice. **Sublimation** is the phase transition directly from a solid to vapour. Heating methods for excitative extraction vary and can include heated drills, static heating elements, or combinations of both. Research by Hab [2022] show that the production of water and hence the water recovery is much greater for using excavation with respect to in-situ heating. Therefore, in-situ water extraction is not considered further. Moreover, for the LUWEX project and this study specifically, the experimental setup requires a batch process. *Note*: Batch production applies to the excavation and sampling phase only. The connection between subsystems and continuous liquid water production will be discussed later.

In excitative extraction, once a regolith sample is in a closed container or **crucible**, external heating raises its temperature to a sublimation point. As sublimation occurs, water ice transitions directly into water vapour, which is then collected to ultimately produce liquid water.

4.1.2 Heating Method

Solar heating, though advantageous because it does not require a direct power supply, has limited practicality for water extraction in PSRs near the Lunar poles. To be effective, solar heat would need to be redirected, often using mirrors or other reflective surfaces. However, maintaining these mirrors and keeping them dust-free in the harsh Lunar environment presents a significant challenge. As such, solar heating remains a less effective option for extracting water in low sunlight areas, though it may be feasible for thermal processing applications outside shadowed regions.

Microwave heating, by contrast, offers potential benefits in its speed and energy efficiency, as demonstrated in studies by Cole et al. [2023]. His research on low-power microwave heating suggests that, with low power available on the Lunar surface, this method could facilitate water extraction using either multiple low-power heating units or a single, higher-power unit. However, the exact mechanisms that cause the Lunar regolith to interact with microwave radiation are still in discussion, with factors such as ilmenite content and particle shape thought to play roles Taylor et al. [2010]. Microwave heating poses challenges in regulation, making it ideal primarily for processes in additive manufacturing, where regolith particles undergo fusion Liu et al. [2024], Lim et al. [2022]. Though microwave heating has proven efficient on small samples, it necessitates a Faraday cage to prevent leakage, adding to the system's complexity.

With these considerations, electrical heating is chosen as the preferred method for Lunar water extraction. Previous research embedded in the LUWEX project has shown that low-power electrical heating is effective for extracting water vapour and simplifies the experimental setup for Earth-based testing Heitkamp [2023]. The subsequent section will outline the process for capturing water vapour produced through this heating method.

4.1.3 Capturing Water Vapour

After sublimation of water-ice, its gaseous state needs to be captured at some point. Capturing water vapour can be achieved by either capturing in a solid or liquid state (directly). In order to capture water vapour and directly transition it into liquid water, one needs pressure. At the triple point of water, which defines a temperature of 273.15 K and a pressure of 611.73 Pa, there is a unique set of conditions, where water can exist simultaneously in its solid, liquid, and gas phases. In other words, this is the lowest pressure at which water can be in its liquid form. Therefore, in order to capture water in its liquid state, one needs a minimum pressure of 611.73 Pa.

Capturing by condensation (g → l)

This process of phase transition from solid (s) to liquid (l) is called **condensation**. In this regards, a condenser is a device used to convert water vapour into liquid by cooling it down. In the context of water extraction from Lunar regolith, a condenser would be used to capture and condense the water vapour produced during sublimation or heating processes, allowing it to transition back into liquid water for collection and use. A condenser requires a cooling system to lower the temperature of the water vapour. On the Moon, this could involve passive radiative cooling using the Lunar environment's natural cold temperatures or an active cooling system for precise control. To efficiently condense water, the condenser must be mounted in a sealed compartment where water vapour can be directed until it condenses. This helps prevent loss of vapour to the Lunar vacuum and ensures that the vapour remains in close proximity to the cooling surface for efficient condensation. Once condensed, liquid water needs to be collected and transported for storage. Since lunar gravity is lower than Earth's, a low-pressure pump may be required to move the condensed water to a storage tank.

Capturing by deposition (g → s)

The process of directly transitioning water vapour (g) to solid ice (s) on a cold surface is known as **deposition**. In this context, a cold trap is a device used to capture water vapour by cooling it to

the point of deposition, forming solid ice. In Lunar water extraction, a cold trap would capture and freeze water vapour produced during sublimation or heating processes, allowing it to be retained as ice for later collection. A cold trap requires a cooling system to lower the surface temperature sufficiently for water vapour to freeze upon contact. Once deposition occurs, the solid ice must be collected and transferred for further processing. Given the Moon's low gravity, facilitating the removal of ice from the cold trap surface may require the use of a mechanical scraper, external vibration, or a low-power heater in a process called **delamination**. Delamination refers to uncoupling the ice from the cold trap substrate, allowing for its release and transport to liquefaction stage. Prior studies have investigated various delamination methods—such as vibration, magnetic excitation, or mechanical scraping—but found these approaches largely ineffective (Kalis [2024]). They often introduce drawbacks, including system fatigue from vibrations, the complexity and mass of added moving parts, actuators, and increased system size.

In contrast, LUWEX primary experiments have demonstrated that thermal delamination effectively separates ice from a copper substrate, achieving efficient ice release without these additional complexities. Thus, combining ice deposition with thermal delamination provides a viable solution for capturing and storing water in solid form. This approach facilitates a sustainable water extraction process without adding more complexity such as pumps, scrapers and condensers.

4.1.4 Liquefying & Purification

When capturing water through deposition, the ice must be melted to obtain liquid water. This leads to a complete extraction process with multiple phase transitions: gas → solid → liquid. Ice liquefaction can occur in two distinct cycles, each suited to different production methods.

In a **single − batch** production cycle, each deposited batch of ice is immediately transferred to a liquefaction chamber and melted in a single process. In a **multi − batch** cycle, multiple batches of deposited ice are stored in the liquefaction chamber and liquefied together in a single operation. When the liquefaction chamber is fully loaded with ice, heat is applied to initiate melting. The chamber's inner core, made of copper, ensures efficient heat transfer for consistent phase transition.

The chamber is isolated from other extraction subsystems when the slider or gate valve is closed, preventing any direct mass or heat transfer to other parts of the system. However, the chamber still experiences some ambient heat loss. Once filled with ice, the chamber can be pressurized by introducing nitrogen gas or by allowing pressure to build naturally as a portion of the ice sublimates upon initial heating. As the copper core heats the ice, sublimated vapour increases the chamber pressure until the required level for melting is achieved. This phase transition from solid (s) to liquid (l) is known as **melting**.

At this stage, the water is considered a pure substance, although the LCROSS mission revealed that it contains various volatile compounds, including ammonia, carbon dioxide, hydrogen sulphide, and methanol, which must be removed to make the water consumable Colaprete [2010]. This process, known as **purification**, occurs after liquefying the ice in the chamber. While the design of the capture subsystem accounts for some purification criteria, the purification subsystem itself lies beyond this study's scope and is intended to operate after liquefaction.

4.2 General Design Criteria

The design, crafted to comply with LUWEX standards, is illustrated in Figure 4.1, where each component is identified and labelled. Familiarizing yourself with these component names is crucial, as they will be consistently referenced throughout the following sections to ensure clarity in discussing subsystems and operations.

4.2.1 Water Extraction Subsystem

For a robust evaluation of the performance of the water extraction subsystem, including the dynamics of mass transfer, a large amount of ice is required to accurately simulate conditions. This enables precise monitoring of the effects of water vapour on the system, leading to the establishment of specific operational requirements:

- Sample Requirements: The Lunar regolith simulant (LHS), should contain 15 kg of material with an initial ice content below the limit of 20 wt. %. The sample is placed within a specialized crucible and is subjected to controlled heating via heating elements within the *stirring mechanism*, inducing sublimation of the water content.

- Inlet and Preconditioning: The LHS-ice mixture enters the crucible via a precisely designed *funnel*, acting as the sample inlet. To maintain integrity, the sample temperature must be preconditioned to 140 K or lower before entering the system.

During the sublimation phase, temperature regulation is critical to prevent overheating, with tight pressure control required to facilitate sublimation in high-vacuum conditions.

4.2.2 Water Capture Subsystem

The water capture subsystem facilitates the conversion of water vapour to ice through deposition, followed by its liquefaction. This process depends upon a stable flow rate to support continuous operation, a topic discussed further in subsequent sections.

- Configuration: The *cold trap*, featuring two *cold fingers*, provides the environment where water vapour is converted into ice. The ice accumulation occurs at the phase change interface, which must be maintained below 200 K to avert the formation of volatile compounds like methanol.

- Needle Line: A precisely dimensioned *needle line* permits controlled venting of excess water vapour from the cold trap prior to liquefaction. This element plays an important role in managing the flow rate and maintaining pressure stability.

- Minimizing Delamination Losses: Heat application to remove excess ice should be minimized to conserve energy and maintain high water recovery. The delaminated ice represents a loss factor that must be controlled in relation to the required energy for phase change.

4.2.3 Water Liquefaction Subsystem

When ice is deposited onto a cold surface, it detaches through a process known as delamination and is directed towards the liquefaction chamber.

- *Slider Mechanism*: This subsystem features an ultra-high-vacuum (UHV) sliding gate valve, referred to as the Slider, which isolates the liquefaction chamber from external environments. This mechanism prevents unintended mass transfer, such as backflow into the crucible.

- *Copper Inlay*: The inner chamber, lined with copper, is designed to facilitate efficient heat transfer, reducing the time required to convert ice into liquid water. Heat must applied at the boundaries of the copper inlay to support the phase transition process.

4.2.4   Experimental Setup and Environmental Control

The setup within the TVAC is designed with precise environmental parameters to simulate conditions similar to those on the Lunar surface. Central to this is the cold shroud, which must maintain an ambient temperature of 140 K or lower. The chamber operates at a high vacuum, with pressure kept at or below 1e-4 Pa, essential for the intended experiments. The integration of various subsystems is improved through the use of flexible fittings that accommodate minor tolerance variations, facilitating connections among the components. The compact design of the cold shroud also contributes to added complexity. The **cold shroud** is not shown in fig. 4.1 but consider the following; the entire three-dimensional model including each part is centred in the cold shroud. Recall that the system must be subjected to lunar-simulated conditions. The experimental setup features a network of pipes, tubes, and valves, primarily made of stainless steel, with the exception of the copper tubes connected to the cold trap and the liquefaction system. These copper components allow easier bending and heating. Each tube and valve are configured according to its functionality and the connections required for effective operation. For instance, the water vapour flow from the crucible to the cold trap is managed by a needle valve, while any vapour loss during operation can be monitored using a mass spectrometer. Electric pneumatic valves control the connections outside the TVAC. As the chamber is evacuated and cooled with a liquid nitrogen cooling system, the subsystems for capturing and extraction will remain under ambient pressure. Subsequently, liquid nitrogen will be introduced through a funnel in the quick-access door to effectively cool the crucible and the cold trap.

4.2.5   Structural Analysis

To evaluate the structural integrity of the stirring mechanism, a simplified model of the original design (Figure 4.3) was developed. Non-essential components such as the crucible housing, rotor shaft, slip ring, motor, outlets, and various assembly parts were excluded for clarity. Notably, the stirring rods contain cartridge heaters that span approximately two-thirds of each rod's length, aligning with the level of the icy-regolith mixture. Since the crucible is partially filled with icy-regolith, the stirring mechanism can be divided into two segments: one in contact with the icy-regolith and one without. Figures 4.2 and Appendix C provide further details of structural analysis. Under typical conditions, a DC motor exerts 12 Nm of torque on the shaft. The analysis reveals no material failure under normal operating conditions. To determine failure thresholds, the applied torque, M_0, is incrementally increased. For simplicity, key conclusions are summarized as follows:

- A steady state (fig. 4.2) is sustained at $M_0 = 12\,\text{Nm}$,

- Material failure in the key occurs when $M_0 > 50$.

These results suggest that material failure is unlikely under normal operating conditions. Only at torque levels where $M_0 > 50$ Nm does the likelihood of failure in the key increase significantly. However, this extreme scenario is improbable, as the motor would likely stall before reaching such levels. In addition, the non-fixed nature of the rods allows movement, which further reduces stress build-up.

4.3   Weights/Dimensions

The LUWEX experiment utilizes a solid sample weighing 15 kg, composed of a mixture of ice and regolith simulant. With an initial ice content of 4.75%, this results in approximately 750 grams of ice present within the regolith. The overall design is constrained by the dimensions of the TVAC, which limits the experimental setup. As mentioned in the introduction to this chapter, the current model may not cover all the necessary aspects for effective extraction processes. While the entire experimental apparatus occupies a room-sized space, several meters in scale, the actual system within the cooling chamber, referred to as the *cold shroud*, has an approximate volume of just 1 cubic meter. All components illustrated in fig. 4.1 are carefully arranged within this space, ensuring that the testing environment closely simulates Lunar conditions.
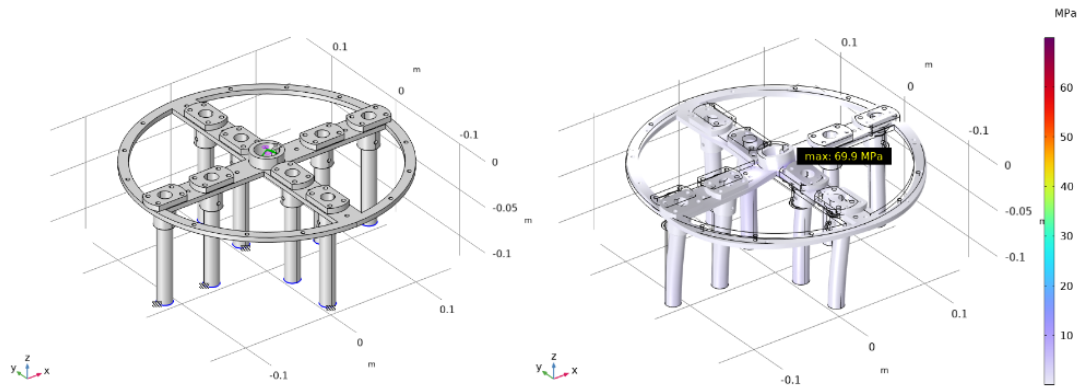
FIGURE 4.2: The bottom area of all rods are assumed to be fixed in all directions due to high resistance of regolith; rotations by the motor on the shaft lead to momentum M_0 acting on the center (axis of rotation), (x,y,z) = (0,0,0) mm; this momentum leads to reaction force F0 from the key (NL: spie). *Note*: if M_0 is positive (counter-clockwise) F_0 should be negative in the y-direction because it is a reaction force from the key on the shaft. F_0 acts from the point (x,y,z) = (8.76,0,0) mm.; Von Mises stress for torque value $M_0 = 12$ Nm around the z-axis, with deformed scale factor of 2000 for clarity.

4.4 Electrical Power

This section highlights the practical implementation of heating cables as a key solution for managing energy requirements in Lunar applications. The power supplied by heating cables is determined through the relation:

$$P = \frac{U^2}{R} \tag{4.1}$$

where P represents the power in W, U is the voltage in V, and R is the resistance in ohms. This equation allows for the estimation of power input necessary for specific models discussed in this study, with particular attention to sustainability and efficient power management crucial for Lunar operations.

In practical terms, the cartridge heater shown in fig. 4.3 is embedded within cylindrical stirring rods, with voids filled using magnesium oxide for insulation. To model the heating effect, the power produced by each cartridge heater is transformed into a heat flux, calculated by dividing the power output by the heater's surface area. For an arrangement involving eight cartridge heaters generating 800 W in total, the resulting heat flux can be distributed along the rods' boundaries but limited to the area below the icy-regolith filling level, ensuring efficient use of energy.

Given the Moon's environment, minimizing power input is crucial. Reduced power consumption aligns with sustainability efforts, reducing reliance on limited sources like solar energy. Lightweight and durable materials, such as magnesium oxide for insulation, are also desirable as they support heat management, prevent overheating, and align with the goal of efficient, lightweight designs that enhance operational performance.

4.5 Equipment

The design shown in fig. 4.1 outlines all components within the cooling chamber (cold shroud) inside the TVAC, representing the equipment setup. This section details the materials used for

these components and investigates the functionality of the stirring mechanism under operational conditions, including an analysis of the regolith packing resistance acting on the mechanism's framework.

4.5.1 Stirring Mechanism

The stirring mechanism comprises multiple components, including the rotor shaft, slip ring, stirring rods, framework, and heating elements or cartridge heaters, among others. For the models presented in this study, the primary focus is on the rotation and heating functions of the stirring mechanism, specifically the part situated within the crucible (see fig. 4.3). Additionally, the crucible is only partially filled with regolith to allow for effective outgassing, represented by a designated filling level. Once sublimation occurs, the resulting water vapour flows toward the exit via the vapour tube before entering the capturing subsystem or cold trap.

4.5.2 Material List

AISI 304L is a widely used stainless steel known for its corrosion resistance and robust mechanical properties, making it suitable for various applications, including aerospace. A more advanced variant, AISI 316, offers superior corrosion resistance, particularly against chlorides, and is frequently employed in chemical processing due to its enhanced durability.

To improve conductivity, several components are made from copper, a conductor ideal for electrical wiring and heat exchangers, ensuring efficient heat transfer in diverse applications. Magnesium oxide fills voids in cylindrical tubes and heating elements, used for its insulating properties and thermal stability. In the initial functional tests of the LUWEX experiments, a sample consisting solely of glass beads was utilized. These tests provided preliminary results to verify that each component functions as intended.

Additionally, SWPL96 is utilized as a high-performance insulation material, showing low thermal conductivity of 0.07 W/m/K. Its lightweight structure and thermal insulation properties make it suitable for high-temperature applications. While it is true that a vacuum is the best insulator, the insulation materials also contribute to compacting the overall design, ensuring that each subsystem is well-connected and aligned with the heating cables. Collectively, these materials create a robust solution for challenging conditions, such as those found in the Lunar environment.

Variable	Material							Unit
	AISI 304L	AISI 316	Copper	Aluminium	Magnesium Oxide	Glass	SWPL96	
ρ	7894	8000	8960	2700	3580	2500	96	kg/m^3
k	16	15	400	238	60	0.84	0.07	W/m/K
C_p	500	500	385	900	1030	750	850	J/kg/K
α	12.3	16	17	23	12	9	5.2	$10^-6/K$
E	193	200	110	70	330	69	1.0	GPa
ν	0.28	0.30	0.35	0.33	0.37	0.21	0.10	1
ε	0.9	0.92	0.1	0.04	0.23	0.95	0.85	1

TABLE 4.1: Material properties at room temperature, i.e. T = 293.15 K.
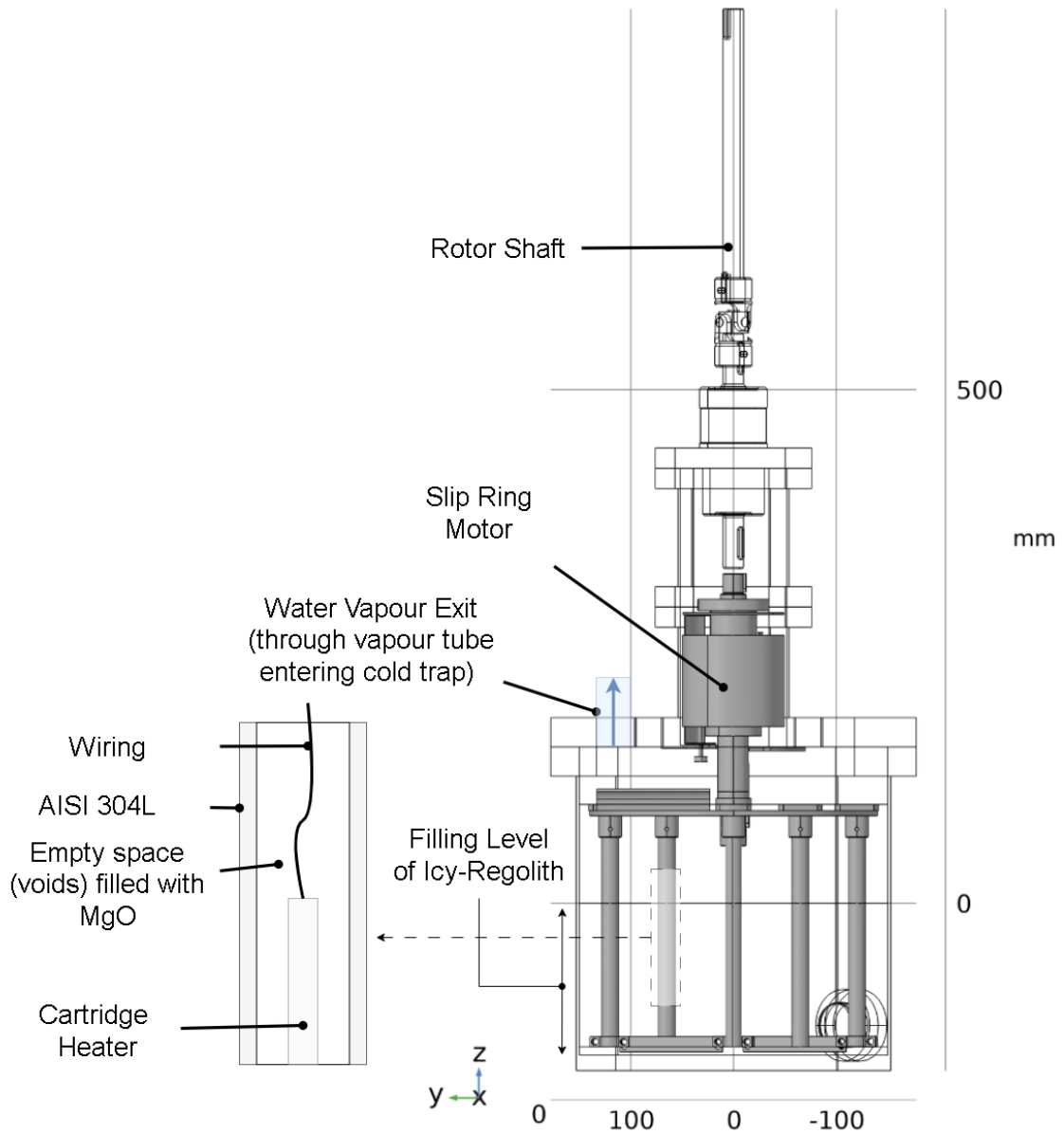
FIGURE 4.3: Clear image of the stirring mechanism consisting of one cartridge heater inside each cylindrical rod (tube) where voids are filled with magnesium oxide (MgO).

5 | Stage I: Sublimation

Sublimation is the process in which a substance transitions directly from a solid state to a gaseous state without passing through the liquid phase. In the context of water, sublimation refers to the transformation of ice directly into water vapour. A sample of ice and Lunar regolith is placed inside a container (future referenced as crucible), see fig. 5.1 below, where its particles will move and extract heat until ice undergoes **sublimation**.
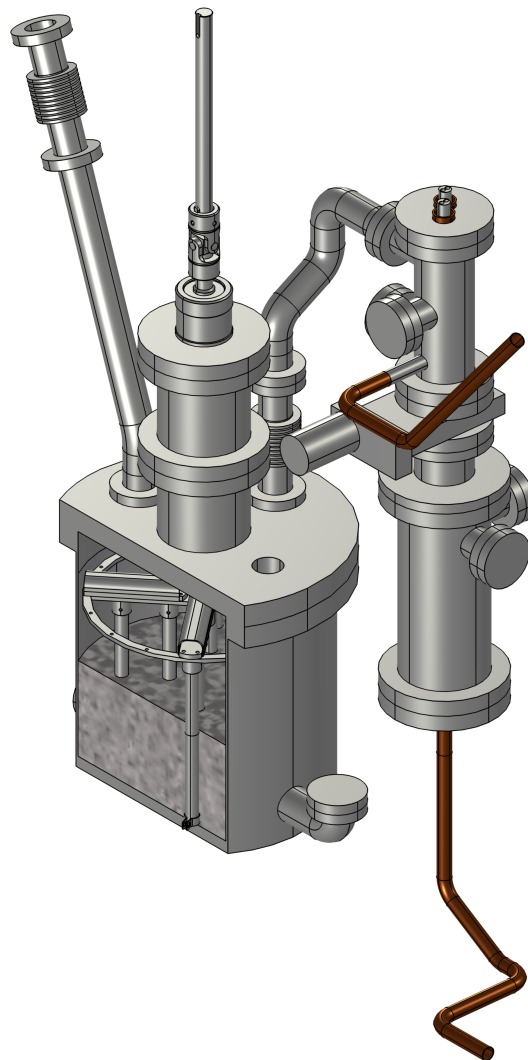
FIGURE 5.1: Illustration of the setup where a sample consisting of ice and Lunar regolith is placed inside a crucible. To provide context for the system's size, the sample has a height (z_{LVL}) of approximately 150 mm.

5.1 Methodology

To extract water from Lunar regolith, the crucible is equipped with specialised heating elements that ensure sufficient thermal energy is applied to sublimate the ice embedded within the regolith. Sublimation, the direct phase change from solid ice to water vapour, occurs as the regolith surface is gradually heated. At initialisation, the thermal energy supplied overcomes the ice's enthalpy of sublimation, releasing water vapour from the regolith. The vapour then escapes from the sample's surface and is directed towards the vapour tube. For efficient and rapid sublimation, a rotating stirring mechanism is integrated within the crucible to maintain a uniform temperature distribution across the sample. This mechanism is particularly essential given the low thermal conductivity of regolith, which can lead to uneven heating if left undisturbed. By ensuring movement of regolith and ice particles, the stirring mechanism prevents temperature gradients and ensures that sublimation occurs uniformly across the entire sample volume.

The *stirring mechanism* rotates on its z-axis ensuring proper movement of ice and regolith particles

Water vapour leaves the *crucible* through *the vapour tube*

Sublimated water excapes from the Lunar regolith surface

Stage I: sublimation of water within Lunar regolith*

Regolith particle

Stirring/heating rods apply heat to the sample

Water vapour can flow through the pores of the regolith

FIGURE 5.2: Illustration of the working principle for extracting ice from Lunar regolith. The system includes stirring/heating rods with surface area A_{rod} interacting with the icy-regolith up to the filling level z_{LVL}. Each cartridge heater has an area $A_{cartridge}$, supplying thermal energy to promote the phase transition from ice to vapour. This diagram highlights the heat distribution zone without considering additional phenomena such as diffusion or absorption.

Throughout this process, the thermal properties of both the regolith and the ice are assumed to remain constant. Although, in reality, these properties may exhibit some temperature dependence, this simplification allows for a more stable optimisation framework. The working principle of the crucible, as illustrated in fig. 5.2, involves several stages. The sample is heated by the heating elements or cartridge heaters, focusing energy on the ice within the regolith pores. To clarify, the stirring mechanism consists of several rods or cylindrical tube, see fig. 4.3. These rods not only move the regolith in crucible but also directly heat the sample. Each cartridge heater can apply a power of 100 W. In summary, the stirring mechanism serves two functions: heating and stirring. This ensures temperature uniformity, allowing ice to sublimate from all regions of the regolith at a consistent rate. As water vapour is formed, it moves along a controlled path towards the vapour tube, minimising back-diffusion and maximising vapour flow towards the exit. In this setup, the design assumes that phenomena such as diffusion, absorption, and re-adsorption of water vapour into the regolith are negligible unless mentioned otherwise. Thus, the focus remains solely on the sublimation process and the transport of vapour from the regolith to the collection zone. This simplification is critical for isolating the sublimation effects and ensuring a high rate of water recovery.

Variable	Discription	Default value	Unit
rpm	Rotations per minute	3	1/min
P	Effective power input in sample	$\zeta \cdot N \cdot$ 100 W	W
N	Number of cartridge heaters	8	1
ζ	Ratio of surfacea areas, $A_{cartridge}/A_{rod}$	0.493	1
z_{LVL}	Filling level of icy-regolith	147.74	mm
ϵ	Porosity for dessicated regolith	0.5679	1
F	Pore filling fraction for dessicated regolith	0.1341	1
κ	Permeability for dessicated regolith	$2.3787 \cdot 10^{-11}$	m^2
d_p	Particle diameter of regolith	43.6	μm
T_0	Initial / Ambient temperature	140	K
C_i	Initial water content	4.75	%
T_{pc}	Phase change temperature	273.15	K
ΔT	Transition interval for temperature	100	K
d_g	Water vapour particle diameter	0.275	nm
m	Mass of icy-regolith sample	15.01	kg
p_0	Pressure inside vacuum chamber	1e-4	Pa
μ	Viscosity of water vapour	1.7e-5	$Pa \cdot s$
H_s	Latent heat of sublimation for water	2834	kJ/kg

TABLE 5.1: System parameters and variables required for stage I; sublimation.

5.1.1 Flow Regime

The Knudsen number serves as a dimensionless parameter that indicates the relative importance of molecular mean free path to a characteristic length scale of the system, helping to characterise the flow regime of the vapour:

$$\mathbf{Kn} = \frac{\overline{l}}{L} \tag{5.1}$$

The representative length scale considered, L, may correspond to various physical traits of a system, but most commonly relates to a gap length over which mass transport occurs through a gas phase. In this case, this gap can be evaluated as the pores inside the porous structure of regolith. The mean free path represents the average distance a particle can travel between two consecutive collisions with other particles. The formula governing this mean free path is expressed as:

$$\overline{l} \cdot p = \frac{k_B T}{\sqrt{2}\pi d_g^2} \tag{5.2}$$

In this equation, where pressure p is measured in Pascals, $\bar{I}$ and molecular diameter d_g are in meters. Notably, significant temperature variations are primarily observed within the crucible, where sublimation occurs, leading to potential discrepancies in the Knudsen number values. As sublimation takes place, there is a rapid influx of water vapour molecules, contributing to an increase in pressure within the crucible. It is critical to maintain the operating pressure below 611.73 Pa to prevent reaching the triple point of water and thus mitigating the formation of liquid water, which could adversely affect the extraction process. Under ultra-high vacuum conditions, the flow of water vapour may transition from free molecular flow towards a continuum, particularly within a Knudsen number (Kn) range defined as:

$$1 < \mathbf{Kn} < 1200.$$

This transition is illustrated using the Heaviside step function in fig. 5.3. The Heaviside step function, commonly denoted as $\alpha_{1\rightarrow2}(T)$, is a mathematical function that is defined as follows:

$$\alpha_{1\rightarrow2}(T) = \begin{cases} 0 & \text{if } T < T_{pc} - \frac{\Delta T}{2} \\ 1 & \text{if } T < T_{pc} + \frac{\Delta T}{2} \geq 0 \end{cases}$$

In fluid dynamics and thermodynamics, the Heaviside step function is used to model sudden changes in physical conditions, such as temperature in phase transition. It captures the transition between different phases in a system. In the context of the flow transition from free molecular flow towards transition flow or even a continuum flow, the Heaviside step function can represent the threshold at which the Knudsen number shifts significantly. This means that as the Knudsen number crosses certain values, the behaviour of the flow changes dramatically, indicating a change in regime. The changes in Knudsen number and corresponding regime can be seen in aforementioned section 3.4.3.

Appendix A includes the general heat equation, the continuity equation, and additional relevant equations, illustrating their applications for both fluids and solids. These fundamental equations can be simplified to specific scenarios. For instance, when dealing with solids where bulk motion (v = 0) and compressibility are negligible, the general heat equation simplifies to

$$\rho C_p \frac{\partial T}{\partial t} = k\nabla^2 T \tag{5.3}$$

In summary, while the original forms of these equations are broadly applicable, they are often simplified for solid-state applications by omitting velocity-related terms.

5.1.2 Density and Porosity

The structure of Lunar regolith as a porous medium is complex regarding its composition, grain size, porosity and pores. Understanding these characteristics is crucial for assessing the regolith's capacity to transport water vapour. The particles in Lunar regolith range from fine dust (micron-sized) to larger fragments (up to several mm). This variation in grain size affects the overall porosity and flow characteristics of the medium. The pores in the regolith can vary significantly in size and shape. Pores can be classified as:

- Macro-pores: large voids that facilitate bulk flow.
- Micro-pores: Very small voids that can influence gas adsorption and storage.

The arrangement and connectivity of pores are critical for determining the flow pathways for water vapour. Well-connected pores allow for better fluid movement, while poorly connected pores can trap fluids, reducing effective permeability. However, the geometric arrangement of pores can be irregular due to the random packing of grains, affecting how fluids move through the medium. This irregularity can result in preferential flow paths and varying saturation levels. To give an insight on this irregularity, consider the image in 8 where Lunar regolith and its pores is schematically drawn. Considering the phase transition of water within regolith, it is crucial to understand how density and porosity are influenced by the states of water present in the medium.
The presence of water ice and water vapour introduces significant variability in the structural

characteristics of the regolith. The transition between the solid state and the gaseous state creates a dynamic relationship between density and porosity within the porous medium. This relationship can be mathematically expressed as:

$$\epsilon = \epsilon(\theta_1, \theta_2) = \left(1 - \frac{\rho}{\rho_r}\right), \tag{5.4}$$

where ϵ represents the porosity of the regolith or mixture of ice and regolith. The apparent density of the medium, which is influenced by the relative amounts of water ice and vapour is denoted by ρ. ρ_r is the particle density of the regolith. The apparent density ρ can be expressed as a function of the densities of water ice ρ_1 and water vapour ρ_2 in their respective phases:

$$\rho = \rho(\theta_1, \theta_2) = \rho_1\theta_1 + \rho_2\theta_2, \tag{5.5}$$

where ρ_1 represents the density of icy regolith, corresponding to phase one, and ρ_2 denotes the density of desiccated regolith, which defines phase two, as will be explained in further detail in the next section.

5.1.3 Dessicated Regolith

Regarding the specific transition, θ_1 and θ_2 serve as phase indicators (or consider it a percentage) for the ratio water-ice and water vapour, respectively, under the condition that $\theta_1 + \theta_2 = 1$. However, when incorporating regolith into simulation models, it is necessary to expand phase one to define icy regolith, which includes water-ice. In phase two, the ice transitions into water vapour and is considered dried out Thus, phase two represents the desiccated form of the regolith, based on the assumption that all water vapor can completely outgas the regolith. The phase transition results in changes in porosity. As water ice sublimates into vapour, the reduction in solid volume increases the pore spaces, thereby enhancing the overall porosity of the regolith. In contrast, when the vapour transforms back into ice, the pore volume decreases. The phase change impacts the density of the regolith. When water vapour accumulates, it introduces a lower density component into the regolith. This change can significantly affect the physical properties, such as weight of the regolith structure. The phase transition also has thermal implications, as the energy required for sublimation affects the thermal conductivity of the medium. Variations in density and porosity can result in changes to thermal and physical properties, making it essential to incorporate phase change indicators into these characteristics.

5.1.4 Permeability and Diffusion

Knudsen diffusion describes the transport of water molecules within a porous medium when the pore size is comparable to or smaller than the mean free path of the gas molecules. This mechanism becomes especially relevant under Lunar conditions, where gas molecules predominantly collide with the walls of pores rather than with each other. Within porous media, Knudsen diffusion is affected by both permeability and porosity, as these properties govern the ease of molecular movement and the frequency of their interactions with pore walls. Permeability, which measures the ease of fluid flow through a porous medium, is strongly impacted by Knudsen diffusion when the pores are sufficiently small. In low-permeability materials, where molecular-wall collisions dominate over intermolecular collisions, the flow regime shifts to Knudsen flow. As permeability decreases, Knudsen diffusion becomes a more prominent transport mechanism compared to bulk diffusion. High porosity, by increasing the void space for molecular movement, can enhance diffusion rates, including Knudsen diffusion. However, in porous materials with very small pores, even high porosity can lead to Knudsen diffusion if pore sizes remain within the molecular mean free path. The Knudsen diffusion coefficient, D_K, for a porous medium is given by:

$$D_K = \frac{2}{3} \cdot L \cdot \sqrt{\frac{8RT}{\pi M}} \tag{5.6}$$

where L represents the mean pore diameter, R is the universal gas constant, T is the absolute temperature, and M is the molar mass of water vapour.

This expression assumes gas molecules primarily interact with pore walls, making Knudsen diffusion the dominant process. Knudsen diffusion is particularly relevant in applications where pore sizes are minimal, specially when the gas molecular mean free path is comparable to the pore size. When modelling regolith as a porous medium where its flow field is calculated using Darcy's law, the permeability definition from Kiewiet et al. [2022] becomes relevant. The permeability is defined as:

$$\kappa = 2 \cdot 10^{-14} \cdot \exp(12.469\epsilon(1 - F\theta_1)) \tag{5.7}$$

This equation can be used to determine the permeability as function of phase change. For example, dessicated regolith indicates $\theta_1 = 0$. Therefore, using equations 7.6 and 5.4 one obtains the original bulk density of regolith, $\rho_{rb} = 1400 \text{ kg/m}^3$, and $\epsilon = 0.5679$. *Note:* these values represent default settings as input variables. As a result, eq. 5.7 denotes $\kappa = 2.37872 \cdot 10^{-11} \text{ m}^2$ when all ice is sublimated into water vapour ($\theta_1 = 0, \theta_2 = 1, \epsilon = 0.5679$), representing the permeability of dessicated regolith also shown in fig. 5.12. The mean pore size for dessicated regolith can be defined as:

$$L = d_p \left(\frac{0.905}{\left[1 - \epsilon(1 - F \cdot \theta_1)\right]^{1/3}} - 1 \right), \tag{5.8}$$

yielding $L = 8.59 \, \mu\text{m}$ for $\theta_1 = 0$. Here, regolith particles are assumed spherical, with a constant mean pore size across the sample. Returning to eq. 5.6 and calculating the Knudsen diffusion for dessicated regolith, one obtains for a pore size of 8.59 µm at a temperature of 273.15 K a calculated Knudsen diffusion coefficient for water vapour of approximately $3.24 \cdot 10^{-3} \text{ m}^2/\text{s}$. This suggests that at this pore size and temperature, water vapour diffusion is primarily governed by Knudsen diffusion rather than bulk diffusion. In Knudsen diffusion, molecules are more likely to collide with the pore walls than with each other, resulting in a distinct transport mechanism compared to bulk diffusion.

5.1.5 Phase Change

The Heaviside step function, as shown in Figure 5.3, defines the smooth transition between phase one (ice) and phase two (water vapour). This transition is characterised by a continuous variation within a transition interval, ΔT, around the temperature of the phase change, $T_{pc} = 273.15$ K. The transition is mathematically expressed as a function of the temperature difference from the phase change temperature.

The mass fraction, $\alpha_{1\rightarrow2}$, representing the transition from phase one to phase two, is defined as:

$$\alpha_{1\rightarrow2} = \frac{\rho_2\theta_2 - \rho_1\theta_1}{\rho}, \tag{5.9}$$

where ρ_1 and ρ_2 are the densities of phase one (ice) and phase two (water vapour), respectively. The phase fraction θ_1 and θ_2 define phase one and phase two, respectively, with $\theta_1 + \theta_2 = 1$. ρ denotes the apparent density of the system. The latent heat is accounted for by incorporating it into the apparent heat capacity, C_p, which is given by:

$$C_p = \frac{1}{\rho}\left(\rho_1\theta_1 C_{p,1} + \rho_2\theta_2 C_{p,2}\right) + H_s\frac{d\alpha_{1\rightarrow2}}{dT}, \tag{5.10}$$

where $C_{p,1}$ and $C_{p,2}$ are the specific heat capacities of phase one and phase two, respectively. The latent heat of the phase transition is defined as H_s, which is in this case the enthalpy of sublimation. $\frac{d\alpha_{1\rightarrow2}}{dT}$ is the rate of change of the mass fraction with respect to temperature. Additionally, the apparent thermal conductivity, k, during the phase transition is given by:

$$k = k_1\theta_1 + k_2\theta_2, \tag{5.11}$$

where k_1 and k_2 are the thermal conductivities of phase one and phase two, respectively. This setup allows for an accurate simulation of the phase-change process.
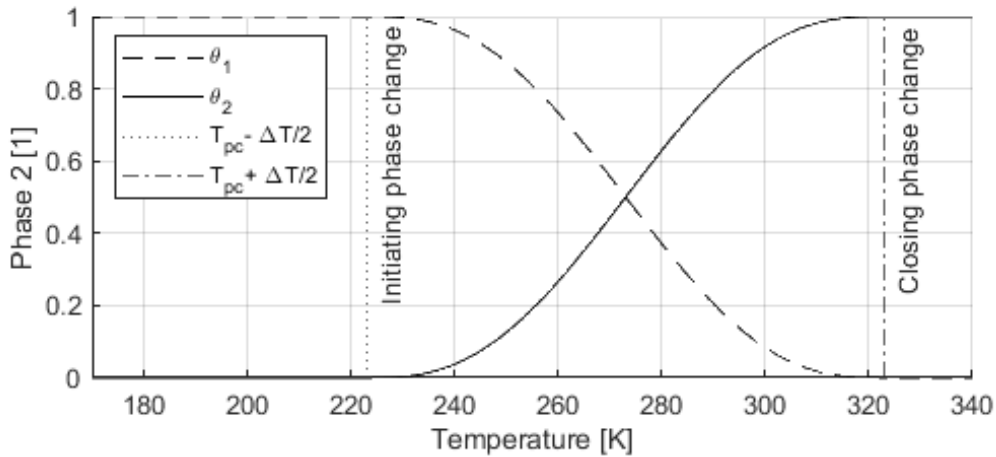
FIGURE 5.3: Smooth Heaviside step function defining the phase transition from phase one to phase two or $\theta_2 = \alpha_{1\rightarrow 2}$ satisfying $\theta_1 + \theta_2 = 1$; it describes a continuous transition within the transition interval $\Delta T = 100$ K around the phase transition temperature $T_{pc} = 273.15$ K.

5.1.6 Temperature Control

While a higher extraction rate might appear advantageous, there are critical considerations for thermal management, particularly at high power levels like 400 W. Such power levels can cause temperatures near the heating elements and the outer surface of the stirring mechanism to exceed 900 K, increasing the risk of sintering the regolith Farries et al. [2021]. Sintering can lead to the bonding of regolith particles, impacting material flow and overall extraction efficiency. Moreover, high temperatures can alter the composition of volatiles through endothermic reactions, potentially changing their properties. Thus, temperature limits must be carefully set to avoid alterations to the mineral composition. Therefore, it is essential to evaluate extraction rates not just by their absolute value but also by their impact on potential sintering and mineral integrity. Additionally, strict temperature control for cartridge heaters and other heating elements will help prevent overheating and ensure the stability of the volatile compounds, which will be discussed in more detail in subsequent sections.

5.2 Sublimation

In this section, the thermal properties of icy-regolith are analysed, particularly focusing on thermal conductivity and specific heat capacity, using the *Volumetric Mixing Model* as detailed in section 3.4.4.

5.2.1 Thermal Conductivity

The thermal conductivity of icy-regolith is determined by the baseline conductivity of the regolith, denoted as k_r, the thermal conductivity of the ice particles, defined as k_i, and a gas conductivity term, k_g, which becomes relevant when ice sublimates into water vapour. The conductivity term associated with outgassing is governed by gas diffusion, expressed as:

$$k_g = \frac{pL \cdot k_{wv}}{(pL + \overline{I})}, \tag{5.12}$$

where p and T represent the system pressure and temperature, respectively, and k_{wv} is the thermal conductivity of gaseous water vapour. It is essential that this gas conductivity term remains positive, thereby requiring $k_g \geq 0$. *Note:* this equation is equivalent to the previously mentioned

equations 3.7 and 3.8. The mean free path $\bar{I}$ is calculated using the appropriate flow regime with the molecular diameter of water vapour, as indicated in eq. 5.2. The total thermal conductivity of icy-regolith can then be expressed as:

$$k_1 = k = \epsilon F k_i + k_r + k_g \tag{5.13}$$

where the filling fraction is calculated according to:

$$F = \frac{\rho_{rb}/(1 - C_i) - \rho_{rb}}{\epsilon \rho_i}, \tag{5.14}$$

with the bulk density of dessicated regolith defined as $\rho_{rb} = 1400\,\text{kg/m}^3$ and the particle density of ice as $\rho_i = 916.7\,\text{kg/m}^3$. The porosity of icy-regolith varies over time as described in eq. 5.4. The initial water-ice content in the sample is defined by C_i. As sublimation occurs, the mean pore size changes due to the outgassing of water vapour. The dependency of this mean pore size on θ_1 is shown in eq. 5.8, indicating that icy-regolith is the first phase during sublimation. The equations 5.10 and 7.9 from section 5.1.5 can now be extended to relate icy-regolith to θ_1 and desiccated regolith to θ_2. Desiccated regolith is defined here in a simplified manner, as it assumes no phase transition from ice back to water vapour is occurring. Thus, it is treated as equivalent to purely regolith along with the gaseous term, expressed as:

$$k_2 = k_r + k_g \tag{5.15}$$

Additionally, this implies that it is assumed all ice is sublimated when $\theta_1 \to 0$. In reality, this assumption may not hold true due to incomplete sublimation of the C_i amount of ice. The apparent thermal conductivity during the phase transition can now be rewritten. For icy-regolith, we denote this as phase one, $k = k_1$, while desiccated regolith signifies phase two, k_2. The apparent conductivity then takes the form:

$$k = k_1 \theta_1 + k_2 \theta_2 = \theta_1 \left(\epsilon F k_i + k_r + k_g \right) + \theta_2 \left(k_r + k_g \right) \tag{5.16}$$

This same approach can be applied to derive the apparent heat capacity, which will be discussed in the next section.

5.2.2 Specific Heat Capacity

Employing the *Volumetric Mixing Model* outlined in section 3.4.4, one determines the specific heat capacity of icy-regolith based on the baseline heat capacity of regolith, denoted as C_{pr}, and the heat capacity of ice particles, C_{pi}. This relationship can be expressed as:

$$C_{p,1} = \frac{\rho_i \varepsilon F C_{pi} + \rho_1 C_{pr}}{\rho}, \tag{5.17}$$

where the apparent density of the mixture during all phases of transition is given by:

$$\rho = \rho_1 \theta_1 + \rho_2 \theta_2 \tag{5.18}$$

This leads to the description of desiccated regolith as phase two:

$$C_{p,2} = \frac{\rho_1 C_{pr}}{\rho} \tag{5.19}$$

Substituting these into eq. 5.10 results in the final relation for specific heat capacity:

$$C_p = \frac{1}{\rho} \left(\rho_1 \theta_1 C_{p,1} + \rho_2 \theta_2 C_{p,2} \right) + H_s \frac{d\alpha_{1\to2}}{dT}, \tag{5.20}$$

where $C_{p,1}$ and $C_{p,2}$ denote the specific heat capacities of phase one and phase two, respectively. The latent heat of the phase transition is defined as H_s, which represents the enthalpy of sublimation in this context. The term $\frac{d\alpha_{1\to2}}{dT}$ represents the rate of change of the mass fraction concerning temperature. The mass fraction, $\alpha_{1\to2}$, which represents the transition from phase one to phase two, is defined as:

$$\alpha_{1\to2} = \frac{\rho_2 \theta_2 - \rho_1 \theta_1}{\rho}. \tag{5.21}$$

The final equations result in the relations from fig. 5.4.
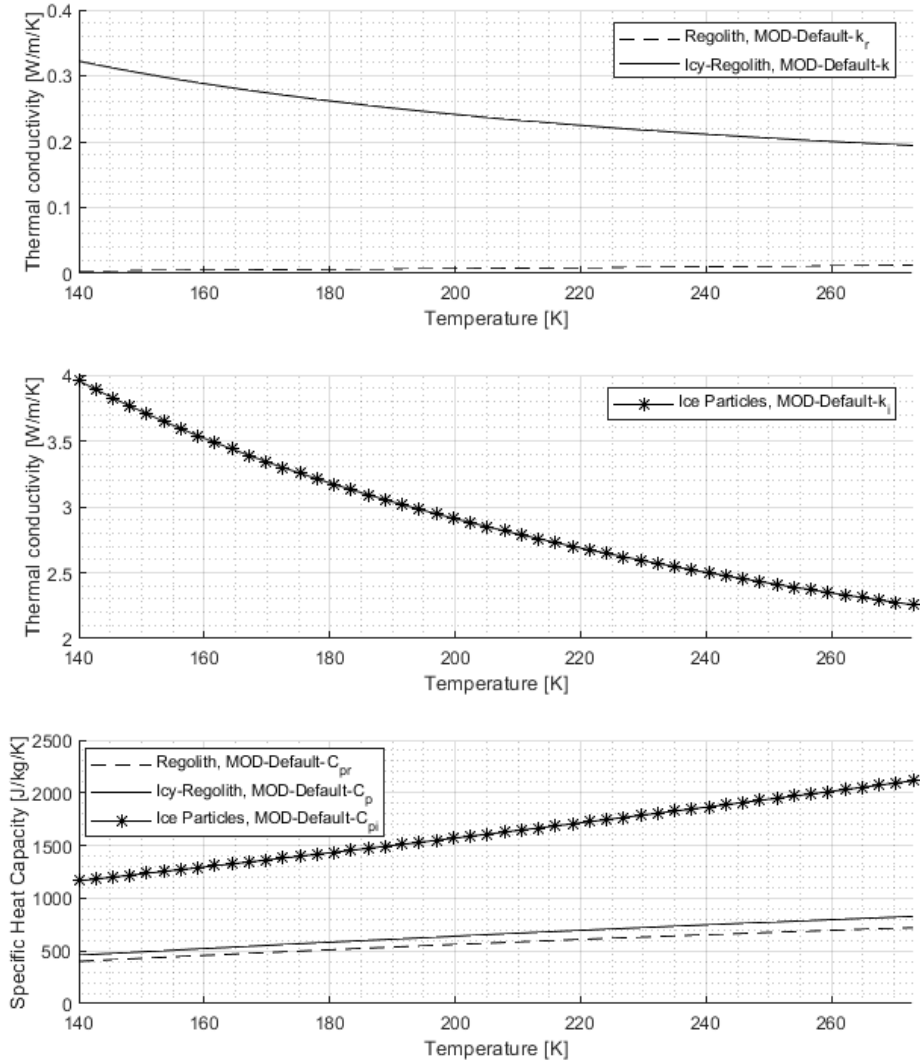
FIGURE 5.4: Thermal conductivities for regolith, ice and icy-regolith; idem for the specific heat capacity; since the thermal conductivity for ice denotes much higher values it is displayed in a separate figure for clarity; the descriptions of *MOD-Default-[var]* will be useful for later in the validation process.

5.2.3 Results for Temperature Distribution

Stirring the sample ensures an even temperature distribution as shown in fig. 5.5. The time at which these temperatures are obtained is not picked out randomly. For P = 200 W at t = 18.4 h, the sublimation curves for both rotation speeds intersect the steady configuration. For clarification, look further to fig. 9 in the appendix where the intersection of sublimation is confirmed or read the follow-up sections, figures 5.6 and 5.7. At this stage, the sublimation rate S is equal. However, the increase in the sublimation rate, i.e. dS/dt, differs a lot. The reason behind this is the fact that only near the heated surfaces, i.e. rods, the temperature is sufficient to overcome the latent heat. That would mean that the amount of sublimated water is minor, again confirmed by the figures 5.7 and 9. This leads to a minor temperature in the remaining sample, which is equivalent to the initial temperature of 140 K. The difference of the maximum and minimum temperature for rpm = 3 is only one Kelvin. Therefore, the distribution of temperature and the need for stirring is justified. Returning to the significant difference of sublimation curve, the equally distributed temperature results in a fast phase transition over the entire sample. However, this only happens when the latent heat is exceeded. In other words, the sublimation for rpm = 0 initiates faster but is of minor magnitude since it represents only the local sublimation near the rods.
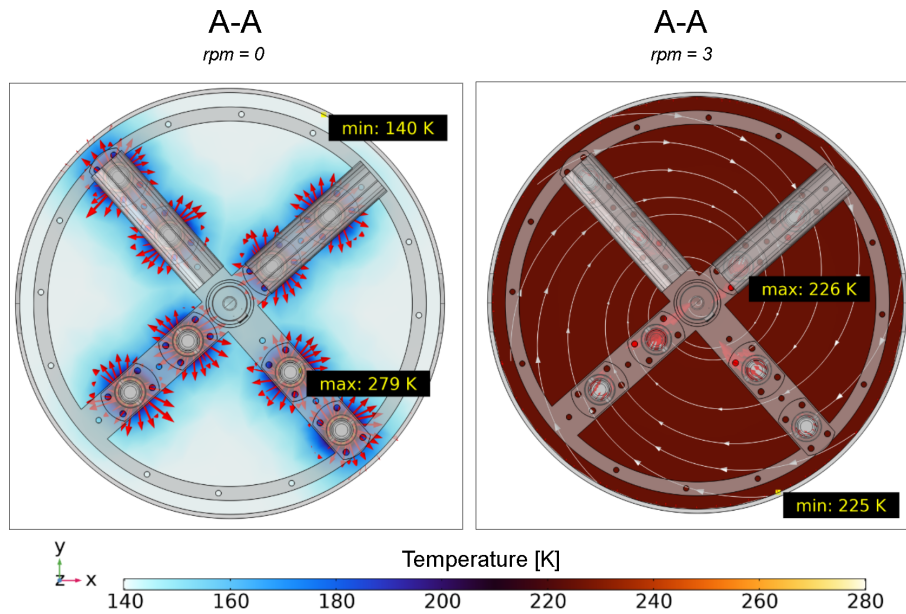
FIGURE 5.5: Temperature (volume) distribution at t = 18.4 h for P = 200 W and rpm = 0 versus rpm = 3; *note*: heat fluxes are vectored in red but have non-equal scales. The maximum heat flux for rpm = 0 is 4564 W/m^2 displayed here with a scale factor of 0.015. In turn for rpm = 3; maximum heat flux denotes only 2.5 W/m^2, its display scale factor = 20 for proper visualisation; streamlines are coloured white showing rotation along the Z-axis; both figures are represented by the same legend.

5.2.4 Baseline → rpm = 0

With a baseline condition of rpm = 0, it is straightforward to observe the timeline required for sublimation under different heating scenarios. Fig. 5.6 presents sublimation rates at two constant power inputs: 200 W and 400 W, applied throughout the extraction process. In the absence of rotation, sublimation initiates rapidly; however, it is confined to areas near the rods (cartridge heaters), where temperature gradients are high enough to exceed the water's latent heat. At 200 W, only 38% of the initial ice content has sublimated after 138.3 hours.

Given this rate, complete extraction at 200 W would weeks, an extended time frame that exceeds the scope of the current evaluation but is detailed in Appendix | B.6, Sublimation model, 3D. Under 400 W, sublimation reaches 6% of the ice content within just 16.7 hours, illustrating a significant acceleration in extraction. The maximum sublimation rate for 200 W remains at two grams per hour, while doubling the power to 400 W increases this rate by 250%, achieving a maximum of 7 grams per hour. Although power was doubled, the sublimation rate did not increase proportionally, indicating limitations due to thermal distribution. While the sublimation rate plot for $P = 400$ W shows a limited X-axis range, the behaviour it exhibits mirrors that of the $P = 200$ W case. This similarity suggests that doubling the applied power effectively shifts the graph upward along the Y-axis, representing a proportionate increase in the sublimation rate. Consequently, this shift implies that with higher power, the sublimation process accelerates while maintaining a similar extraction pattern over time. Beyond 120 hours with a 200 W input, fluctuations in the sublimation rate occur, attributed to uneven heating throughout the sample. In some regions, ice-regolith mixture reaches the phase transition temperature of 273.15 K, initiating localised sublimation, but this effect is inconsistent across the sample. These fluctuations will be discussed further in subsequent sections to analyse their impact on uniformity.
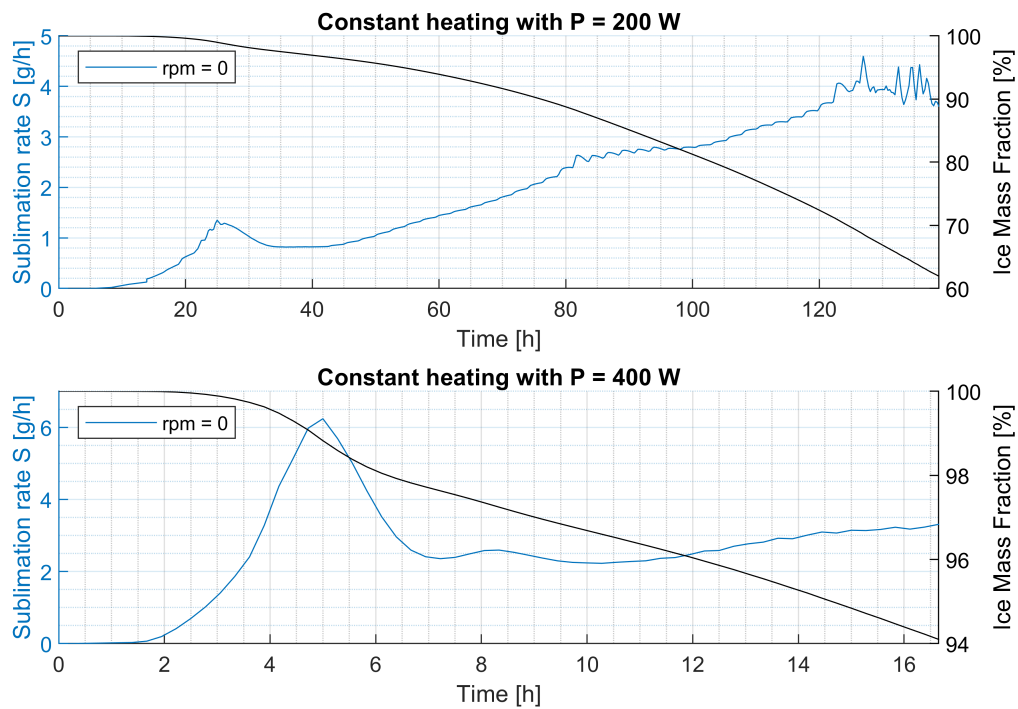
FIGURE 5.6: Sublimation rates for no-rotation; constant heating for both 200 and 400 W; right Y-axis shows the mass fraction of ice indicating the progress of sublimation; important to state is the right Y-axis is **not** scaled from 0-100% when comparing to fig. 5.7.

5.2.5 Comparison of Sublimation Rates

The heat distribution from stirring notably enhances sublimation rates in the sample. As shown in Figure 5.7, rotation rates above zero (rpm > 0) lead to significantly higher sublimation rates than the no-rotation case, where rates peak at around seven grams per hour. Both figures also exclude the initial time (t = 0), demonstrating that it takes over 18 hours at 200 W and over nine hours at 400 W to raise the regolith temperature to the sublimation temperature of 273.15 K.
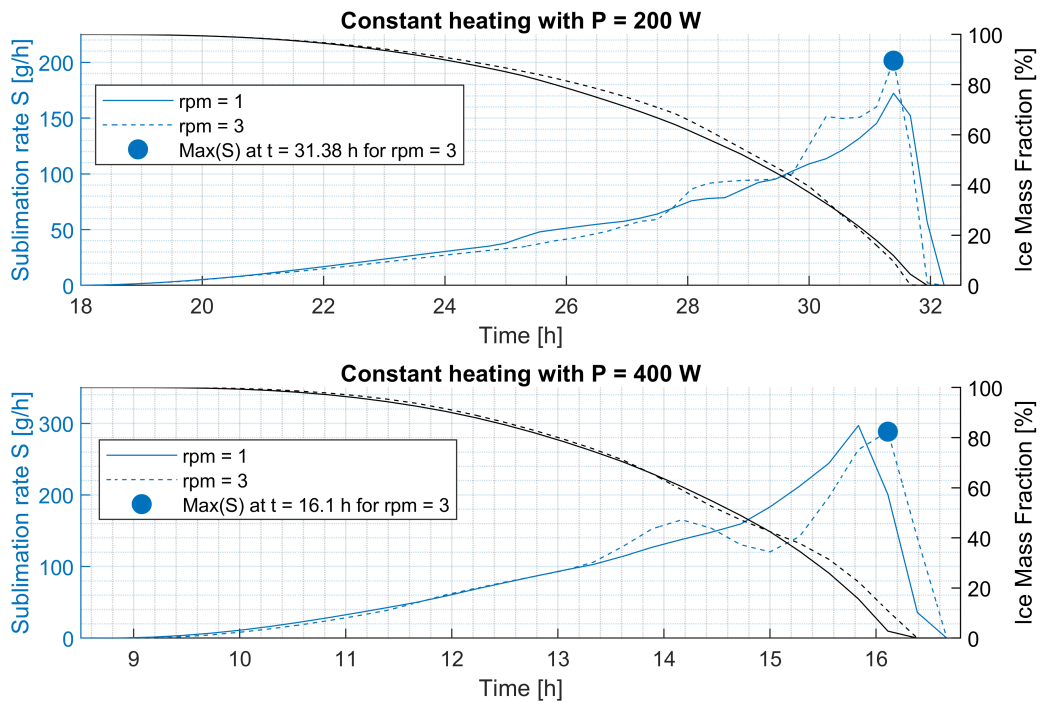
FIGURE 5.7: Sublimation rate throughout the entire extraction process, including its maximum pressure marker; *Note:* The maximum pressure/rate is only achieved at rpm = 3. The right Y-axis represents the mass fraction of ice for rpm = 1 (solid blue and black) and rpm = 3 (dashed blue and black). *Note:* For both pressure values, the sublimation rate and ice mass fraction reach zero at the same time interval, although this may not be immediately apparent at this time scale.

The following points summarise the effect of rotation on sublimation in detail:

- **Duration**:
  For rpm = 1, complete extraction is achieved in approximately 31.95 hours at 200 W and 16.39 hours at 400 W.
  For rpm = 3, the process concludes slightly faster at 31.65 hours with 200 W and matches the 16.39-hour mark with 400 W. Thus, increasing the speed by two rpm reduces the process time by 0.3 hours (or 1080 seconds).

- **Maximum Sublimation Rate**:
  -With rpm = 1 at 200 W, the peak sublimation rate reaches 172.3 grams per hour at 31.38 hours, while rpm = 3 achieves a higher rate of 201.5 grams per hour at the same time—indicating a considerable difference due to rotation.
  At 400 W, maximum sublimation is observed at 296.9 grams per hour after 15.83 hours for rpm = 1 and slightly lower at 288.4 grams per hour after 16.1 hours for rpm = 3, showing minimal variation.

- **Power**:
  For rpm = 3, doubling the power results in a rate increase factor of 1.43, while for rpm = 1, the factor is 1.72. This suggests there is an optimal balance of power and rotational speed to achieve maximum sublimation efficiency.

This analysis demonstrates that rotational speed has a significant impact on sublimation rates, particularly under lower heating power. At higher power levels, however, the effect of rotation diminishes in importance, although a positive integer speed is still necessary. Notably, slower rotational speeds, such as one rotation per minute, appear sufficient to achieve maximum sublimation

under high-power heating conditions. This analysis suggests that, in high-power heating scenarios, lower rotational speeds provide a more stable thermal environment, thereby enhancing the sublimation process. By reducing the rotational speed, heat can diffuse more uniformly, preventing thermal gradients that could disrupt sublimation and lead to less effective extraction. However, for low-power heating, higher rotational speeds are advantageous as they ensure equal heat distribution across the sample, which can minimise the extraction time. In summary, *high-power heating* benefits from lower rotational speeds for stability and uniformity, while *low-power heating* requires higher rotational speeds to improve sublimation efficiency and accelerate the process. Adjusting rotational speed based on heating power can therefore optimise the overall sublimation rate and process duration.
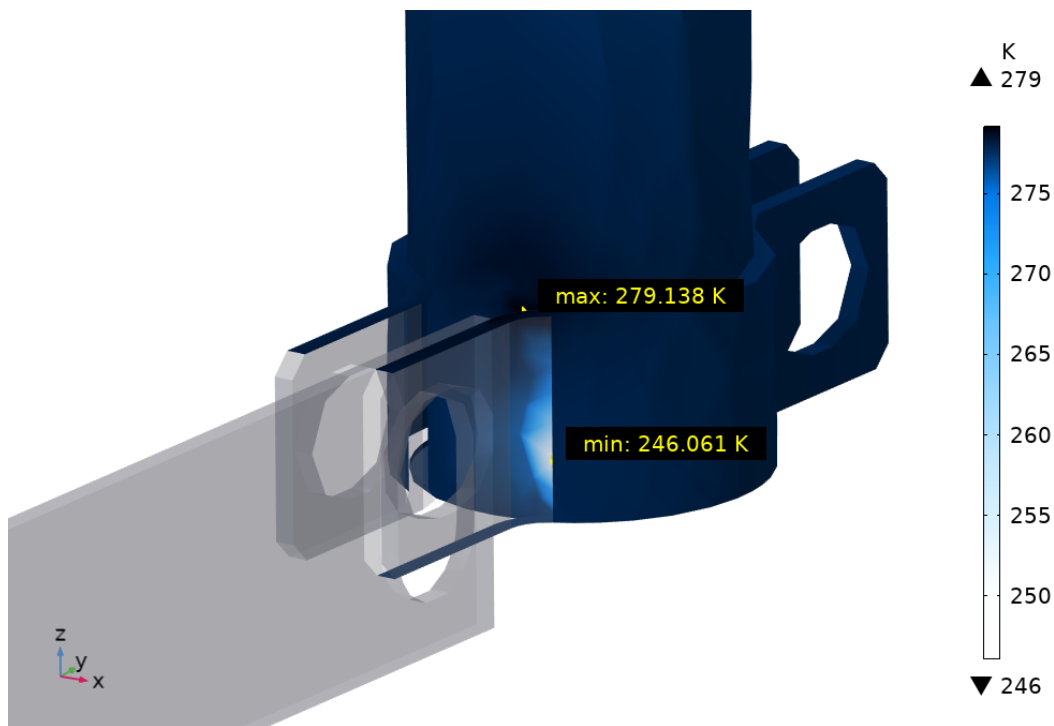
FIGURE 5.8: Constant heating of P = 400 W and rpm = 3; temperature on **boundaries** at t = 15 h from fig. 5.7 in the stirring frame/rods; significant decrease in temperature referred to as *cold spots*.

The sudden decrease in sublimation rate at three rotations per minute is caused by temporary thermal instability within the rotating icy-regolith sample. Higher rotation speeds hinder (relatively) a uniform heat distribution, leading to localised regions with insufficient heating rather than traditional overheating. These *cold spots* create temperature gradients throughout the sample, where certain regions are too cold to sustain steady sublimation. This effect is illustrated by *cold spots* in fig. 5.8. Interestingly, sublimation at rpm = 1 surpasses the speed of rpm = 3, a counter-intuitive result explained by the uneven heating at higher rotational speeds. For rpm = 1, the sublimation curve is smooth and consistent, while at rpm = 3, it fluctuates irregularly due to the instabilities introduced by higher speeds. Faster rotation shortens the time each section of the sample being near the cartridge heaters, preventing heat from diffusing evenly before another section rotates into place. Consequently, some areas reach the phase-change temperature while others remain too cold, disrupting the sublimation rate until it stabilises again. Adjustments to rotation speed or slight changes to heating power could help achieve a more uniform thermal distribution, assuming the thermal conductivity of icy-regolith remains stable across different speeds. These adjustments would help reduce temperature gradients and stabilise the sublimation rate for improved efficiency.

5.2.6 Results for Pressure Rise

Pressure within the regolith pores rises significantly during water-ice sublimation due to the formation of water vapour and resulting localised pressure gradients. These gradients, in turn, contribute to an overall increase in pressure within the entire sample volume. The combined effects of sublimation and rotational flow define this pressure rise, particularly near the heat sources (i.e. cartridge heaters), where the rotational motion of water vapour enlarge the pressure build-up. Higher rotational speeds, therefore, correlate with greater pressure rises, as faster rotation enhances pressure gradients near the heating elements. Below is a summary of these effects:

- For rpm = 3 with 200 W of heating, pressure rises by 139.4 Pa at a maximum sublimation rate of 201.5 g/h.

- When the heating power is doubled (still at rpm = 3), the maximum sublimation rate reaches 288.4 g/h, resulting in an increased pressure build-up of 151 Pa.

- When rpm tends to zero, i.e. rpm $\to$ 0, pressure build-up decreases because there is minimal rotational impact on pressure. Without rotation, the added pressure gradient from rotational flow diminishes.

- For rpm = 0, the pressure increase directly corresponds to the sublimation rate and distributes linearly across the sample. This uniform pressure distribution from the bottom to the top of the sample does not occur when rpm > 0, as the rotating flow of water vapour introduces larger irregular pressure gradients throughout the sample.

This analysis highlights the importance of rotation and sublimation rate in regulating pressure dynamics within regolith. For assessing pressure rise with respect to water's triple point (611.73 Pa), the X-axis in the figures is extended. It is evident that even at a sublimation rate of 500 grams per hour, the sample's internal pressure remains below 180 Pa. The saturation pressure of water at the triple point, i.e. 273.15 K is 611.73 Pa. Since the operational pressures are below this, the water will remain in the vapour phase. The pressure increase within the regolith pores due to sublimation reaches 137 Pa for rpm = 3 and $P = 200$ W. An additional 200 W raises the pressure to 159 Pa. For assessing pressure build-up with respect to water's triple point (611.73 Pa), the X-axis in the figures is extended. It is evident that even at a sublimation rate of 500 grams per hour, the sample's internal pressure remains below 180 Pa. The saturation pressure of water at the triple point, i.e. 273.15 K is 611.73 Pa. Since the operational pressures are below this, the water will remain in the vapour phase.

5.3 Enhancement of Thermal Conductivity

Analysing the cause for achieving a uniform temperature within the rotating regolith sample is interesting. This section is dedicated to examining the influence of rotation on thermal conductivity, focusing specifically on how the effective thermal conductivity is affected by the rotational motion.

5.3.1 Mathematical Approach

To calculate the effective thermal conductivity of a sample under rotation, it is essential to consider both the thermal conductivity of the material and the effect of rotational motion. The rotational motion can influence heat transfer due to the additional effects caused by the rotation. To derive the effective thermal conductivity k_{eff}, consider the energy balance in a small control volume within the rotating system, explained in appendix |B, specifically § B.4 *Enhancement of Effective Thermal Conductivity*. The rotating term adds a form of enhanced thermal transport. The total heat flux $\vec{q}$ can be modified to include the contribution from rotation:

$$\vec{q} = -k_{\text{eff}}\nabla T + \rho c_p(\vec{v}T).$$

where its enhancement in conductivity due to rotation depends on the radial distance from the axis, angular velocity, and the specific heat capacity of the material.

$$k_{\text{eff}} = k_r + \beta\rho c_p\omega r^2,$$
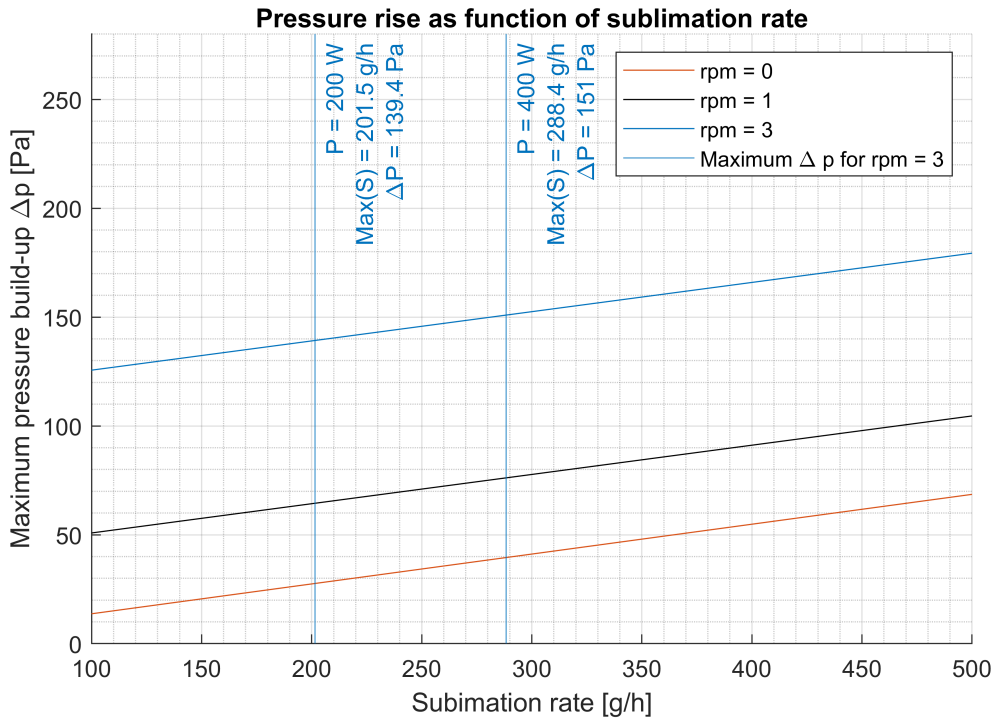
FIGURE 5.9: Pressure rise as function of sublimation rate; *Note:* pressure rise corresponds to higher sublimation rates than achievable at lower rpm values, i.e. rpm = 1 and 3.

Here β is a factor dependent on the material and geometry, r is the radial distance from the rotation axis. Using curve fitting, an optimised value is determined for $\beta = 0.000078$. For understanding the mathematical approach, read appendix |C, specifically topic § C.3 *Curve Fitting*. The thermal conductivity of raw and dry regolith is still denoted k_r.

5.3.2 Enhancement of k_{eff}

The plot shows that k_{eff} remains significantly higher across the temperature range (140–300 K), with the data points (indicated as *Data Points without Outlier*) closely following the fitted curve. This fitted curve deviates considerably from the baseline thermal conductivity k_r, represented by a dashed line, especially at lower temperatures where the enhancement effect is more pronounced. As s results the following is observed:

- The increase in thermal conductivity suggests that rotation mitigates the insulating effects inherent to the porous structure of regolith, by continuously shifting contact points and promoting thermal interactions between particles.

- Despite the vacuum conditions typically limiting heat transfer, rotation induces a convective-like effect that increases thermal conductivity. This effect becomes especially useful at greater radial distances or greater surface surfaces, where particle motion disrupts insulating voids and improves particle-wall contacts.

- The effective thermal conductivity under rotation is observed to be up to approximately 75 times the thermal conductivity k_r at certain points, as indicated by the fitted curve. This significant increase aligns with the hypothesis that rotational motion improves thermal transport, countering the insulating properties of the sample.

The effective thermal conductivity due to rotation is influenced by both the intrinsic thermal conductivity of the material and the rotational speed, geometry, and other material properties.
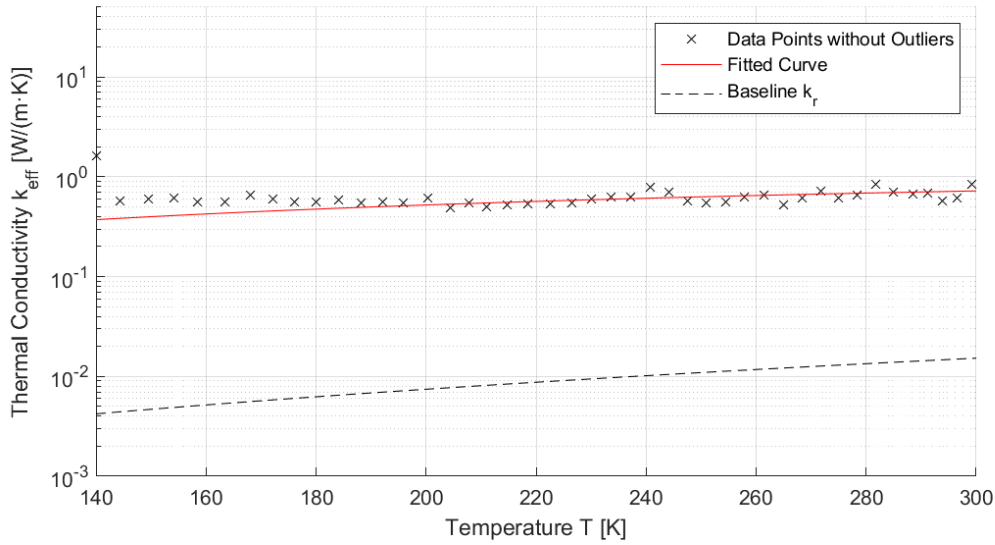
FIGURE 5.10: Data points of effective thermal conductivity fitted over the function $k_{eff} = k_r + \rho\omega\beta C_p r^2$; where $\beta = 0.000094$; $\rho = 1470$ kg/m^3, $\omega = 0.314$ rad/s (3 rpm), $r = $ R $= 0.15$ m, $C_p = C_p(T) = C_{pr}$; at this stage data points are obtained by simulation not by measurements in experimenting; rotating regolith results in effective thermal conductivity of 0.3-1 W/m/K with respect to dessicated Lunar regolith not reaching higher values of 0.02 W/m/K for T < 300 K.

As the particles rotate, they move relative to each other, which improves contact points between individual particles and particle-wall interactions. In a static configuration, thermal resistance, due insulated properties of regolith, is high at these contact points due to limited surface area contact. Rotation constantly shifts the contact regions, reducing thermal resistance, and enhancing heat transfer between particles. In addition, the radiative conduction and k_g-component between heated rods and particles is increased as well. Particles that rotate expose more surface area to the heated rods and to each other, maximising radiative heat exchange. In terms, of heat exchange to the ambient, the constant motion allows heat to be kept inside the domain more effectively, reducing the rate of heat loss to the ambient.

As the stirring mechanism rotates, the heat from the rods is distributed more uniformly throughout the domain. Without rotation, heat accumulates fast around the rods, causing thermal gradients and localised overheating. Rotation breaks these gradients, spreading heat more evenly and enhancing the overall thermal conductivity. In a static domain, the void spaces in the regolith act as insulators, due to vacuum conditions, reducing heat transfer. As the particles rotate, these void spaces are disrupted, reducing the insulating effects and allowing heat to flow more freely throughout the domain, increasing the effective thermal conductivity. These phenomena lead to an increase in thermal conductivity 35-75 times the baseline k_r. In other words, due to rotation the effective thermal conductivity is 75 times higher at its extreme than Lunar regolith conductivity.

The findings suggest that even under low-pressure environments, rotational motion can dramatically improve heat transfer. The curve fitting approach successfully models this enhanced conductivity, with β calibrated to represent the material's specific response to rotation. In conclusion, this study demonstrates that rotational motion can effectively increase thermal conductivity by overcoming the natural properties of regolith. The enhancement observed here could have broader implications for thermal design in water extraction applications.

5.4 Rotational Flow Dynamics

As the water vapour rotates, it experiences a force pushing it outward, resulting in a radial pressure gradient. In fig. 5.2 one sees the sublimated water escaping from the surface. Ideally, the rotational force by the stirring mechanism has no influence on the water vapour flow towards the exit, i.e. the vapour tube. However, forces arise from the effects of rotation and influence the dynamics of water vapour within the rotating mechanism. Centrifugal force is the apparent force experienced by the stirring mechanism, pushing water vapour outward from the axis of rotation. This force is given by Goldstein and Safko [1980], Landau and Lifshitz [1976]:

$$\mathbf{F}_{\text{centrifugal}} = m\,\boldsymbol{\omega} \cdot (\boldsymbol{\omega} \cdot \mathbf{r}) \tag{5.22}$$

Here m defines the mass of water vapour, $\boldsymbol{\omega}$ is the angular velocity vector of the stirring mechanism, and radius $\mathbf{r}$ denotes the position vector of water vapour relative to the axis of rotation. This force acts radially outward from the axis of rotation. Another effect is caused by the so-called Coriolis force which acts on the water vapour moving within the stirring mechanism, causing them to be deflected perpendicular to their direction of motion. The Coriolis force influences flow patterns causing the water vapour to take a curved path rather than a straight one. This force is expressed as Fowles and Cassiday [1977]:

$$\mathbf{F}_{\text{Coriolis}} = -2m\,(\boldsymbol{\omega} \cdot \mathbf{v}')$$

where $\mathbf{v}'$ is the velocity of water vapour relative to the rotating mechanism. The Coriolis force results in a sideways deflection, which depends on the upward velocity of water vapour due to sublimation and the angular velocity of the stirring mechanism. It might not be relevant due to the low angular and upward velocities, relatively. Nevertheless, the Euler force is experienced in a non-uniformly rotating frame, where the angular velocity is changing over time. Although, the rotational speed of the stirring mechanism is assumed to be constant, it is interesting to see what the effects are on outgassing, if one would change the rotational speed. The Euler force is given by the following equation where $\frac{d\boldsymbol{\omega}}{dt}$ defines the time derivative of the angular velocity vector Symon [1971]:

$$\mathbf{F}_{\text{Euler}} = -m\,\frac{d\boldsymbol{\omega}}{dt} \cdot \mathbf{r} \tag{5.23}$$

To facilitate the effective exit of water vapour through the outlet, an upward axial velocity is essential. This upward velocity must overcome the centrifugal, Euler and Coriolis forces generated by the rotation. Achieving a steady-state condition requires that the upward velocity due to sublimation be strong enough to overcome the combined forces, thus ensuring a continuous flow of water vapour from the regolith to the outlet.

5.4.1 Mathematical Approach

When rotating a porous medium, an adaptation to the current model must be made. Since Darcy's law does not consider a free flow, one needs to implement another phenomenon. A *free flow* can be considered as overall fluid behaviour. In this case, rotation adds fluid dynamics that contribute to this overall fluid behaviour. Darcy's law determines the flow behaviour through the microstructure of regolith due to pressure changes. However, it does not account for velocity gradients based on inertial effects LAGE [1998]. *Note:* Darcy's velocity field is calculated based on regolith's permeability which does not address momentum of a fluid. Take a look at the equation of motion described in the appendix A | *Fundamental of Fluid Dynamics*. Here, the transient term defined as $\rho\partial v/\partial t$, and convective term represented by $\rho v(\nabla v)$, are assumed to be negligible according to Darcy's law. Additional, permeability functions as an empirical material property, directly relating pressure and flow velocity. This means that Darcy's law simplifies flow by using a empirical relationship of the permeability term. In short, Darcy's law is very practical for steady viscous flows with low Reynolds numbers. To account for the rational impact of flow through regolith, the so-called Brinkman's equations are used Yano et al. [1991]. By extending Darcy's law with these equations, one can capture the velocity gradients due to rotation. Together, a free flow described

by Brinkmann and Darcy's porous flow, it is possible to analyse the rotational conditions on outgassing the water vapour. To assess the influence of these rotational dynamics on the flow, it is necessary to calculate the transmission of vapour between the outgassing surface of the regolith and the outlet of the crucible:

$$\overline{T} = \frac{\int_{S_{out}} J_{I,H2O}}{\int_{S_{in}} J_{E,H2O}}. \tag{5.24}$$

Here transmission $\overline{T}$ is defined a ratio between the total incident molecular flux at the outlet over the emitted flux from the regolith. Therefore the specific surfaces are evaluated as:

- $S_{out} = \pi R_{VT}^2$ which represents the surface area of the vapour tube with radius $R_{VT} = 18.5$ mm. Since the water vapour needs to flow towards the vapour tube it is considered the exit or outlet.

- S_{in} defines the top surface area of the sample. Since this area is not homogenous throughout the sample it cannot be analytic evaluated.

- $J_{E,H2O}$ in $1/(\mathrm{m}^2 \cdot \mathrm{s})$ is derived from the sublimation rate, the Avogadro constant $N_A = 6.02214076e23$ [1/mol] and surface area S_{in}.

5.4.2 Impact of angular velocity ω on Outgassing

This model is specifically adapted for a continuum flow regime where the Reynolds number is significantly below one. Modelling the combined effects of free molecular flow, rotational dynamics, and the interactions between the stirring mechanism and water vapour proved computationally intensive, necessitating this simplification to observe the rotational impact. Consequently, the focus of the results is on comparing transmission outcomes at various rotational speeds, rather than ensuring high accuracy in the absolute transmission values.

Transmission results are captured once they reach a steady state, indicated by minimal fluctuations over time. This steady state signifies fully developed flow under rotational conditions, at which point rotational forces no longer influence the outgassing behaviour.

The results demonstrate a decline in transmission when rotational dynamics are applied. Specifically, at a rotation speed of one rotation per minute, the transmission $\overline{T}$ stabilises at approximately 0.98. However, with an increase in speed to three rotations per minute, transmission values fall below 0.9, indicating a significant reduction. These findings provide preliminary insights into the behaviour of transmission under varying rotational speeds. For higher rotation rates, transmission does not settle at equilibrium and exhibits substantial fluctuations. These fluctuations may be attributed to irregular flow patterns influenced by present forces, but this cannot be confirmed with complete accuracy. Therefore, these results should be interpreted with caution.

5.4.3 Impact of gravity g on Outgassing

Visualising the effect of gravity is insightful. Given that the Moon's gravity is about six times weaker than Earth's, it influences the outgassing of water vapour from the sample. With the icy-regolith mixture modelled as a porous structure, the effect of gravity on water vapour flow through the regolith pores is analysed and detailed in below first section. Additionally, the gravitational forces impacting water vapour flow toward the capturing subsystem are examined.

- Lunar gravity denotes 1.62 m/s^2.
- Gravity on Earth is defined by a value of 9.81 m/s^2.

Previous results indicated a reduction in transmission when rotational dynamics were introduced. However, these initial simulations did not include gravitational forces. To evaluate the influence of gravity, the water vapour flow was re-simulated under the same conditions with gravitational effects included.

The data reveals that at higher rotational speeds, gravitational forces start to impact transmission noticeably. Specifically, as the flow reaches a fully developed state, differences in transmission become apparent. Transmission is shown to be lower under higher gravity, such as Earth's, suggesting that rotational flow on the Moon would operate more efficiently than on Earth. Nonetheless, given the partial validation status of the outgassing transmission data, these comparisons are not utilised in further calculations.

5.5 Coupled Flow

The effect of rotation on water vapour exiting the crucible is discussed in Section 4.5 | *Rotational Flow Dynamics*. It is shown that centrifugal forces help to decrease backflow but also limit effective flow through the vapour tube. Therefore, considering the impact of rotation, the flow behaviour, and resulting mass fluxes require further investigation. This implies that the sublimation rate is influenced by the stirring mechanism, leading to variations in fluxes reaching the cold trap.
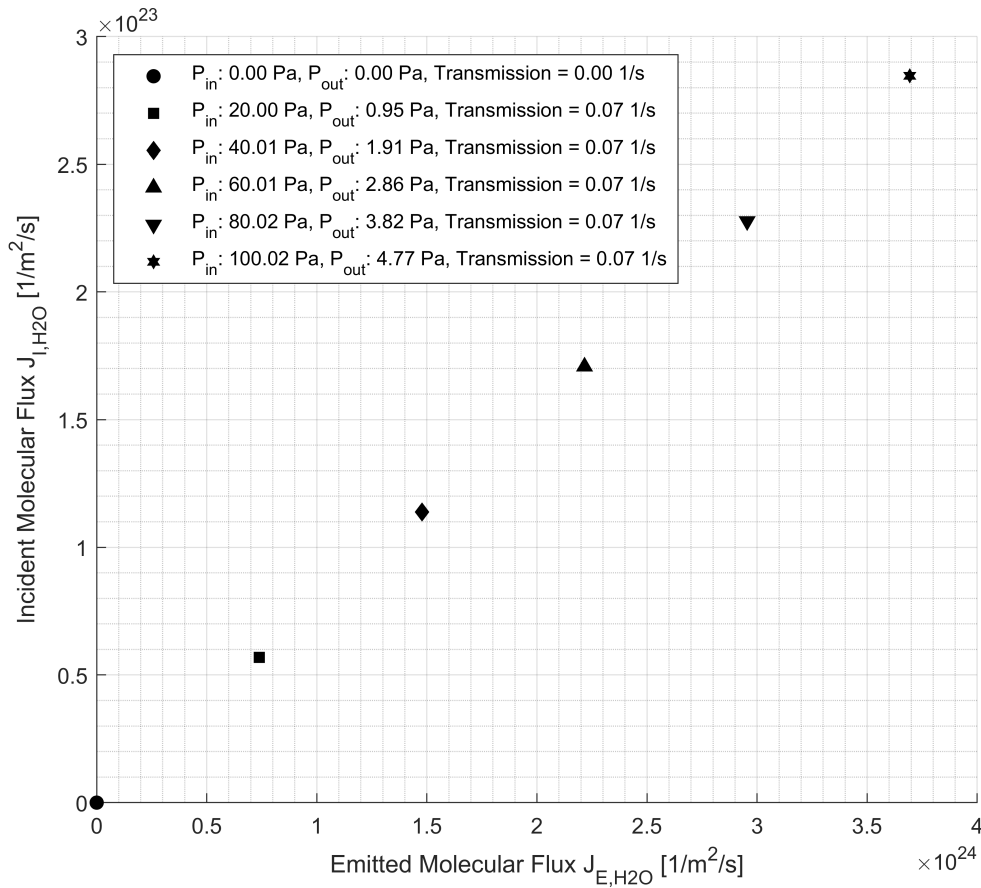
FIGURE 5.11: Transmission $\overline{T}_2$ of water vapour calculated in section 5.5.1 defining the ratio of molecules passing through the vapour tube, eventually reaching the cold trap.

5.5.1 Mathematical Approach

The emitted molecular flux from the crucible exit, as shown in fig. 4.3, represents the flux of molecules leaving the crucible and entering the vapour tube. For optimal performance, a high

outgassing rate is necessary to ensure that the incident molecular flux reaching the cold trap (or the exit of the vapour tube) is substantial. To investigate the relationship between these fluxes within the vapour tube, a free molecular flow of water vapour is maintained through the tube, ensuring sufficient velocity as the vapour enters the cold trap.

The vapour tube exit is assumed as an outlet under the condition that the deposition rate within the cold trap is high enough to prevent extreme pressure gradients. This assumption ensures that no backflow occurs from the cold trap into the vapour tube. Given this setup, the incident flux reaching the cold trap can be calculated under steady-state conditions. This steady-state approach holds only if the cold trap captures vapour molecules at a sufficient rate, ensuring low pressures and a unidirectional flow directed towards the cold trap trap. This relationship is depicted in fig. 5.11 and is derived from eq. 5.24, with one key difference:

$$\overline{T}_2 = \frac{\int_{S_{out}} J_{I,H2O}}{\int_{S_{in}} J_{E,H2O}}. \tag{5.25}$$

- S_{out} defines the cross-sectional area of the vapour tube entering the cold trap and is therefore considered the exit or outlet.

- S_{in} defines the cross-sectional area of the vapour tube at the inlet.

- $J_{E,H2O}$ in $1/(\mathrm{m}^2 \cdot \mathrm{s})$ is derived from the sublimation rate, transmission $\overline{T}_1$ from section 5.4 and surface S_{in}.

5.5.2 Water Vapour Flow towards Capturing

The figure illustrates a linear relationship between the emitted flux from the inlet and the incident flux that reaches the cold trap, as shown in Fig. 5.11. This indicates that transmission remains constant for different emitted fluxes, with the incident flux adjusting accordingly. The free molecular flow reaches equilibrium through mass conservation. The pressure at the outlet is equivalent to the ambient pressure, i.e. the pressure inside the TVAC. At this equilibrium point, transmission stabilises at 7%, meaning that 7% of the water vapour molecules reach the cold trap per second. Time integration is not applicable because the solution is calculated for equilibrium, not in a transient state. Nevertheless, the transmission serves as a good indicator of how the water vapour flows toward the cold trap.

5.6 Model Development and Optimisation

For this stage in the water extraction process, there is not a lot to optimise. Since the operational variables only involve the heating elements and stirring mechanism, these are the variables to optimise. However, current models can be extended with accurate mass transfer. In this case, in stead of just using Knudsen diffusion, D_K, one can determine the molecular fluxes over the boundaries of a Lunar regolith sample.

5.6.1 Cartridge Heaters

Research by Hao et al. [2023] suggests that lower-temperature heating is more efficient for water extraction, as high-power heating leads to rapid sublimation of water-ice near the cartridge heaters. This rapid sublimation significantly reduces the effective thermal conductivity, ultimately prolonging the time it takes for heat to diffuse through the icy-regolith mixture. However, as demonstrated in sections 5.2.3 and 5.3, the results indicate that localised ice sublimation does not occur during sample stirring. Consequently, the effective thermal conductivity remains high, as shown in fig. 5.10, surpassing 1 W/m/K. The primary consideration in this process is temperature control, ensuring the maximum temperature does not exceed 333.15 K. This threshold is selected to prevent overheating of the cartridge heater, which is a product performance specification.

When heating at a constant 400 W, the maximum temperature can exceed 900 K, depending on the rotational speed. As rotation speeds increase, the maximum temperature decreases, since rotation ensures uniform temperature distribution, as discussed in previous sections. This even distribution prevents large temperature gradients, which in turn keeps the maximum temperature near the cartridge heater lower. The process of sublimation including temperature control regarding the cartridge heaters is rediscussed in Chapter 8 | *Validation & Analysis*.

5.6.2 Rotational Speed

The primary drawback of high rotational speeds during the sublimation process is the potential formation of *cold spots*, as illustrated in fig. 5.8 and discussed in section 5.2.5. These cold spots can introduce fluctuations in the sublimation rate. Although the sublimation process concludes at the same time across different rotational speeds at a constant power $P = 400$ W, the configuration with 3 rpm achieves full sublimation 1080 seconds faster than 1 rpm under low-power heating conditions.

However, this difference in completion time is insufficient to determine an optimal rotational speed, so other factors should be considered. For instance, examining the pressure increase within the regolith pores, as shown in fig. 5.9, reveals that even at the evaluated sublimation rate, the peak pressure is significant below water's triple point (611.73 Pa), allowing for tolerance in pressure. *Note:* The current pressure gradients are evaluated throughout the pores of the icy-regolith mixture. When the outgassing rate towards the vapour tube is insufficient, an additional pressure build-up occurs in the empty space ($> z_{LVL}$) within the crucible. Another option is temperature control. If the temperature limit of 333.15 K is reached, power input would automatically reduce to maintain a constant temperature $T_{\max} \leq 333.15$ K instead of constant power. At this controlled temperature, the chance of forming cold spots decreases, even at higher rotational speeds, due to significantly lower temperature gradients.

Thus, simulation results provide no conclusive reason to determine a particular rotational speed. Experimental testing, however, will be essential to determine the optimal rotational speed, which will be revisited in Chapter 8 | *Validation & Analysis*.

5.6.3 Diffusion

In free molecular flow, where gas molecules rarely interact with one another and mainly collide with pore walls, the Knudsen diffusion coefficient becomes an important parameter as explained in section 5.1.4. However, for water extraction, external heat is applied, by the cartridge heaters. External heat alters the flow conditions.

5.6.4 Mathematical Approach

Considering small pores of regolith and low pressure values in vacuum conditions, the Knudsen number can transition between a **Transition Flow** ($0.1 \leq \mathbf{Kn} < 10$) and a **Free Molecular Flow ($\mathbf{Kn} \geq 10$)**. This means, the mean free path of water vapour becomes larger with respect to its pore size. When such a transition occurs, the Knudsen number changes accordingly and the application of Knudsen diffusion becomes more important. In turn, it means that at lower values of the Knudsen number, diffusion cannot be only evaluated by Knudsen. Therefore, to go around the Knudsen diffusion, one has to consider the mass diffusion coefficient of water vapour flowing through the pores of regolith. By implementing a free molecular flow in a simulated geometry of regolith, one can calculate its molecular diffusion. In such cases, the diffusion coefficient D can be evaluated based on flux $\mathbf{J}$ integrated over the boundary Γ and the concentration gradient, $\Delta\phi$, as follows:

$$D = \int \mathbf{J} \, d\Gamma \frac{1}{\Delta\phi}, \tag{5.26}$$

where $\Delta\phi$ represents the concentration density between the inlet and outlet of the porous structure (in mol/m^3).

The concentration density is calculated based on the incident molecular flux at the inlet and the emitted flux at the outlet. Fig. 8 in Appendix B.9 illustrates the molecular flux across a porous regolith slab, determined via image processing techniques (as detailed in Appendix B.9). Because free molecular flow is sensitive to pressure and temperature distributions, accurately calculating fluxes require assessing local pressure and temperature values within each pore. This approach into the new diffusion coefficient provides a better insight into transport properties within small-pores.

5.6.5 Results for Diffusion

The molecular flux and vapour concentrations at the inlet and outlet are calculated according to eq. 5.26. Notably, the diffusion coefficient remains constant, irrespective of pressure gradients across the slab, as shown in fig. 5.12. At a standard temperature of 273 K, the diffusion coefficient reaches a value of $0.185\,\text{mm}^2/\text{s}$. Temperature fluctuations significantly affect diffusion. For example, with a 1 K temperature difference between inlet and outlet in a rotating setup (fig. 5.5), the diffusion coefficient remains near the baseline of $0.185\,\text{mm}^2/\text{s}$. However, for no-rotation case, i.e. rpm = 0, larger temperature deviations are observed due to the proximity of cartridge heaters, which can lead to significant spatial variations in temperature (ΔT) across the domain (see Figure 5.12). This spatial temperature gradient obtains the importance of heat for controlling mass transport within the porous regolith.
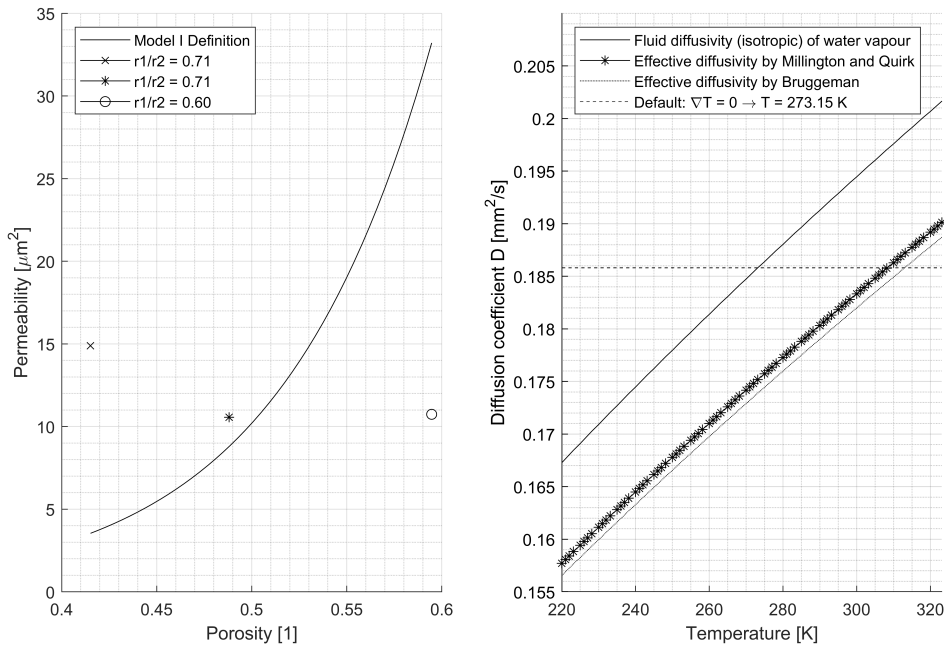
FIGURE 5.12: Diffusion coefficient as a function of temperature; at T = 273.15 K, diffusion coefficient D is considered default value which denotes $0.185\,\text{mm}^2/\text{s}$.

5.6.6 Effective Diffusion Coefficient

The effective diffusion coefficient D_{eff} for water vapour moving through porous regolith is influenced by the porosity ϵ and tortuosity τ, as expressed in eq. 5.27. Here, D represents the diffusion coefficient of water vapour, previously derived, with the assumption of isotropic diffusivity. This means the diffusion process behaves equivalently in all directions.

Tortuosity, characterises the complexity of the pathways within the regolith; a higher tortuosity indicates more twisted or indirect paths, which reduces the effective rate of diffusion.

$$D_{eff} = \frac{\epsilon}{\tau} D \tag{5.27}$$

To estimate tortuosity, two models are considered. The *Millington-Quirk model* relates tortuosity to porosity with the expression:

$$\tau_{MQ} = \epsilon^{-1/3}, \tag{5.28}$$

as found in Hillel [1971], making it suitable for regolith samples with more uniform, well-connected pore structures. Alternatively, the *Bruggeman model* approximates tortuosity as:

$$\tau_B = \epsilon^{-1/2}, \tag{5.29}$$

a formulation that better captures the diffusion behaviour in materials with irregular shapes and variable pore sizes, where void connectivity is poor , as noted in Bruggeman [1935]. Both models offer distinct advantages depending on the structural characteristics of the regolith, and due to limited data on Lunar regolith, both models must be considered at this stage for estimating diffusion. Simulation results (fig. 5.12) indicate only slight differences in effective diffusivity between the models across various temperatures, mainly due to the differing tortuosity factors. However, the baseline diffusion coefficient of water vapour remains relatively high. Future modelling of water vapour transport through regolith can leverage these insights to account for diffusion within Lunar regolith.

5.6.7 Validation

The extent and impact of the cold spots discussed in section 5.2.5 require careful evaluation, as they indicate extreme temperature gradients reaching approximately 33 K. These gradients may partly result from boundary conditions, especially since thermal insulation is applied across the boundaries in the stirring mechanism. This boundary condition enforces a thermal gradient by preventing heat from dissipating efficiently. However, the cold spot appears at the interface between the stirring mechanism and the regolith, suggesting that the gradient arises from non-uniform heat diffusion rather than solely from the boundary condition itself. Nevertheless, the influence of the boundary condition on enforcing this phenomenon should be considered.

The sublimation rates shown in figures 5.7, 5.6, and 9 were calculated using a time step size of 1000 seconds. These simulations are computationally intensive, often requiring several weeks to complete, showing the high computational cost involved. While reducing the time step size would increase the model's accuracy, it would also extend the simulation time significantly. This trade-off between computational efficiency and model precision must be carefully managed to achieve reliable results.

The system parameters, detailed in Table 5.1, include the transition interval for temperature. Based on the Heaviside step function shown in fig. 5.3, ΔT specifies the temperature threshold where sublimation begins. The default setting for this interval is 100 K, allowing the sublimation process to proceed smoothly under simulation conditions. However, in practice, sublimation initiates at the phase change threshold $T_{pc} = 273.15$ K. When the temperature interval ΔT is reduced, solver divergence occurs, suggesting that the *Volumetric Mixing Model* may not fully capture the behaviour of the system. This divergence could also be influenced by how porosity is defined. Currently, porosity is calculated based on density, which implies that regolith particles are assumed to be uniformly packed. In reality, various packing configurations are possible for regolith particles within a given unit of void, affecting the accuracy of the model which will be further discussed in Chapter 8.

6 | Stage II: Deposition

Once sublimation occurs, the water vapour travels through the vapour tube towards the capturing system. As the vapour enters this system, the free molecular flow of water molecules is directed toward the copper cold finger, which is maintained at low pressure and temperature. This environment encourages the water vapour to transition into solid ice upon contact with the cold finger's surface. Essentially, the vapour deposits onto the cold finger, marking the commencement of the next stage in the water extraction process: **deposition**.
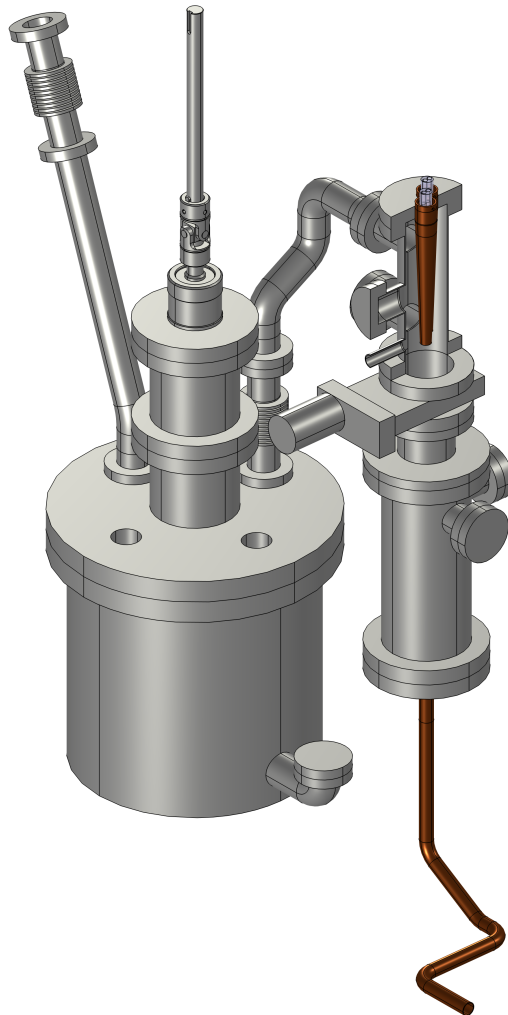
FIGURE 6.1: The complete water extraction system setup is shown, featuring two cold fingers positioned inside the cold trap.

6.1   Methodology

Water vapour enters the cold trap and flows towards the cold fingers, which play a crucial role in the deposition process. The cold fingers are equipped with heating elements inside a cone-shaped structure to manage thermal control. The figure (referenced as 6.2) provides a transparent cross-section view of a cold finger, highlighting the placement of a heating sensor at the bottom. This sensor monitors the temperature closely, ensuring control over the heating process. Additionally, a hole for wiring is visible inside the cold finger, allowing for easy connection of the sensor to the control system. The cold fingers are welded securely to the top of the housing, ensuring thermal connectivity and minimising heat loss to the surroundings.
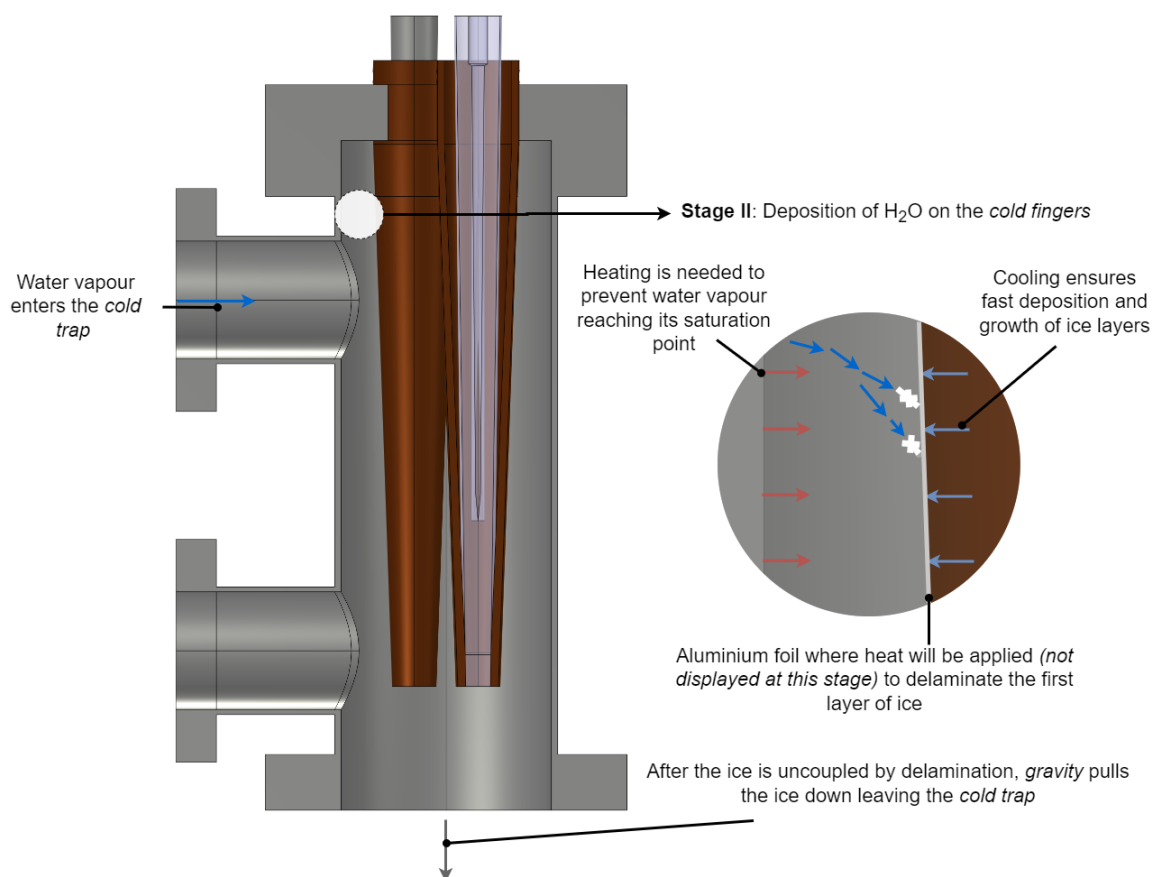
Figure 6.2: Working principle of capturing water vapour; the inner material of the right cold finger is transparent to visualise wiring, space for magnesium-oxide to enhance thermal behaviour and geometry of the copper cone.

To further reduce heat dissipation and maintain efficiency, the housing around the cold fingers is externally heated. This prevents the water vapour from reaching its saturation point prematurely, ensuring that phase transition occurs only at the designated cold surfaces. Ideally, the temperature of the water vapour is kept constant at 273.15 K, the freezing point of water. By maintaining this temperature, the vapour remains in a gaseous state until it contacts the surface of the cold finger, where it transitions into solid ice. The formation and density of this ice frost layer depend on the operating conditions, such as the temperature of the cold fingers and the rate at which the water vapour is supplied. Faster cooling promotes rapid deposition, leading to thicker ice layers, while the deposition rate itself influences the required cooling rate. In other words, the balance between the cooling rate and the deposition rate determines the overall efficiency of the ice growth process. As the ice builds up over time, the phase change occurs at a moving interface known as the phase change interface (PCI). This interface represents the boundary where the water vapour transitions

into ice. The growth of the ice layer continues as long as there is a temperature gradient and an adequate supply of water vapour. Once equilibrium is reached no more ice will form on the surface. At this point, delamination becomes necessary. Delamination refers to the process of removing the accumulated ice from the cold finger surface. By removing the a minimum layer of ice, the amount of ice can fall down towards the liquefaction chamber.

Variable	Discription	Default value	Unit
q_{del}	Heat flux for delamination	7211.1	W/m^2
k_s	Thermal conductivity of solid ice	$k_i(T)$	W/m/K
k_f	Thermal conductivity of water vapour (fluid)	$k_{wv} = 0.0165$	W/m/K
$C_{p,s}$	Heat capacity of solid ice	$C_{pi}(T)$	J/kg/K
$C_{p,f}$	Heat capacity of water vapour (fluid)	1864	J/kg/K
d_p	Particle diameter of regolith	43.6	
T_0	Initial / Ambient temperature	140	K
T_h	External heating temperature	273.15	K
T_c	Internal cooling temperature	150	K
δ_{in}	Initial ice frost thickness	0.01	mm
r_0	Effective radius of cold finger	10	mm
L_0	Maximum reference length of fluid domain	33	mm
p_0	Pressure inside vacuum chamber	1e-4	Pa
μ_f	Viscosity of water vapour	1.7e-5	$Pa \cdot s$
H_s	Latent heat of sublimation for water	2834	kJ/kg

TABLE 6.1: System parameters and variables for stage II; deposition including the process of delamination.

6.1.1 Mathematical Model

The ice deposition model describes an interface that moves outward along the positive r-direction, as shown in fig. 6.3. The cold finger's outer radius, r_0, represents an effective radius derived from the top and bottom radii of its cone shape, where symmetry holds at $r = 0$. This effective radius simplifies 1D modelling, allowing for accurate representation in a conical geometry.

An initial frost thickness, δ_{in}, is introduced to model the moving interface. Although there is no such frost layer initially in a real setup, it is necessary in simulations to prevent the interface from being defined directly at the cold copper surface, $r = r_0$. The initial frost thickness δ_{in} is set to 0.01 mm, based on findings that a minimum layer of this thickness allows reliable modelling of the moving interface in 1D, as supported by Brèque and Nemer [2016]. Attempts to mesh layers thinner than 0.01 mm in COMSOL showed poor accuracy, making this thickness an effective compromise for capturing the interface.

The 1D model also assumes uniform ice growth across the entire cold finger. However, actual ice deposition varies, as water vapour flow distribution strongly influences deposition rates. Specifically, molecular flux is highest near the vapour tube (outlet) aligned with the cold finger's surface, while lower fluxes are observed on regions further from this point. Consequently, the assumption of uniform ice growth in 1D modelling holds best for the areas with sufficient water vapour flow. This observation suggests that refining the cold trap's design may improve uniformity, though homogenous ice growth is still expected in the regions of highest vapour concentration.

As water vapour enters the cold trap with velocity $\mathbf{u}$ and temperature $T_h = 273.15$ K, the number density n_{H_2O} increases within the domain. Moving toward the low-temperature boundary $\delta = 0$, where temperature T_c penetrates the initial frost layer, vapour molecules undergo a phase change at the phase change interface (PCI), defined by T_{PCI} and mass flux $\dot{m}_{PCI}$. Modelling this dynamic interface is critical as it governs ice growth over time. Consequently, detailed examination of this ice-vapour interface will be discussed further in the following section.
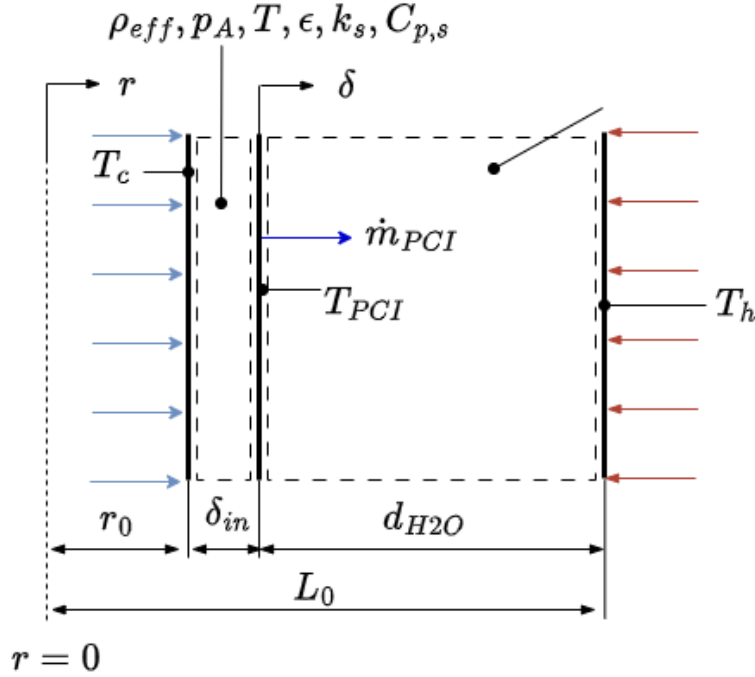
FIGURE 6.3: Mathematical 1D model of ice deposition on the phase change interface; symmetry line defined by $r = 0$; domain variables are within the dashed lines; dimension d_{H2O} is fixed and remains constant; *note*: schematic is not on scale.

6.1.2 Flow Regime

In reality, a free molecular flow defined by the Knudsen number beyond 10 enters the cold trap in fig. 6.2. If one assumes the 1D modelling in section 5.1.2 *Ice-Vapour Interface*, the system parameters n_{H2O}, p and T depend on each other and consequently on the inlet parameters. For clarification, the more water vapour per second entering the cold trap, the higher the amount of water molecules in the system. That means, below 1D model still holds, though the velocity field is not considered at this stage:

$$n_{H2O} = f(u, p, T), \tag{6.1}$$

where f is an arbitrary function. As in statistical mechanics, it is easier to write the pressure according to the number density of molecules:

$$p = \rho_{vap} \frac{R}{M} T = n_{H2O} k_B T, \tag{6.2}$$

where where p is the absolute pressure of the gas, n_{H2O} is the number density of the molecules given by the ratio $n_{H2O} = N/V$, T is the absolute temperature, and k_B is the Boltzmann constant relating temperature and energy, given by:

$$k_B = \frac{R}{N_A}, \tag{6.3}$$

where N_A is Avogadro's constant, the particle density per unit volume remains substantial even at ultra-low pressures like 10^{-12} hPa. Under standard conditions, this results in roughly 26500 molecules per cm^3 persisting in the environment. This underscores that even at extreme vacuum levels, describing the area as a complete void is impractical, as water vapour molecules are still present. Thus, under ultra-high vacuum, water vapour and other particles persist, highlighting that such systems cannot be considered devoid of material completely.

6.1.3 Ice-Vapour Interface

The Phase Change Interface (PCI) depends on several boundary conditions which are of great importance. In order to obtain deposition of ice, the temperature needs to be aligned with the pressure inside the water vapour domain at all times. Therefore assuming thermodynamic equilibrium at this interface, the deposition front temperature T_{PCI} is defined according to the Clausius-Clapeyron equation:

$$T_{PCI} = \frac{H_s/R}{\left(\frac{H_s}{RT_0} + \ln p_0\right) - \ln p} \tag{6.4}$$

Here H_s denotes the latent heat of water needed to obtain phase change, i.e. $H_s = 2834$ kJ/kg. Furthermore, the specific gas constant $R = 461.5$ J/kg $\cdot$ K for water vapour, T_0 and p_0 represent the reference temperature and pressure, respectively. In this case, the triple point of water is considered where $T_0 = 273.15$ K and $p_0 = 611.73$ Pa. Simultaneous heat and mass balances at the deposition interface lead to the phase change interface velocity of:

$$\left.\frac{\partial r}{\partial t}\right|_{r=\delta} = \frac{q_{f \to s}}{\rho_{eff} H_s}, \tag{6.5}$$

where $\partial/\partial t$ is the time derivative and $q_{f \to s}$ is the jump in the normal heat flux at the interface from fluid to solid:

$$q_{f \to s} = -k_f \nabla T_f + k_s \nabla T_s \tag{6.6}$$

Here the heat flux is only obtained by conduction, where k_f and k_s are the thermal conductivity of the solid, i.e. ice-frost, and fluid, i.e. water vapour, respectively. When there is still water vapour in the domain, hence $n_{H2O} > 0$, water vapour should be able to deposit on the interface. Therefore, the mass flux of the growing ice layer can be determined by;

$$\dot{m}_{PCI} = \rho_{eff} \cdot \left.\frac{\partial r}{\partial t}\right|_{r=\delta} = \rho_{eff} \cdot \frac{\partial \delta}{\partial t}, \tag{6.7}$$

The growth of new ice layers should be only stopped when there is no more water vapour to deposit, hence $n_{H2O} \to 0$. At this point, the increase in frost thickness is $\delta_{max} - \delta_{in}$.

$$\lim_{r \to \delta} \frac{\partial \delta}{\partial t} = 0 \tag{6.8}$$

That means the ice collection efficiency is a relation of:

$$\frac{\delta}{d_{H2O}} \tag{6.9}$$

As mentioned in Chapter 4, it is crucial for ice to deposit below 200 K to avoid the risk of methanol forming. Using the Clausius-Clapeyron equation (as referenced in 6.4), this implies that the pressure at the phase change interface (PCI) must remain below 0.12 Pa to ensure proper ice formation:

$$T_{\mathrm{PCI}} < 200\,\mathrm{K} \quad \text{and} \quad \lim_{r \to \delta} p < 0.12\,\mathrm{Pa}. \tag{6.10}$$

Furthermore, the initial pressure p_0 defines a temperature of 162.9 K, which corresponds to the initial conditions of the frost layer thickness δ_{in}. Therefore, to summarise:

$$T = 162.9\,\mathrm{K} \quad \text{at} \quad r = \delta_{\mathrm{in}} \quad \text{and} \quad t = 0. \tag{6.11}$$

6.1.4 Frost Density

The porosity of ice significantly influences the overall density of the ice frost. Specifically, the density of the frost at the interface with water vapour will differ from the density of the frost at the cold surface. This section explores two distinct approaches to understanding the structure of ice and its transient behaviour.

6.1.5   Inhomogeneous Frost Density

To implement the porosity of the ice frost, the porosity can be assumed to be an arbitrary function with respect to its temperature:

$$\epsilon = f(T) \quad \forall f \tag{6.12}$$

Since the water vapour number density n_{H2O} is not constant because it depends on the deposition rate, pressure and temperature in the system it is time-dependent. To obtain a relation between the number density and porosity, while still holding for the conservation of mass on the ice-vapour interface, the ice frost density can be described as a function of its thickness:

$$\rho_{eff} = (1 - \epsilon)\rho_{ice} + \epsilon \frac{n_{H2O} M}{N_A}, \tag{6.13}$$

where the particle density of ice, $\rho_{ice} = 916.7$ kg/m^3. The ratio $n_{H2O} M/N_A$ is equivalent to the density of the water vapour. *Note:* the boundary conditions δ_{in} and δ correspond with T_c and T_{PCI} since the effective (denoted as apparent) density of the frost layer depends on its porosity, i.e. fig. 6.4.

6.1.6   Homogeneous Frost Density

Given the assumption of homogeneous porosity throughout the frost layer, the variable porosity function in fig. 6.4 is no longer applicable, as it depicts an increasing porosity across the frost thickness. Modelling this frost layer as a porous structure remains accurate, even though fluid flow through it is not currently implemented in the model. Hence, one initially considers the permeability of water vapour through ice to be zero, with an adjustable porosity for ice set to zero as a preliminary parameter.

Darcy's Law, a fundamental description of flow behaviour in porous media, typically governs fluid movement through a material's porous structure. However, in free molecular flow applications, especially in high vacuum conditions, Darcy's Law does not directly apply. In high vacuum, the mean free path of gas molecules greatly exceeds the pore size, resulting in molecular-wall interactions rather than intermolecular collisions.

Darcy's Law will only become significant if the ice frost layer grows thick enough to create substantial temperature gradients between the cold finger and the phase change interface (PCI). When these gradients are large enough, they influence the vapour transport pathway within the frost, ensuring that water vapour is not directly deposited on the PCI. Thus, Darcy's law could eventually model flow dynamics in scenarios with thick frost layers and significant temperature gradients, modifying deposition within the porous frost layer. This approach allows for adaptable modelling that considers both initial and developed conditions in ice formation and vapour transport.

6.1.7   Delamination

In contrast to ice deposition, where the initial frost thickness is defined by δ_{in}, the initial thickness in this case should correspond to the water vapour. Thus, the mathematical model is adapted as shown in fig. 6.5, where the initial thickness of the water vapour is denoted by δ_{in}, and the interface moves in the positive r-direction. For clarity, another thickness, δ_{min}, is introduced to represent the minimum amount of ice that has sublimated. This is necessary because excess heat penetrates through the ice frost. If only δ_{in} sublimates, the water vapour interface moves exponentially, resulting in more sublimated ice than desired. There exists an optimal condition where the excess sublimation is minimised with respect to the initial thickness, such that:

$$\exists \, \delta_{in} \text{ such that } \delta_{min} = \min(\delta) \tag{6.14}$$
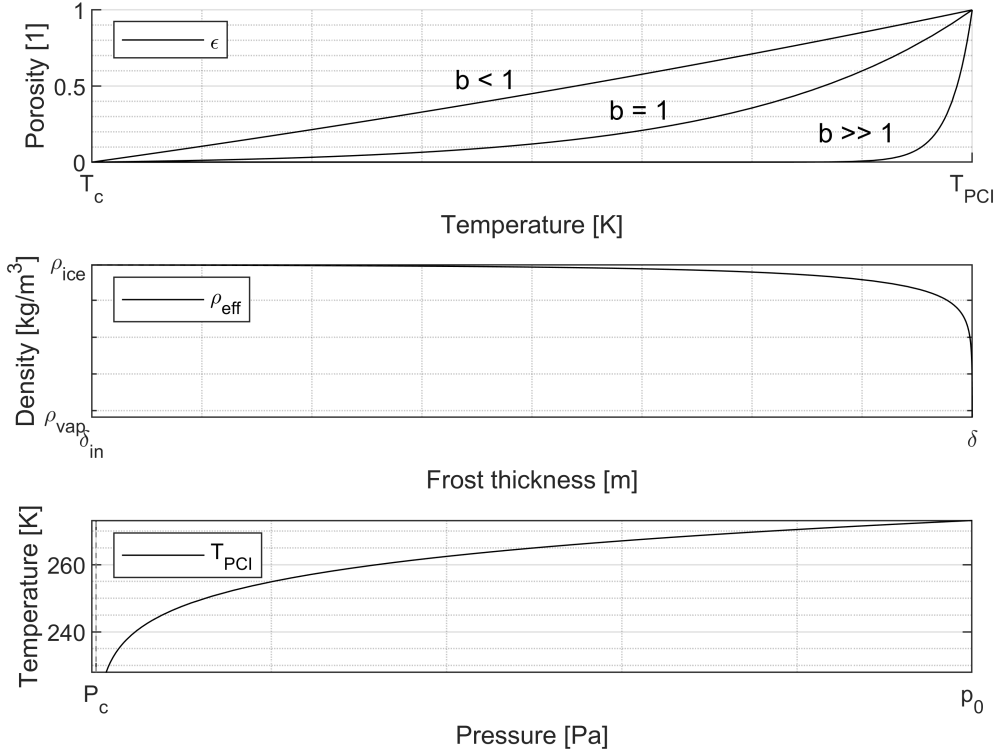
FIGURE 6.4: 1: Porosity of ice frost with respect to temperature in the interval T_c and T_{PCI} defined as $\epsilon = \frac{\exp b(T-Tc))-1}{\exp b(T_{PCI}-Tc))-1}$; coefficient b is a constant positive integer; 2: ice frost density as function of its thickness defined by eq. 6.13; the boundary conditions δ_{in} and δ correspond with temperature T_c and T_{PCI}, respectively; particle density of ice, $\rho_{ice} = 916.7$ kg/m^3; 3: the temperature of the phase change interface depending on vapour pressure according to eq. 6.4;

In this context, the initial frost thickness δ_{in} is assumed to be very small, but not zero. This assumption ensures that the model can effectively simulate the dynamics of the moving interface between the ice and the vapour, which would otherwise be difficult to capture if the thickness were set to zero. When considering delamination, the minimum power required for effective detachment of the ice layer from the cold finger, denoted as $\dot{q}_{del}$, must be calculated. The minimal delamination power can be expressed as:

$$\dot{q}_{del} = \left(k_s \theta_1 + k_f \theta_2\right)\frac{\partial T}{\delta_{min}}, \tag{6.15}$$

Here, s and f represent solid and fluid, respectively, where the fluid is water vapour and the solid defines ice. For delamination, it is essential that the remaining ice is not subjected to phase changes or large temperature gradients. The delamination of the ice from the cold finger occurs when the stresses at the ice-substrate interface exceed the adhesive strength of the interface. This balance involves thermal and mechanical stresses, primarily induced by temperature gradients and the mismatch in thermal expansion between the ice and the cold finger. Due to the complexity of these factors, a minimal ice thickness, δ_{min}, is sublimated. At this point, phase change occurs across the entire domain of this thickness.
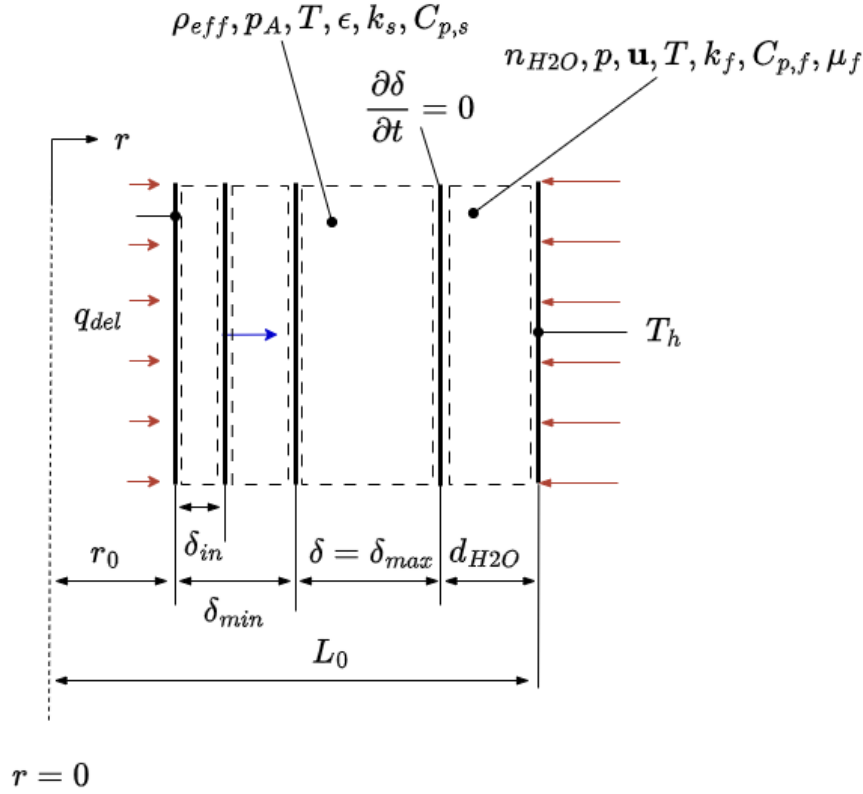
FIGURE 6.5: Mathematical 1D model of ice delaminating from the interface. Efficient delamination occurs when δ_{min} is minimised but sufficient to release the ice, with low temperature gradients remaining in the ice, i.e. $\delta_{max} - \delta_{min} \approx \delta_{max}$.

6.2 Coupled Flow

Given the interdependence of all subsystems and stages in the phase transition, evaluating the deposition process relative to the preceding sublimation stage is crucial.

6.2.1 Mathematical Approach

The conservation of mass, also known as the continuity equation, as derived in Appendix A (2), states that the rate of change in mass within a control volume inside the cold trap must hold, following equation 6.1:

$$\frac{\partial n_{\mathrm{H_2O}}}{\partial t} + \nabla \cdot (J_{\mathrm{H_2O}}) = 0, \tag{6.16}$$

where $J_{\mathrm{H_2O}}$ represents the molecular flux. This flux enters through the inlet of the cold trap, with the incident flux $J_{I,\mathrm{H_2O}}$ having been previously calculated in Section 5.5 and dependent on both the sublimation rate and rotational speed. Deposition at the phase change interface (PCI) may alter the mass balance, so the continuity equation must account for water vapour molecules inside the cold trap and the deposition rate, expressed as:

$$\frac{\partial n_{\mathrm{H_2O}}}{\partial t} + \nabla \cdot (J_{\mathrm{H_2O}}) = -\dot{m}_{\mathrm{PCI}} \tag{6.17}$$

The mass flux at the interface is determined using equation 6.7. It is important to note that the continuity equation provided only applies to continuum flow (i.e., when the Knudsen number is less than 1). In a 1D modelling scenario, this continuity equation can relate the deposition rate to the

sublimation rate (inlet molecular flux), as no flow field is incorporated. Another assumption is that only water vapour is considered as a phase, with interactions with other phases excluded from the analysis. Additionally, no sources other than $\dot{m}_{PCI}$ are accounted for within the control volume of the cold trap. However, an initial ice thickness, deposited at $t < 0$, is assumed, contributing to the initial number of molecules at $t = 0$. This initial ice layer represents a mass of $9.811 \cdot 10^{-2}$ grams, which is negligible for simplicity. Additionally, the initial molecule count is determined by the vacuum chamber pressure p_0, calculated as:

$$n_{\text{H}_2\text{O}} = \frac{p_0}{k_B T} \quad \text{for} \quad t = 0 \tag{6.18}$$

To maintain a steady-state solution, the deposition rate ideally matches the sublimation rate, avoiding batch processing. For example, with a heating power of 200 W and a rotation speed of 3 rpm, the peak sublimation rate is calculated at 185 grams per hour. To operate efficiently, the molecular flow over time should be regulated to align with this sublimation rate.

6.3 Results for Deposition

Water vapour enters the cold trap at $T_h = 273.15\,\text{K}$, flowing toward the cold fingers, with the empty circle at the centre representing the cold finger itself (see fig. 6.6). A steady-state solution is achieved under a defined temperature distribution. Specifically, at a pressure of $1 \cdot 10^{-4}\,\text{Pa}$, water vapour transitions into ice at $162.9\,\text{K}$, see eq. 6.4. To maintain equilibrium, the cold finger is cooled to $T_c = 150\,\text{K}$, resulting in the formation of approximately 52 grams of ice. While this may initially seem low, it is important to consider the graduation of the process and how it affects the overall phase transition. As ice forms and grows, the deposition must be analysed in terms of its time-dependent progression.

All ice is deposited below a temperature of 200 K, ensuring that no unwanted volatiles, such as methanol, are present. This temperature threshold is vital in preventing the formation of substances that could contaminate the final product of liquid water. To achieve a steady-state condition, a time-dependent study is conducted to analyse the deposition over time. Fig. 6.7 illustrates the deposition rate over time, showing a gradual increase in the total mass fraction of ice during nearly one hour of deposition. Initially, the deposition rate is notably high, exceeding 500 grams of ice per hour inside the cold trap. This rate might seem excessive at first. However, it is valid due to the specific initial conditions applied. The initiation of the deposition process relies heavily on the initial conditions used in the simulation. Since an initial ice thickness is introduced to obtain the movement of the interface, this thickness was previously water vapour within the domain. Consequently, the initial conditions are calculated based on δ_{in}, and an initial time is assumed for which this frost thickness is established. Further details regarding the accuracy of these conditions and their validation will be provided in subsequent sections. To elaborate on the results, consider the following key points:

- At $t = 2.7778 \cdot 10^{-4}\,\text{h} = 1\,\text{s}$, the deposition reaches its maximum gradient, exceeding 562 grams per hour. *Note*: This specific time frame corresponds precisely to the initial time parameter used for the initial conditions, explaining the extreme deposition rate observed at this moment. Following the first second, the rate decreases significantly until it stabilises at a later point.

- After 0.01 hours of deposition, the system reaches a critical threshold, at which point the decline in the deposition rate begins to slow. The rate starts to behave asymptotically, eventually approaching zero.

- Upon reaching the end of this asymptote, the deposition rate stabilises at a value of 33 grams per hour. The simulation is concluded after nearly one hour of deposition.

- The fraction of ice formed is evaluated concerning the amount present in the steady-state condition, meaning that after almost one hour of deposition, it attains its maximum amount. Although the deposition rate is not zero at this point, the total quantity of ice equals the steady-state solution.
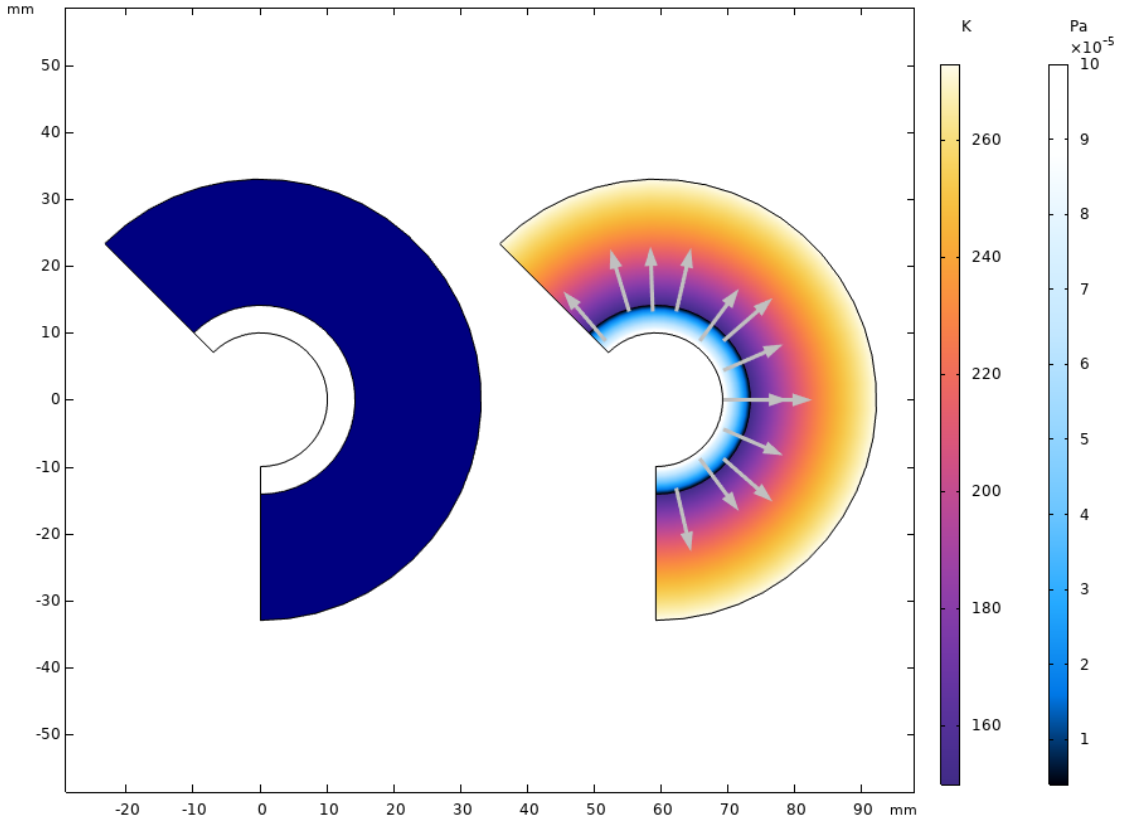
FIGURE 6.6: Steady-state solution illustrating the temperature field at equilibrium.

While results could have been obtained over a larger time scale, understanding the dynamics of ice formation toward equilibrium is crucial for optimising processes. The phase transition model, which considers ice deposition onto the cold fingers, needs to account for the subsequent delamination of the ice.

6.4 Results for Delamination

The initial stage of delamination involves the sublimation of water vapour upon contact with the cold surface of the cold finger. This phenomenon occurs as the temperature of the cold finger rises as a result of a heat flux applied at the same boundary. However, the formation of an ice layer continues as long as the temperature and vapour pressure, remain conducive to deposition. As the ice accumulates on the cold finger, the increasing weight of the ice layer generates stress at the interface between the ice and the cold finger substrate. This stress can eventually surpass the adhesive forces holding the ice in place, particularly when influenced by external perturbations, such as vibrations. However, prior investigations, such as those reported in Kalis [2024], have established that using vibrations alone is ineffective for ice detachment from the cold finger. The most effective approach to achieve delamination involves a external power source, at least for the LUWEX project. Upon initiating the sublimation of a small initial ice mass, denoted as δ_{in}, the heat required for overcoming the latent heat of sublimation facilitates a phase transition. Given that the initial thickness is considered negligible compared to the total ice thickness formed, δ_{max}, the time required to exceed the latent heat barrier is minimal, resulting in the penetrated heat facilitating further sublimation of additional ice. Consequently, the amount of delaminated ice increases proportionally. As δ_{in} increases, the additional sublimated thickness increases accordingly. In contrast, when δ_{in} decreases to a sufficiently low value, rapid heat transfer may lead to excessive sublimation, exceeding the initial desired amount. Specifically, ice sublimation begins at a temperature of 162.9 K under conditions of $p_0 = 1 \cdot 10^{-4}$ Pa.
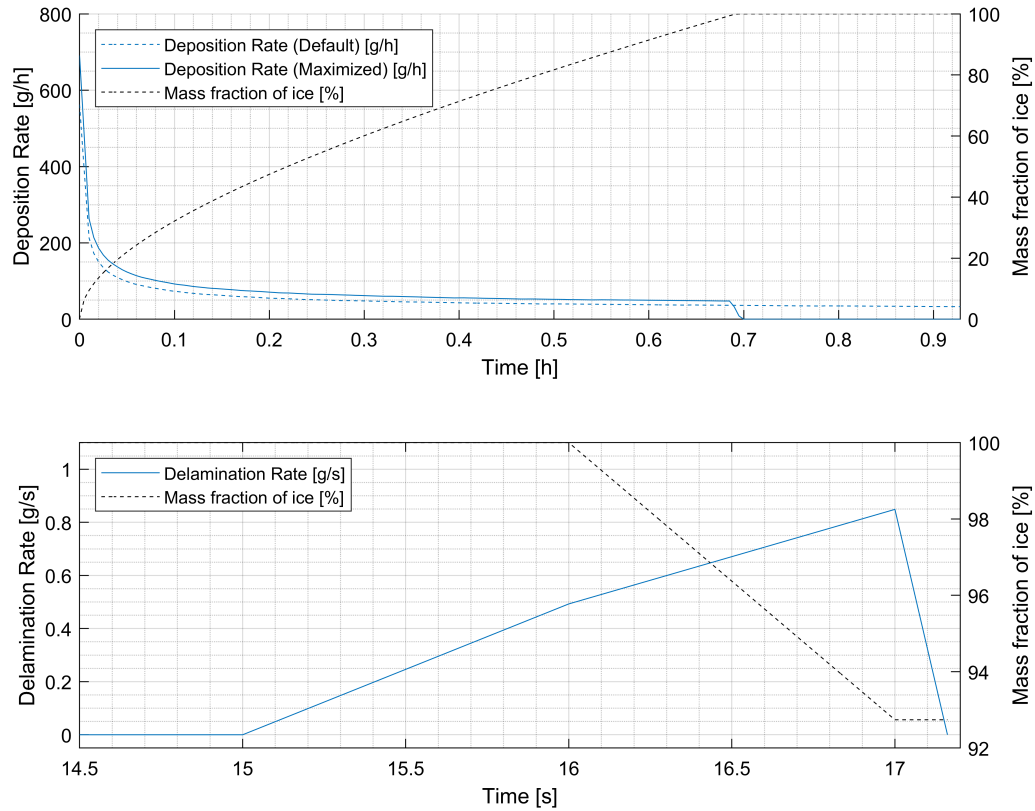
FIGURE 6.7: Deposition rate in grams per hour for $T_c = 150\,\mathrm{K}$ (Default), $T_h = 273\,\mathrm{K}$, and $\delta_{in} = 0.01\,\mathrm{mm}$ and $T_c = 140\,\mathrm{K}$ (Maximised); the delamination rate in grams per second indicates a total loss of ice of approximately 7.0% of the original deposited amount.

Again, this is evaluated using the Clausius-Clapeyron equation in 6.4. Thus, whenever the ice temperature exceeds this threshold, additional ice is sublimated. However, there exists an optimal value for δ_{in} that minimises the total sublimated thickness, known as δ_{min}. The results in Table 6.2 and fig. 6.7 summarises the relationship between the initial thickness of ice δ_{in}, the minimal sublimated thickness δ_{min}, and the time required for the delamination process:

- **Initial thickness** (δ_{in}): The values range from 0.01 mm to 1.0 mm, indicating the various initial conditions applied during the sublimation process.

- **Minimal thickness** (δ_{min}): The corresponding values of δ_{min} vary between 0.36 mm and 1.67 mm, which illustrates that as δ_{in} increases, δ_{min} also tends to increase. This relation indicates that a greater initial thickness contributes to a higher volume of ice being effectively delaminated.

- The time required for the sublimation process varies from 17 seconds to 23 seconds, with longer times associated with larger values of δ_{in}. This suggests that larger initial thicknesses require more time to overcome the latent heat of sublimation, which aligns with the understanding that greater energy input is necessary for thicker ice layers.

- For the minimum value of $\delta_{min} \approx 0.1\,\mathrm{mm}$, the total delaminated fraction of ice exceeds 7%. This implies that 93% of the initially deposited ice, denoted as δ_{max}, proceeds to the liquefaction chamber for further processing.

δ_{in} [mm]	δ_{min} [mm]	Time [s]
0.01	0.39	17
0.1	0.36	17
0.4	0.81	19
0.5	1.21	20
1.0	1.67	23

TABLE 6.2: Input parameters and results for delaminating the ice frost of thickness δ_{max}.

Consequently, the inability to fully detach the ice indicates that optimisation of the initial conditions and operational parameters is crucial for enhancing the efficiency of the delamination and subsequent liquefaction stages.

6.5   Optimisation & Validation

To optimize the conditions for ice growth, two primary approaches can be taken. The first focuses on maximising the total mass of deposited ice, while the second targets the maximisation of the mass flux, effectively optimising the rate of phase change over time. These strategies can be mathematically expressed as follows. The first approach involves ensuring that the rate of change of the ice thickness approaches zero at the interface as deposition stabilises. This means that no further increase in ice thickness occurs, and the ice reaches its maximum thickness:

$$\lim_{r \to \delta} \frac{\partial \delta}{\partial t} = 0 \quad \to \quad \delta = \delta_{\max} \tag{6.19}$$

Since the inlet temperature of water vapour should remain constant at 273.15 K, the temperature T_h cannot be varied, nor can the pressure inside the TVAC. Therefore, the only control variable to maximise the ice mass is the cooling temperature T_c. For the steady-state solution depicted in fig. 6.6, it is found that $\delta = \delta_{\max} = 4.16$ mm at a cooling temperature of $T_c = 148$ K. This results in a minimal increase of less than 1% in the ice mass. Consequently, optimising for equilibrium mass is not deemed worthwhile.

The second approach aims to maximise the rate of ice growth, corresponding to maximising the phase change velocity at the phase change interface:

$$\max \left(\frac{\partial r}{\partial t} \Big|_{r=\delta} \right) \tag{6.20}$$

In this scenario, the goal is to accelerate the phase change process, which will increase the mass flux $\dot{m}_{PCI}$. According to equation 6.5, this can be achieved by maximising the temperature gradient between the ice and the water vapour at the interface. As such, T_c is reduced to its lower limit, which is equivalent to the ambient temperature, $T_c = T_0 = 140$ K. Fig. 6.7 illustrates the impact of changing the cooling temperature. The maximum deposition rate can be evaluated as follows:

- The deposition rate reaches its maximum gradient after a few seconds, exceeding 691 grams per hour.

- After 0.01 hours of deposition, the system reaches a critical threshold, after which the deposition rate begins to slow.

- Upon reaching the asymptote, the deposition rate stabilises at a value of 50 grams per hour before reaching zero.

- Unlike the default deposition process, the asymptote does approach zero and after 0.7 hours.

Overall, while both approaches, maximising total deposited ice mass and optimising mass flux, are valid, prioritising the acceleration of the phase change process by maximising mass flux offers the most substantial benefits for optimising ice growth. This is especially important when considering time-dependent deposition, as it helps quantify the production process in either a batch or continuous mode.

6.5.1 Model Validation

The transient study conducted suggests that the phase change is mainly dependent on temperature gradients between the ice and water vapour domains. However, the resulting behaviour, where the ice thickness δ approaches the maximum reference length of the water vapour domain L_0, raises concerns, as this seems physically unrealistic and inconsistent with the expected behaviour of the deposition process. The issue likely stems from the conservation of mass, which should hold throughout the deposition process as outlined in eq. 6.17. If the phase change is incorrectly modelled, it could be due to initial conditions, particularly at times $t < 0$ and $t = 0$.

It is possible that the deposition process is less sensitive to variations in the molecular inlet flux, as the phase change may be primarily limited by pressure conditions. In such cases, changes in the number density of water molecules due to sublimation (in Stage I) might not significantly impact the deposition process itself. This could explain the observed discrepancy in the transient study.

To address this issue, it would be useful to reconsider the initial conditions for both the ice and vapour domains, ensuring that the mass conservation equation is correctly applied and that the impact of pressure variations is fully accounted for. This may be more pertinent for 2D and 3D models, where molecular flux fluctuations inside the cold trap are more pronounced. Modelling the ice deposition in two dimensions would likely be more straightforward, as a velocity field can be incorporated, unlike in 1D models, where only potential flow can be obtained. As Schrödinger stated, "there is nothing physical about a potential flow". Moreover, further investigation into the molecular fluxes and their effects on deposition, especially under transient conditions, may help explain the deviations from the expected behaviour in the system.

7 | Stage III: Liquefaction

After the ice is deposited and delaminated in the previous stage, it will be subjected to gravitational force, causing it to fall into the liquefaction chamber. The liquefaction process begins once the ice reaches the chamber. At this point, the ice must undergo a phase change from solid to liquid, which is the final stage (Stage III) in the process.
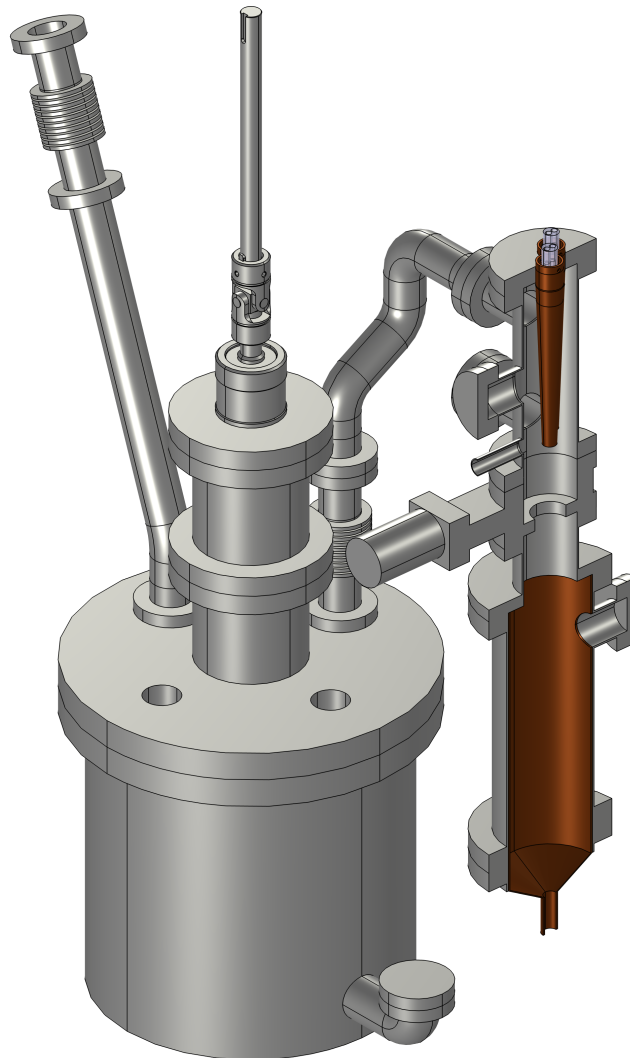
FIGURE 7.1: Cross-section of the capturing system connected by the slider to the liquefaction chamber; inner geometry is made of copper for optimal heat transfer towards the ice.

7.1 Methodology

As mentioned, ice reaches the liquefaction stage primarily due to gravitational forces, allowing it to settle in the chamber. In Fig. 7.2, the working principle of the liquefaction process is illustrated. The sliding gate mechanism plays a crucial role in ensuring that the liquefaction chamber is completely isolated from the previous stage, which is involved in capturing water vapour. This isolation prevents any residual water vapour from flowing into the liquefaction chamber or vice versa, maintaining the integrity of the phase change process.

The *slider* (UHV sliding gate) closes before the pressure inside the *liquefaction chamber* increases to ensure phase change from solid to liquid

Heat is needed to prevent liquid water reaching its saturation point

Stage III: Liquefaction of ice

Pressure field on the boundary

Radiative heat flux by heating elements attached to the copper interior ensures phase transition

External housing made of stainless steel with an inner geometry of copper to enhance phase change

Liquid water flows through the *water outlet tube* to the storage system

FIGURE 7.2: Working principle of liquefying water ice; *note* that the storage system is not considered at this stage

The first step in the liquefaction process is to increase the pressure inside the chamber. It is essential to raise the pressure to a level significantly higher than the triple point of water. The triple point is the unique set of temperature and pressure, where water can exist simultaneously in its solid, liquid, and gas phases. This point occurs at a temperature of 273.15 K and a pressure of 0.6117 kPa. Operating the liquefaction process at a pressure well above this threshold ensures that the system avoids any transitions back to the gas phase, maintaining control over the liquefaction process. For this setup, the operating pressure is set around 1-50 kPa, ensuring stable conditions for the phase transition.

Once the pressure reaches the required levels, the temperature inside the chamber is increased through electrical heating. Heating elements or coils are strategically positioned around the inner copper tube, delivering electric power to generate the necessary thermal energy. This electric power radiates heat towards the ice. The copper tube serves as an efficient medium for heat conduction, ensuring uniform heating throughout the chamber. As the temperature gradually increases, heat is absorbed by the ice, and the phase transition from solid to liquid begins.

The radiative heat transfer from the copper inlay to the ice follows the principles outlined in the Stefan-Boltzmann law. This heat is essential to overcoming the latent heat of fusion, which is the energy required for the ice to change its phase from solid to liquid without an increase in temperature. The applied heat flux at the water-ice boundary, denoted by q_{int}, plays an important role in the phase transition process. This specific heat flux governs the rate of energy transfer necessary for converting ice into water at the interface.

In fig. 7.2, the radiative heat flux incident on the ice is depicted. One might question why heat conduction is not considered in this context. The rationale behind this choice lies in the specific configuration of the ice relative to the copper inlay. In this setup, the ice only makes contact with the copper at the interface. Given that the liquefaction process is modelled in one dimension, including conduction would necessitate assuming uniform heat conduction across the entire surface area of the ice. This assumption is unlikely to hold in practice. Additionally, during the liquefaction process, the ice may fracture, which would further reduce the effective interaction area between the ice and the copper along the circumference. In contrast, the 1D model exclusively represents the ice phase, excluding the copper inlay and the surrounding vacuum from the simulation. As a result, any heat boundary condition can be applied or iterated solely at the ice boundaries, without considering the thermal interactions with the copper or the vacuum. Concluding, only radiative heat flux is considered for this 1D model, at this stage. Furthermore, the goal of the model is not to investigate the detailed process of liquefaction itself, but rather to determine the time required to heat the ice to its melting point. *Note:* the current emphasis is not on the exact numerical values of q_{int} or other system parameters but on understanding the interconnections between all stages of the process.

Additionally, detailed verification of all phase transitions and related processes will be conducted later in the section titled *Validation & Analysis*. This reduces the criticality of the initial system parameter values, as these will ultimately be assessed and calibrated during the validation phase.

Unlike sublimation, where a higher amount of energy is required to convert solid ice directly into vapour, liquefaction requires less energy due to the relatively lower latent heat of fusion. As the ice absorbs heat, it melts and is converted into liquid water. The liquid water then flows downward, driven by gravity, and is collected for further storage. The system is designed to ensure that the heating elements operate efficiently without exceeding the temperature limit of 60°C, which prevents the components from overheating and damaging the system.

7.1.1 Mathematical Model

The ice thickness, denoted by δ, now differs from previous models due to the delamination of the frost. In this case, the frost thickness is given by $\delta = \delta_{\max} - \delta_{\min}$, where $\delta_{\max}$ is the frost thickness deposited on the cold finger, and $\delta_{\min}$ represents the delaminated thickness. The properties of the ice remain unchanged throughout this process. During the phase transition from ice to water, the material undergoes volumetric compression due to changes in density. These changes are captured in the material coordinate system, assuming the ice initially fills the entire domain. The model assumes no mixing in the liquid phase, which allows for the use of the conduction (adapted from eq. 3 in appendix A) equation in material coordinates, simplifying the model by removing the need to compute velocity fields resulting from density changes during the phase change:

$$\rho C_p \left(\frac{\partial T}{\partial t} \right) = k \nabla^2 T + Q \tag{7.1}$$

Here ρ is the apparent density, C_p is the apparent heat capacity, k the apparent thermal conductivity and Q defines a heat source depending on q_{int} or similar applied boundary condition such as T_{max}. The values in table 7.1 are measured in spatial coordinates. To adapt them to the material coordinates, they must be adjusted using the ratio of densities.

Variable	Discription	Default value	Unit
q_{ext}	Radiative heat flux emitted from the liquefaction chamber	11.5	W/m^2
q_{int}	Radiative heat flux incident to the boundary of ice	80.0	W/m^2
ϵ	Porosity	0	1
k_s	Thermal conductivity of solid ice	$k_i(T)$	W/m/K
k_f	Thermal conductivity of **liquid** water (fluid)	0.613	W/m/K
$C_{p,s}$	Heat capacity of solid ice	$C_{pi}(T)$	J/kg/K
$C_{p,f}$	Heat capacity of **liquid** water (fluid)	4179	J/kg/K
$C_{p,Cu}$	Heat capacity of copper	385	J/kg/K
k_{Cu}	Thermal conductivity of copper	400	W/m/K
ε_{Cu}	Surface emissivity of copper	0.1	1
$\mathcal{F}_{ext \rightarrow int}$	View factor for liquefaction inner copper chamber towards ice	0.10581	1
T_0	Initial / Ambient temperature	140	K
T_{max}	Maximum temperature for control	333.15	K
ΔT	Transition interval for temperature	1	K
T_{pc}	Phase transition temperature	273.15	K
r_0	Effective radius of cold finger	10	mm
L_0	Maximum reference length of fluid domain	10	mm
p_0	Pressure inside vacuum chamber	1e-4	Pa
H_l	Latent heat of fusion	334	kJ/kg

TABLE 7.1: System parameters and variables for stage III; liquefaction of ice.

In the 1D model, this is achieved by multiplying by the density ratio:

$$\rho_\zeta = \frac{\rho_i}{\rho_{\text{water}}}, \tag{7.2}$$

where $\rho_i = 916.7$ kg/m^3 is the density of ice, and $\rho_{\text{water}} = 997$ kg/m^3 is the density of water. Using this transformation, the density of water in material coordinates is given by:

$$\rho_2 = \rho_{\text{water}} \cdot \rho_\zeta = \rho_i. \tag{7.3}$$

This approach is consistent with the principle of mass conservation because the integral of density $\rho = \rho_2$ over the geometry of the domain remains constant over time. The material properties also adjust accordingly:

$$k_f = k_f \cdot \rho_\zeta, \tag{7.4}$$

and

$$\rho_1 = \rho_{\text{water}} \cdot \rho_\zeta. \tag{7.5}$$

The heat flux from the elements is defined as q_{ext}, which is emitted from the copper surface after reaching the interior surface of the ice, with magnitude q_{int}. The distance from the center of the liquefaction chamber to the exterior surface is denoted by L_0. The model assumes axis-symmetry with respect to the radius r, where symmetry is applied at $r = 0$. In terms of radiation, the distance d is critical, as it affects the amount of radiation reaching the ice. Despite this, the dimensions of the copper cold finger are still relevant in the model, as the ice deposits on its outer surface. The system variables within the liquefaction chamber include pressure and temperature. The view factor, denoted as $\mathcal{F}$, will be discussed in more detail later.

7.1.2 Phase Change

The liquefaction process involves the transition of solid ice to liquid water. This transition can be modelled similarly to the sublimation process outlined in section 5.1.5. Consequently, the equations from 5.6 to 5.8, including the Heaviside function depicted in Fig. 5.3, are applicable with modifications to reflect the parameters specific to liquefaction.
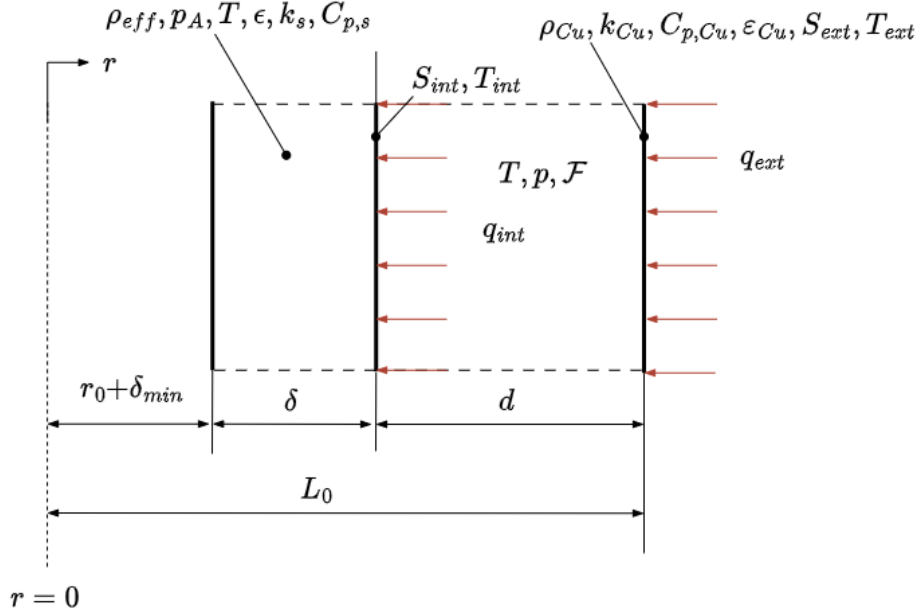
FIGURE 7.3: Mathematical 1D model of liquefying ice; note that the ice frost thickness δ is defined as the maximum frost thickness minus the delaminated frost thickness, i.e., $\delta = \delta_{\mathrm{max}} - \delta_{\mathrm{min}}$.

A summary of these adjusted parameters is provided in table 7.1. The apparent density, ρ, is a function of the densities of water-ice (ρ_1) and liquid water (ρ_2) in their respective phases, expressed as:

$$\rho = \rho_1 \theta_1 + \rho_2 \theta_2, \tag{7.6}$$

where ρ_1 is the density of phase one (ice), and ρ_2 represents the density of phase two (liquid water). The phase indicators, θ_1 and θ_2, correspond to ice and liquid water, respectively, with the constraint that $\theta_1 + \theta_2 = 1$. The mass fraction, $\alpha_{1\to2}$, representing the transition from phase one to phase two, is defined as:

$$\alpha_{1\to2} = \frac{\rho_2 \theta_2 - \rho_1 \theta_1}{\rho}. \tag{7.7}$$

Latent heat is incorporated into the apparent heat capacity, C_p, which is given by:

$$C_p = \frac{1}{\rho}\left(\rho_1 \theta_1 C_{p,1} + \rho_2 \theta_2 C_{p,2}\right) + H_s \frac{d\alpha_{1\to2}}{dT}, \tag{7.8}$$

where $C_{p,1}$ and $C_{p,2}$ are the specific heat capacities of each phase. The latent heat of the phase transition is denoted as H_l, corresponding to the fusion enthalpy. The most significant difference between sublimation and liquefaction lies in the latent heat required for the phase change. For liquefaction, $H_l = 334\,\mathrm{kJ/kg}$, which is substantially lower than the latent heat for sublimation. This reduced latent heat decreases the energy required for the phase change, impacting both the time and rate of the process.

Furthermore, $\frac{d\alpha_{1\to2}}{dT}$ represents the rate of change of the mass fraction with respect to temperature. The apparent thermal conductivity, k, during the phase transition is given by:

$$k = k_1 \theta_1 + k_2 \theta_2, \tag{7.9}$$

where $k_1 = k_s$ and $k_2 = k_f$ are the thermal conductivities of phase one (ice) and phase two (liquid water), respectively, as detailed in Table 7.1. This setup enables accurate simulation of the phase-change process, analogous to the sublimation process described in Chapter 5.

7.1.3 Temperature Control

Heating in the liquefaction process must not exceed a temperature of 60°C, or 333.15 K, to prevent damage and ensure safe operation of the heating cables. This temperature limit is crucial for maintaining the performance of the elements and avoiding burnout. In phase change processes, even small deviations from the set temperature can result in undesirable changes in the phase transition dynamics. Mathematically, this temperature constraint can be expressed as:

$$\lim_{T \to T_{\max}} q_{\text{ext}} = 0, \tag{7.10}$$

where T is the temperature at the boundary located at $r = L_0$, and $T_{\max} = 333.15\,\text{K}$. This condition implies that as the temperature at the specified boundary approaches the maximum temperature limit, the external heat flux q_{ext} approaches zero. In practical terms, when the temperature reaches $T_{\max}$, the radiative heat flux can be evaluated by substituting $T_{\max}$ into the temperature equation, ensuring the system does not exceed the allowable thermal limits.

7.1.4 Surface-to-Surface Radiation

In a thermal system like the liquefaction chamber, radiative heat flux plays a central role in driving phase transitions, particularly when solid ice is converted to liquid under controlled heating. The radiative heat flux, which depends on the chamber's interior temperature and properties like surface emissivity, is governed by the Stefan-Boltzmann law. This law links the power emitted by a surface to its temperature, adjusted by the surface emissivity, which accounts for the material's ability to emit radiation relative to an ideal blackbody. Thus, for accurate modelling, both the maximum temperature reached in the chamber and the emissive properties of materials (such as copper in this case) must be considered to determine the radiative heat flux impacting the ice.

The net radiative heat flux, $q_{r,net}$, represents the effective radiative energy exchange that contributes to the heating of the ice and thus promotes liquefaction. It is calculated by considering both the radiative flux incident on a surface and the thermal radiation emitted by that surface at a given temperature T. This flux can be expressed as:

$$q_{r,net} = \varepsilon \big(G - e_b(T) \big) \tag{7.11}$$

where ε is the emissivity of the surface material, indicating the fraction of radiation the surface emits relative to an ideal blackbody, G is the total incident or irradiation flux on the surface:

$$G = G_{amb} + G_{ext} + G_m, \tag{7.12}$$

encompassing contributions from surrounding heated elements and the chamber walls, $e_b(T)$ is the blackbody emissive power, which describes the theoretical maximum radiation emitted by the surface at temperature T. In this expression, G incorporates radiative flux from various sources, such as ambient irradiation (from heated chamber walls $\to$ copper inlay), external irradiation (from any additional direct heat sources), and mutual surface irradiation (accounting for radiation exchange between surfaces within the chamber). These components combined create the incident flux G that reaches the ice surface, enhancing the heat transfer necessary for liquefaction.

The blackbody emissive power, $e_b(T)$, is a temperature-dependent term that can be modified by the refractive index n when dealing with media other than a vacuum. The blackbody emissive power is given by:

$$e_b(T) = n^2 \sigma T^4 \tag{7.13}$$

Here σ is the Stefan-Boltzmann constant, representing the fundamental constant of proportionality in radiative heat transfer, n is the refractive index, and T is the surface temperature. In media with refractive indices greater than 1, the term n^2 adjusts $e_b(T)$ to reflect how the medium influences the radiation behaviour. This adjustment is crucial in transparent media, where the refractive index slows down light propagation compared to a vacuum, and impacts how energy is

absorbed, transmitted, or emitted within the chamber. For instance, in an environment with higher refractive indices, the net radiative exchange is more complex as light interacts differently with these materials, further affecting the heat flux absorbed by the ice. In the liquefaction chamber, understanding $q_{r,net}$ is vital for determining the precise amount of energy transferred to the ice.

7.1.5 View Factor

In the liquefaction process, radiation is exchanged between the interior surface of the chamber, S_{ext}, and the outer surface of the ice, S_{int}, through surface-to-surface radiation. The view factor, denoted as $\mathcal{F} = \mathcal{F}_{ext \to int}$, is crucial for determining how much radiative energy leaving S_{ext} reaches S_{int}. The view factor depends on the geometry, orientation, and distance between the two surfaces. For simple geometries, view factors can often be calculated analytically. However, in the case of the irregular geometries found in the liquefaction chamber, it is impractical to determine the view factor analytically. Instead, an arbitrary view factor $\mathcal{F}_{ext \to int}$ is defined as the ratio of the radiation leaving surface S_{ext} that intercepts surface S_{int}:

$$\mathcal{F}_{ext \to int} = \frac{\text{Radiation leaving } S_{ext} \text{ and intercepting } S_{int}}{\text{Total radiation leaving } S_{ext}} \tag{7.14}$$

This value depends primarily on the geometric configuration of the system. However, in this case, the radiation leaving S_{ext} is used to liquefy the ice, meaning that the view factor $\mathcal{F}$ must be calculated based on the heat transfer in solids and surface-to-surface radiation, as described in Appendix B, specifically Section B.3 | *1D Liquefaction Model*. In summary, the view factor computation is performed at each evaluation point on the boundaries. A boundary has an upside and a downside and both can be exposed to radiation. In this model the liquefaction chamber radiates inward and the ice radiates outward. The mutual surface irradiation is evaluated based on an upside and a downside. Both are available on all boundaries where surface-to-surface features are active. To compute the geometrical view factor, for example, $\mathcal{F}_{ext \to int}$, the following integration needs to be defined:

$$\mathcal{F}_{ext \to int} = \frac{\int_{S_{int}} \mathcal{I}(ext, 0) dS}{A_{ext}} \tag{7.15}$$

where S_{int} and S_{ext} denote interior and exterior surfaces, A_{int} and A_{ext} are corresponding surface areas. The integration at the numerator is defined over the ice cone, which radiates only on the upside of its surface.

7.2 Radiative Heat Flux

The radiative heat energy, or radiosity, reaching the ice surface is a key factor to initiate phase change. This radiative heat transfer, represented by the net radiative heat flux $q_{r,net}$, depends on the temperatures and radiative properties of both the chamber walls and the ice surface. If all the radiative energy emitted by the chamber walls is absorbed by the ice, then the net radiative flux should ideally be zero, indicating a balanced energy exchange. Mathematically, this condition is represented by:

$$q_{r,net} = \varepsilon \big(G - e_b(T) \big) = q_{int} + q_{ext} = 0$$

where ε is the emissivity of the copper surface inside the chamber, G is the radiosity reaching the ice from the chamber walls, $e_b(T)$ is the blackbody emissive power of the ice surface at temperature T, q_{int} and q_{ext} are the internal and external components of radiative heat flux, respectively. Since the initial ice temperature is assumed to be equivalent to the ambient temperature, no significant radiosity occurs at the start, as the ice is in thermal equilibrium with its surroundings. This condition simplifies the initial energy balance, allowing the equation to be rewritten to represent the initial conditions more effectively as follows:

$$\varepsilon q_{ext} = n^2 \sigma \big(T_{ext}^4 - \varepsilon \mathcal{F}_{ext \to int} T_{ext \to int}^4 \big)$$

In this modified equation, n represents the refractive index of the medium, T_{ext} is the temperature on the exterior surface, $T_{ext \to int}$ is the temperature from the external chamber environment towards the interior, $\mathcal{F}_{ext \to int}$ is the view factor, representing the fraction of radiation that reaches the ice from the chamber walls. As a system variable, the temperature $T_{ext \to int}$ influences the energy exchange rate. Therefore further simplifying above equation into a final equation that isolates the effective external radiative flux reaching the ice surface:

$$\varepsilon q_{ext} = n^2 \sigma \left(T_{ext}^4 - \varepsilon \mathcal{F}_{ext \to int} T^4 \right)$$

This final expression highlights how the temperature gradient, material emissivity, and spatial orientation (view factor) together define the actual heat flux absorbed by the ice. The effective radiative heat flux at the ice surface, q_{int}, and the external radiative flux, q_{ext}, can now be calculated. This equation ensures that the radiative heat flux reaching the ice is correctly adjusted for the view factor, capturing the portion of radiation transferred from the chamber surfaces to the ice. .

7.3   Liquefaction

Before the heating elements are activated, the initial temperature of the ice is assumed to match the ambient temperature of the thermal vacuum chamber (TVAC), which is 140 K. Any temperature gradients within the ice caused by delamination are considered negligible once the ice has disintegrated in the liquefaction chamber. This assumption is valid because the slider is activated after the delamination process, allowing sufficient time for the ice temperature to equilibrate with the ambient environment, thereby minimising any significant temperature differences.

The temperature at which ice transitions into liquid water, commonly known as the melting point, is 273.15 K. This value remains constant over a wide range of pressures. Only at pressures exceeding 10 MPa does the melting point begin to deviate from this standard value. Since the operating pressure in this scenario is well below 10 MPa, the melting point is consistently set at 273.15 K. The substantial temperature difference between 273.15 K (the melting point) and 140 K (the initial ice temperature) results in a significant time delay before the ice begins to melt. As illustrated in Fig. 7.4, when the emissivity factor, $\varepsilon \mathcal{F} \approx 100$, and the emissivity of copper is set to 1, it takes 1820 seconds to raise the temperature of the ice to the melting point of 273.15 K. For clarity, the X-axis in the figure is scaled in intervals of 200 seconds. The results of the liquefaction process under different emissivity conditions are as follows.

- For $\varepsilon \mathcal{F} \approx 100$: The total time for the liquefaction process, including the heating period up to the melting point, is 1850 seconds. The phase transition itself takes only 40 seconds, during which the liquefaction rate exceeds 4 grams per second.

- For $\varepsilon \mathcal{F} \approx 50$: The time required to heat the ice to the melting point nearly doubles, and the liquefaction rate does not exceed 2.5 grams per second. The entire mass of ice liquefies after 3585 seconds, or nearly one hour.

- For $\varepsilon \mathcal{F} \approx 10$ where $\varepsilon = 0.1$ (the emissivity of copper): The heating period extends significantly, taking 17700 seconds to raise the ice to the melting point before initiating the phase change. Once the phase transition begins, the liquefaction process takes only 200 seconds, with the rate reaching 0.5 grams per second.

This data underscores the impact of emissivity and heat transfer efficiency on the liquefaction rate and overall process duration. Lower emissivity values greatly prolong the heating phase, even though the phase transition itself remains relatively brief.

7.4   Model Validation

While the existing 1D model provides a reasonable approximation of the liquefaction process, it simplifies several physical phenomena that could be better represented in more sophisticated

models. For instance, the current model primarily assumes a simplified heat transfer mechanism, focusing on basic heat flux calculations without fully incorporating the complexities of radiation exchanges between surfaces during the liquefaction process. By using surface-to-surface radiation in a more comprehensive model, one could better account for the radiative energy transfer between the ice and its surroundings, which becomes particularly relevant in 3D simulations where spatial variations in radiation are more pronounced. In such models, the effect of radiation fluctuations within the liquefaction chamber, such as redistributed heat or absorbed by different surfaces, could influence the phase transition rate, leading to a more accurate prediction of the liquefaction dynamics.

Additionally, 3D models could account for the varying geometries and boundary conditions of the system, further enhancing the precision of the phase change simulations. Since the radiative heat fluxes and view factors depend on the relative orientations of surfaces in space, a 3D model would provide a more realistic assessment of how heat is transferred in the system as a whole, including the effects of angles and surface areas involved in the radiation exchanges. While the 1D model effectively provides an initial relationship between the applied thermal conditions and the liquefaction process, incorporating more comprehensive 3D models offers a better insight into the liquefaction dynamics, particularly with regard to the transient behaviour of radiation.
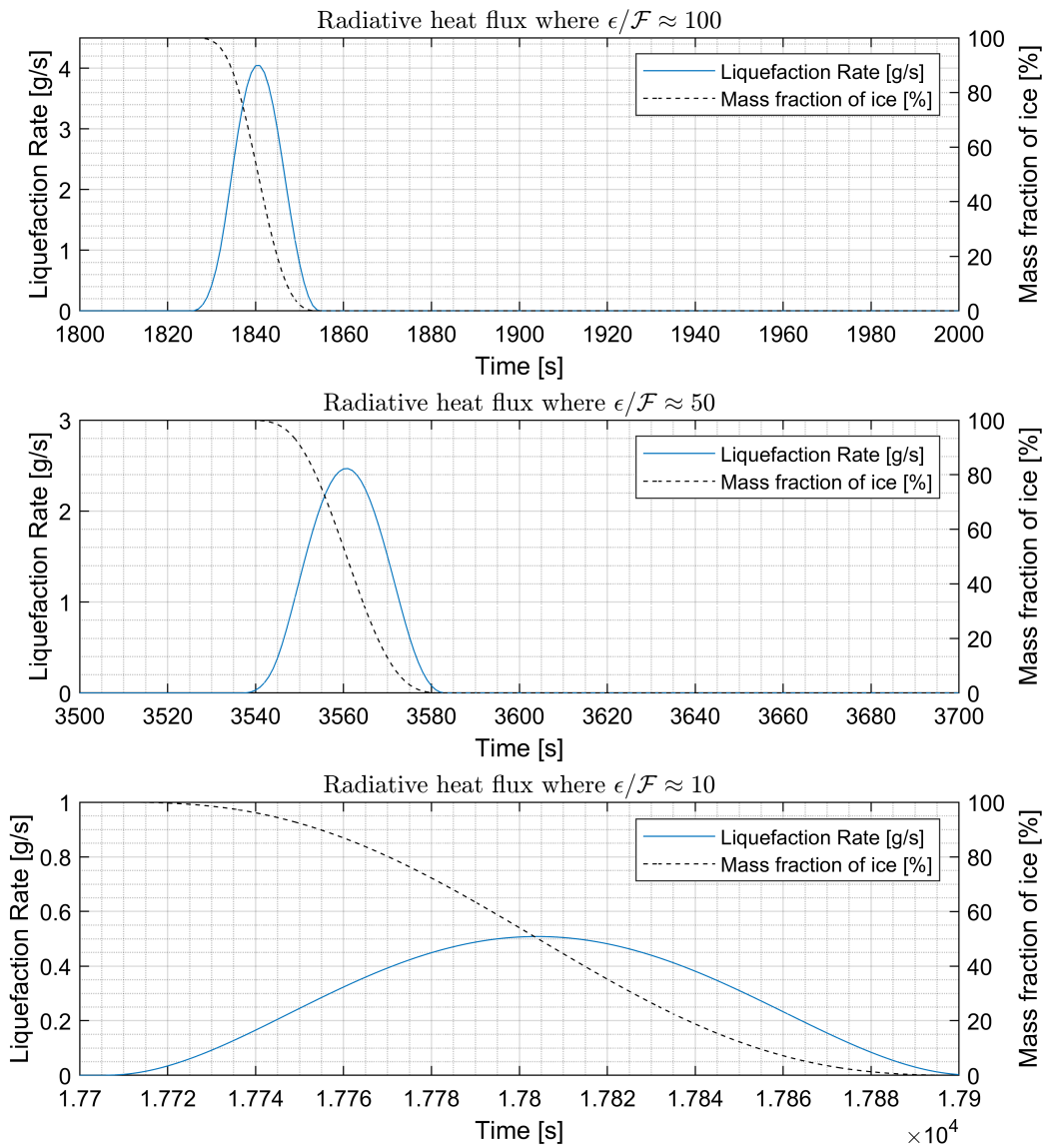
FIGURE 7.4: Liquefaction rates at various values of $\varepsilon\mathcal{F}$, illustrating the minimal time required for phase transition relative to the time needed to heat the ice.

8 | Validation and Analysis

The validation of models and experiments is a critical step in scientific research, particularly in fields where theoretical predictions must be tested against empirical observations. Validation ensures that the models accurately represent the physical processes being studied and that experimental results are reliable. In the context of Lunar water extraction and related phase transition processes, robust validation is essential to ensure that both computational models in this study and experimental setups yield consistent results that can inform future missions and technologies.
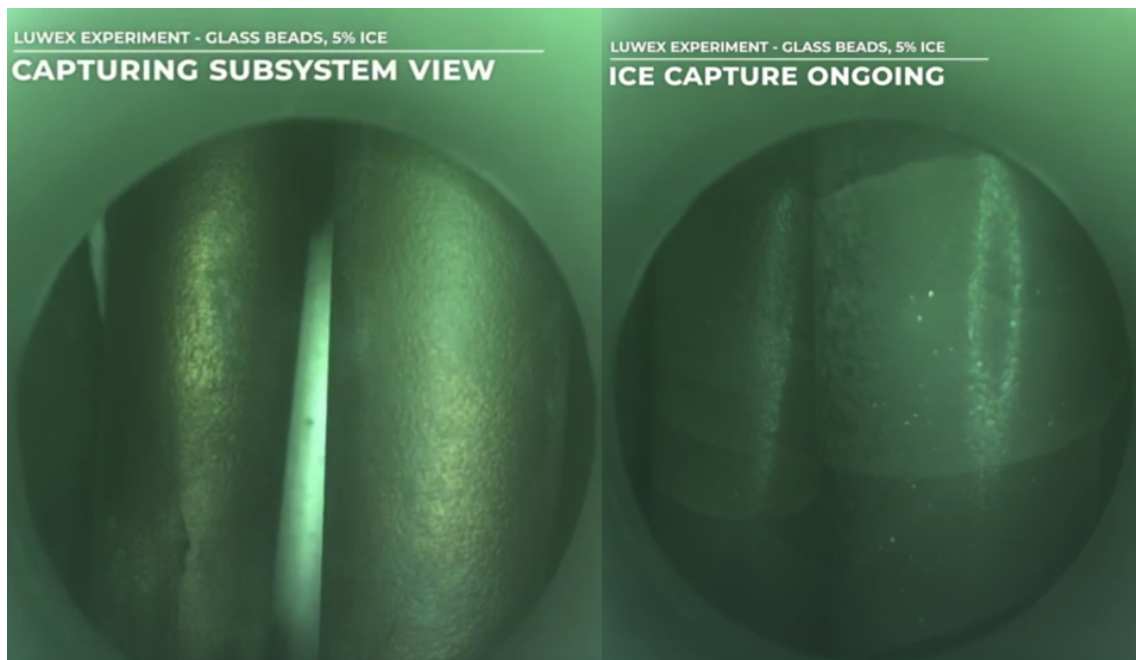
FIGURE 8.1: Left image: The cold trap setup from the LUWEX experiment, featuring two cold fingers utilised for ice deposition; *right image*: ice accumulation on the cold fingers, showcasing visible ice growth and its fractured structure; images courtesy of LUWEX team and Luca Kiewiet.

8.1 Methodology

This plan aims to validate experimental measurements against existing COMSOL models and ensure that the models accurately represent experimental processes. Key phenomena considered are the phase transitions including extraction or sublimation, outgassing, deposition, delamination, and liquefaction under various initial conditions of temperature, pressure, and time. Therefore, the objective here is to validate COMSOL models by comparing simulated results with experimental data from LUWEX.

8.1.1 Step 1: Calibration of Ice and Regolith

The process begins with calibrating material properties as outlined in table 8.1, with a focus on the physical characteristics of the regolith simulant and the ice formation. Bulk densities for both LHS-1 and ice are measured before experimentation. This step also involves validating the mixing model for ice and regolith in COMSOL simulations. Deviations between porosity ϵ and pore filling fraction F require model adjustments for accuracy. The mixing model, described in Section 3.4.4, integrates the thermal conductivities of regolith and ice, accounting for gas conductivity due to sublimation.

8.1.2 Step 2: Define Experimental Conditions

With material properties established, initial conditions are set to ensure consistency between COMSOL and LUWEX simulations. Table 8.2 summarises these conditions, including an initial pressure of 1e-4 Pa and temperature of 140 K in the TVAC. To evaluate ambient temperature effects on extraction, the temperature will vary across trials. Each icy-regolith sample is prepared with a unique mass m and initial water-ice content C_i, which influences filling levels within the crucible. System variables like maximum temperatures and the rotation speed of the stirring mechanism are defined to ensure accurate monitoring of the experiments.

8.1.3 Step 3: Set Up COMSOL Simulations

This phase involves configuring parameters, mesh, and solvers in COMSOL to reflect the defined experimental conditions. Temperature, pressure, and sample mass affect filling level, requiring geometry adjustments in COMSOL. For each sample mass, a certain height z_{LVL} or filling level can be calibrated, with mesh refinement modified for accuracy. This height is adjustable according to the filling level and sample mass. Specific process models are incorporated: free molecular flow and fluid dynamics for sublimation and outgassing, phase change modelling for vapour deposition to solid phases, delamination, and liquefaction for ice-to-water transition, integrating heat transfer for thermal interactions.

8.1.4 Step 4: Run Baseline Simulations and Gather Experimental Data

Baseline simulations are executed in COMSOL with initial conditions independent of experimental data to establish expected system behaviour. Experimental trials follow under controlled conditions, documenting initial and boundary conditions such as temperature and pressure. Key variables are tracked over time for each phenomenon, and final outcomes like water extraction quantity and delamination extent are analysed.

8.1.5 Step 5: Compare Simulation Results with Experimental Data

Simulation results are compared with experimental data to validate COMSOL model accuracy. This comparison includes a time-series analysis of temperature and pressure profiles and an assessment of phenomena like extraction rates, deposition, delamination, and liquefaction.

8.1.6 Step 6: Model Calibration and Adjustment

Calibration involves addressing identified discrepancies between simulations and experimental data. Parameter adjustments in COMSOL, such as boundary conditions and model assumptions such as cooling temperature T_c, heat flux inputs, or phase transition intervals, are applied for improved alignment. Calibrated simulations are rerun to verify enhancements.

8.1.7 Step 7: Validation and Verification

To ensure reliability, validation tests are performed according to LUWEX standards, encompassing a range of initial conditions to rigorously evaluate model robustness. Verification metrics, such as the root mean square error, are used for a quantitative assessment of model performance.

8.1.8 Step 8: Design Revision and Iterations

Following the validation and verification process, the next phase involves revisiting the design and refining the model based on the insights gathered. This step includes incorporating the validated parameters, iterating steps 6-9, adjusting system variables, and making design revisions where necessary to improve model performance. Any discrepancies or areas of improvement identified during the verification phase are addressed, and the model is further optimised for accuracy and efficiency.

8.1.9 Step 9: Document Results and Update Models

The findings, including error analysis, calibration adjustments, and validation outcomes, are documented comprehensively. COMSOL models are updated with validated parameters, enhancing future predictive accuracy. This documentation not only serves as a reference for current applications but also facilitates future model refinements, ensuring continuous improvement through iterative validation cycles.

8.2   Step 1: Calibration of Ice and Regolith

Studies by Henning *et al.* as part of the LUWEX project indicate that bulk densities for were measured in the range of 1200 to 1500 kg/m^3 Wache [2024]. Furthermore, the thermal conductivity for ice particles are way off. In comparison with sample Icy-Regolith with simulant LHS-S1, the thermal conductivity denotes values in the range of 0.0075-0.02 W/m/K for single ice particles.

At this stage, it is also possible to validate the mixing model by Wasilewski [2021a] for ice and regolith in the COMSOL simulations. If significant deviations are observed between the porosity ϵ and the pore filling fraction F, the model can be adjusted to achieve more accurate conditions. This mixing model, previously described in Section 3.4.4, integrates the thermal conductivities of both regolith and ice. Notably, a gas conductivity term is included for cases where sublimation leads to the formation of vapour, although recent studies suggest that this gas contribution may be negligible Wache [2024]. Only the latent heat release significantly influences the effective thermal conductivity of the ice-regolith mixture.

8.2.1   Findings from Wache [2024] for LHS-1 and LUNEX

Initially, the thermal conductivities of the icy samples are notably low, comparable to those of dry regolith. However, as the temperature increases, the thermal conductivity values rise, likely due to the effects of sintering. When increasing the amount ice, C_i in samples, the sample exhibits a slightly higher initial conductivity. At approximately 220 K, there is a significant peak in thermal conductivity, which is likely attributed to latent heat transport. *Note*: the thermal conductivity values reported at this temperature may be subject to considerable uncertainty due to limitations in the measurement method, indicating that its interpretation must be only as order-of-magnitude estimates.

Furthermore, the gas diffusion component contributing to thermal conductivity appears negligible up to around 230 K, assuming a regime of free molecular flow. If the samples are heated to completion, thermal conductivity values revert to levels comparable to dry regolith around 250 K. It is crucial to mention that the experiments were conducted over several days, during which outgassing was a time-consuming process.

Variable	Model	LUNEX	LHS-1	Icy LHS-1	Ice Particles S1	Unit
ρ_r	3240	3240	3240	3240	NaN	kg/m^3
ρ_i	916.7	NaN	NaN	917	917	kg/m^3
ρ_{ib}	70	NaN	NaN	290	290	kg/m^3
ρ_{rb}	1400	1380	1580	NaN	NaN	kg/m^3
ρ	1470	NaN	NaN	1520	NaN	kg/m^3
ϵ for Regolith	0.57	0.57	0.51	NaN	NaN	1
ϵ for Icy-Regolith	0.55	NaN	NaN	0.53	NaN	1
ϵ for Ice Particles	0.92	NaN	NaN	NaN	0.68	1
F for Regolith	0.13	0.43	0.49	NaN	NaN	1
F for Icy-Regolith	0.14	NaN	NaN	0.48	NaN	1
F for Ice Particles	Inf	NaN	NaN	NaN	0.32	1
d_p	43.6	55	65	65	NaN	μm
C_i	4.75	0	0	2.24	100	%

TABLE 8.1: The system variables for the samples used in the experiments, specifically LUNEX and LHS-1 as reported by Wache [2024], include measured values that are adapted and supplemented with calculations for porosity ϵ using equations 5.4 and 7.6. Some of the parameters show notable discrepancies, highlighting the need for calibration to ensure accuracy. Values that are unknown, undefined, or irrelevant are denoted by *NaN*.

8.2.2 Validation of Thermal Conductivity from sections 3.4.4 and 5.2.1

The thermal conductivity of icy-regolith is influenced by the baseline conductivity of the regolith, k_r, the thermal conductivity of the ice particles, k_i, and a gas conductivity term, k_g, which becomes significant when the ice sublimates into water vapour. However, findings by Wache [2024] suggest that the gas term is negligible below approximately 230 K. As a result, the gas conductivity term is set to zero, $k_g = 0$. The overall thermal conductivity of icy-regolith can therefore be expressed as:

$$k = \epsilon F k_i + k_r, \tag{8.1}$$

where k represents the thermal conductivity of icy-regolith according to the *Volumetric Mixing Model* in section 5.2.1. The filling fraction F is calculated as:

$$F = \frac{\rho_{rb}/(1 - C_i) - \rho_{rb}}{\epsilon \rho_i}, \tag{8.2}$$

The measured values from table 8.1 can now be applied. For a sample of ice-regolith using the LHS-1 simulant, porosity ϵ and volume filling fraction F are found to be 0.53 and 0.48, respectively. *Note:*Wache [2024] introduces a scaling factor as a free parameter to account for deviations from a mono-disperse packing of spherical regolith particles. Changes in packing structure imply variations in heat transfer properties. For initial validation purposes, this scale factor is set to one, implying no effect on the thermal conductivity validation.
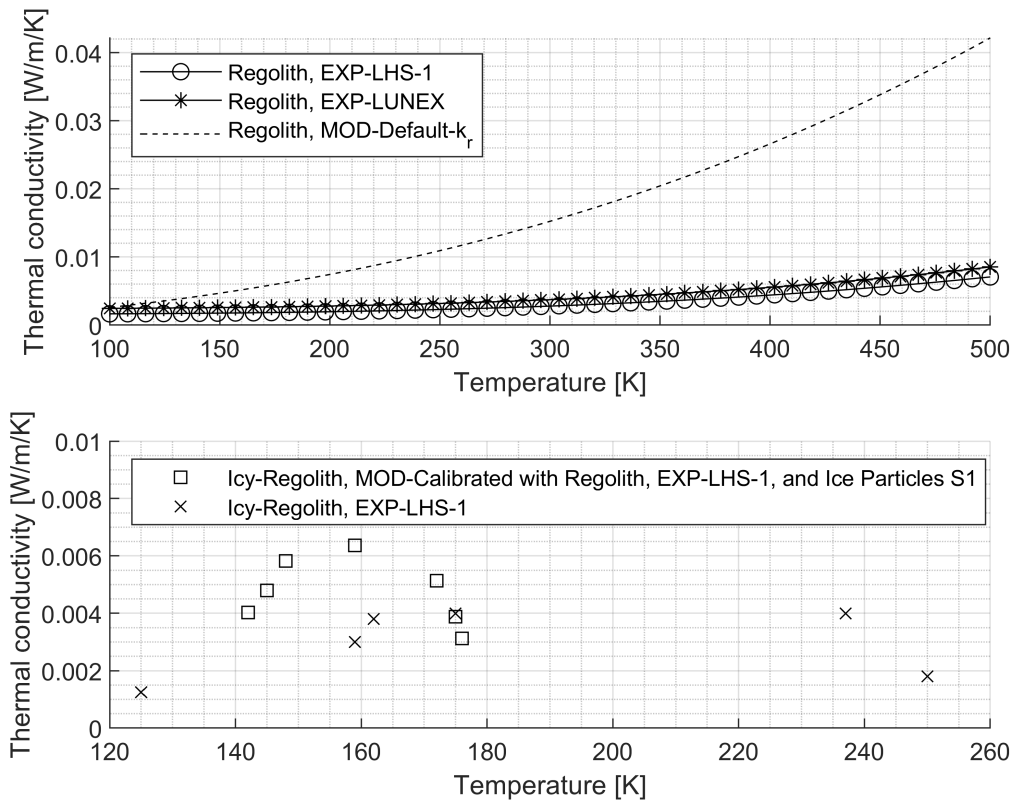

FIGURE 8.2: Calibration of Ice and Regolith Using the *Volumetric Mixing Model* from section 3.4.4 *Note*: The calibration involves fitting data for regolith, EXP-LHS-1, and EXP-LUNEX using Watson's equation $a + b \cdot T^3$. The coefficients were adapted from Wache [2024]. In this context, MOD indicates the model predictions, while EXP refers to the experimental measurements.

Significant differences in regolith's thermal conductivity are evident when comparing fig. 5.4 and fig. 8.2. Furthermore, the conductivity of the ice is notably inconsistent. In Figure 5.4, the conductivity of the ice reaches up to 4 W/m/K, while Henning's measurements for *ice particles S1* do not exceed 0.02 W/m/K. This suggests that the conductivity relationships shown in Figure 5.4, based on the analytical functions in Appendix B (specifically B.1 *Analytic Functions*), require reconsideration.

The significant deviation in ice conductivity is attributed to the porous structure of the ice particles. While k_i represents more the behaviour of glacial ice found on Earth, the ice prepared for the LUWEX project has a different structure with notable porosity. This indicates that the conductivity functions for both ice and regolith need to be adjusted according to LUWEX standards.

If eq. 8.1 is calibrated using the values from table 8.1, the resulting thermal conductivity of icy-regolith is labelled as *Icy-Regolith, MOD-Calibrated with Regolith, EXP-LHS-1, and Ice Particles S1*. This calibrated result is shown in the bottom part of fig. 8.2. A large deviation at lower temperatures is still apparent, possibly due to the high fluctuations in the thermal conductivity of *Ice Particles S1* and related uncertainty, as noted by Henning Wache [2024]. It may also be influenced by the volume filling fraction as determined by eq. 8.2. Table 8.1 shows significant differences in F between the model (0.14) and the experimental values for *Icy LHS-1* (0.48). Additionally, singular ice particles show extreme volume fractions. These findings suggest that the volume filling fraction requires a re-evaluation.

By refining the volume filling fraction, the *Volumetric Mixing Model* can still provide accurate results. The model remains practical for implementing phase change in regolith, so it is unnecessary to state the entire model invalid. Future work should focus on refining the filling fraction to produce more accurate thermal conductivity values for icy-regolith, aligning model outcomes with experimental data, thus ensuring the *Volumetric Mixing Model* from sections 5.2.1 and 3.4.4 holds under these conditions.

8.3 Step 2: Define Experimental Conditions

With the material properties established, the next step involves setting precise initial conditions to ensure consistency across modelling and the performed experiments. Table 8.2 provides a summary of these initial conditions. In the TVAC, the initial ambient pressure and temperature are set to 1e-4 Pa and 140 K, respectively. *Note*: the initial temperature defines the temperature of the sample inside the crucible. This excludes the filling process through the funnel for which the sample denotes a different temperature. Due to sample preparation including liquid nitrogen, the initial temperature when entering the funnel will not be equivalent to 140 K.

Variable	Description	Model	Experiment	Unit
T_0	Initial / Ambient temperature	140	140	K
T_{max}	Maximum temperature for control	333.15	333.15	K
p_0	Pressure inside vacuum chamber	$1 \cdot 10^{-4}$	$1 \cdot 10^{-4}$	Pa
rpm	Rotations per minute	3	3	1/min
P	Power input per cartridge heater	100	100	W
C_i	Initial water content	4.75	5	%
m	Mass of icy-regolith sample	15.01	15	kg

TABLE 8.2: The experimental conditions and initial values within the TVAC must be aligned with 100% accuracy, as any discrepancies can significantly impact the entire water extraction process. Ensuring precise control and monitoring of these parameters is critical to maintain consistency and reliability throughout the experiment.

8.4 Step 3: Set Up COMSOL Simulations

The next phase of the experimental setup involves carefully defining parameters, configuring the mesh and solver, and setting up models for specific processes within COMSOL. To begin with, experimental conditions from the previous step such as temperature and pressure must be accurately input into the COMSOL models. This step ensures that simulations closely mirror the physical conditions under which the experiments will be conducted.

Following parameter definition, configuring the mesh and solver is essential. The sample mass, which affects the filling level inside the crucible, necessitates alignment of the geometry in COMSOL. For each new sample mass, the height z_{LVL} must be adjusted, ensuring the model reflects the correct sample volume. Consequently, this adjustment also requires modifications in mesh refinement to maintain an accurate representation of the geometry:

1. Set the filling level, denoted as z_{LVL}.

2. Run the simulation using the default solver settings.

3. Refine the mesh if the baseline simulation does not converge.

4. Increase the damping factor and reduce the step size to aid convergence; adjust the tolerance once stability is achieved and the solver has converged.

5. *Note*: Take model nonlinearity into account depending on the COMSOL setup. For example, the ice-deposition model is significantly more non-linear than the liquefaction model.

For extraction and outgassing, dedicated models incorporate free molecular flow and fluid dynamics to capture the behaviour of vapour, considering **sublimation**. For **deposition**, a separate model simulates water vapour deposition, with phase change considerations included to address transitions from vapour to solid phases. **Delamination** is modelled subsequent to deposition to obtain uncoupling of ice. Lastly, for **liquefaction**, a model simulates the phase transition from ice to liquid water.

8.5 Step 4: Run Baseline Simulations and Gather Experimental Data

In this step, the focus shifts to executing baseline simulations and gathering experimental data. The COMSOL models will be run using baseline initial conditions, which will not rely on experimental data. This approach aims to establish the expected behaviour of the system under predefined parameters such as temperature control. In section 5.6, it became clear that optimisation for cartridge heaters solely was possible based on its maximum temperature correspondence. Therefore, the next section provides the maximum temperature behaviour along the process of sublimation, discussed in Chapter 5.

8.5.1 Temperature Control, Advancing from section 5.6

The sublimation rates shown in figures 5.7 and 5.6 represent the phase transition from ice to water vapour at three distinct rotational speeds. For these speeds, the maximum temperature is measured at the boundary where heat is applied, specifically near the cartridge heater. Analogous to eq. 7.10, temperature control can be mathematically expressed as:

$$\lim_{T \to T_{\max}} \frac{P}{\zeta N} = 0, \tag{8.3}$$

where T is the temperature at the rod's boundary (A_{rod}), and $T_{\max} = 333.15\,\text{K}$. Here, P denotes the effective power applied across the entire icy-regolith sample and depends on the ratio ζ and the number of cartridge heaters N. This condition implies that as the boundary temperature approaches $T_{\max}$, the effective power applied by each heater approaches zero.
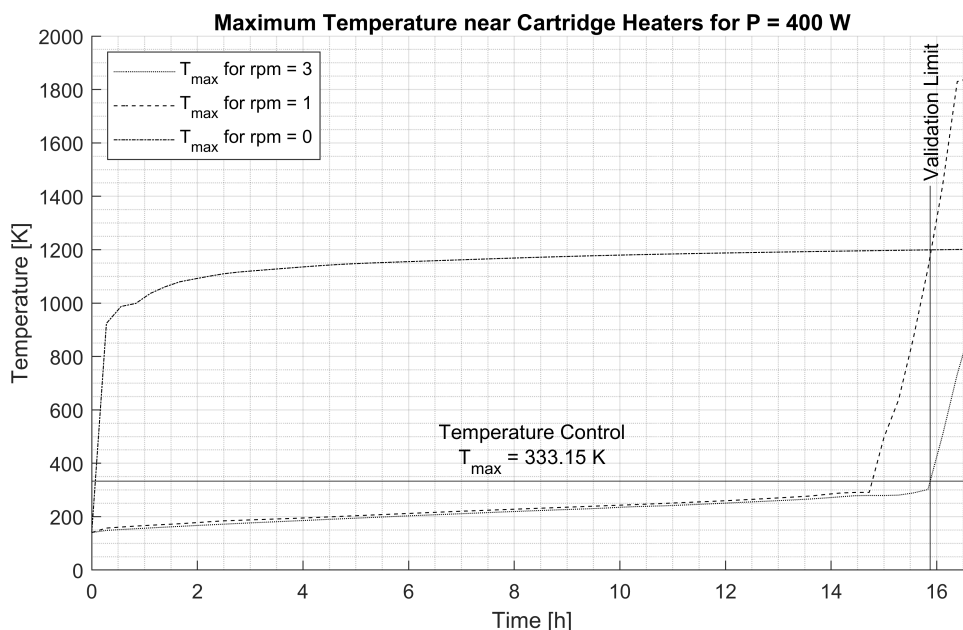
FIGURE 8.3: Maximum temperatures for three different rotational speeds; for the case without rotation, the maximum temperature surpasses 1000 K, posing a significant risk of sintering and is thus excluded from further analysis; for rotational speeds greater than zero, the maximum temperature gradually rises due to the rotation effect, eventually exceeding the temperature control threshold defined as T_{max}.

While higher extraction rates may seem beneficial, maintaining optimal thermal management is essential, particularly at high power levels, such as 400 W. For rotational speeds greater than zero, the maximum temperature gradually increases, confirming improved heat transfer due to rotation. When the temperature surpasses the phase transition point of 273.15 K, the maximum temperature at the heater boundaries rises significantly. The delayed increase in maximum temperature for rpm = 3 can be attributed to the formation of *cold spots*, which often develop near the cartridge heater and lower the overall temperature, thus affecting the boundary's maximum temperature.

For example, at rpm = 3, the maximum temperature reaches the defined temperature control limit of $T_{\max} = 333.15\,\mathrm{K}$ after 15.88 hours. If temperature sensors used in experiments confirm this condition, it would validate the model up to 15.88 hours. This specific time frame is thus considered the *Validation Limit* for rpm = 3. A similar approach can be applied to other rotational speeds. By referring to the mass fraction of ice shown in Figure 5.7 (P = 400 W), it is observed that at the validation limit, approximately 21% of the ice remains in the sample. This method indicates that the sublimation rates calculated in Chapter 5 are valid only up to specific time points. For rpm = 3, this means that after 79% of the ice has sublimated, temperature control as described by Equation 8.3 becomes active.

Building on the analysis in Section 5.6, a clear recommendation can now be made regarding the choice of rotational speed. The maximum temperature for lower rotational speeds is notably higher, which must be avoided to prevent the risk of sintering and changes in other mineral properties Farries et al. [2021]. This analysis enforces the need for strict temperature control of the cartridge heaters to prevent overheating and ensure the stability of the regolith. Maintaining stable regolith conditions is crucial for allowing the LUWEX team to reuse the regolith simulant efficiently. Following these baseline simulations, experimental data collection will be conducted. Additionally, significant variable changes over time will be recorded for each studied phenomenon, facilitating detailed analyses of their dynamics.

8.6 Step 5: Compare Simulation Results with Experimental Data

In Step 5, the focus shifts to comparing the simulation results with experimental data collected in the previous phase. This step is crucial for validating the accuracy and reliability of the COMSOL models. The first component of this analysis involves a time series comparison, in which both the simulation and experimental data are evaluated over time. This comparison assesses the consistency between temperature and pressure profiles, ensuring that the simulated behaviours align with observed conditions.

8.6.1 Key Variables

Beyond comparing temperature and pressure, the following key variables are critical for evaluating the results from the models against experimental data. For the deposition phase, ice growth can be monitored over time, with frost density measured through imaging connected to the cold trap. For a

Key Variable	Description	Unit
$\partial\delta/\partial t$	Ice growth rate	m/s
P	Low-pressure sensor reading	Pa
T	Temperature r	K
ϵ	Porosity of the ice	1
E_{sub}	Energy used for sublimation	J
E_{delam}	Energy used for delamination	J
E_{dep}	Energy used for deposition	J
E_{liq}	Energy used for liquefaction	J

TABLE 8.3: Key variables for analysis

comprehensive time-series analysis, pressure and temperature data can be examined for locations such as the cold trap, where the known temperature and pressure at the cold finger serve as a reference. Additionally, the energy used for processes like sublimation, delamination, deposition, and liquefaction should be considered to provide deeper insights into the system's behaviour. The default pressure and temperature profiles for the deposition model are shown in fig. 8.6. Meanwhile, the actual experimental data for pressure during extraction is presented in fig. 8.5. This detailed comparison, including energy usage for key processes, helps identify discrepancies and supports further calibration to align simulations with experimental observations.

8.6.2 Comparing Simulation Results with Experimental Data

The experimental ice growth rate, $\partial\delta/\partial t$, is shown in fig. 8.4. From 12:00, an incremental increase can be observed as the deposition continues steadily until the end of the experiment. Notably, in fig. 6.7, the modelled deposition rate is capped at $\delta_{max} \approx 4.15$ mm ($\rightarrow 52$ grams). For a valid comparison, the transient behaviour in the simulation should be examined up to 16:30, where it reaches an ice thickness comparable to that observed in the experiment.

The most noticeable difference lies in the duration; the optimised model completes the deposition in under an hour, whereas the experimental data indicates a period of approximately 4.5 hours (12:00 to 16:30). *Note:* starting from 12:00, ice begins forming and surpasses the assumed initial thickness, δ_{in}, in the model, establishing this point as the starting reference for comparison. The discrepancy in growth rates between the simulation and experiment is significant. Earlier validation of the deposition model revealed limited sensitivity to the sublimation rate due to pressure constraints. Consequently, pressure measurements throughout the experiment are essential for comparison.
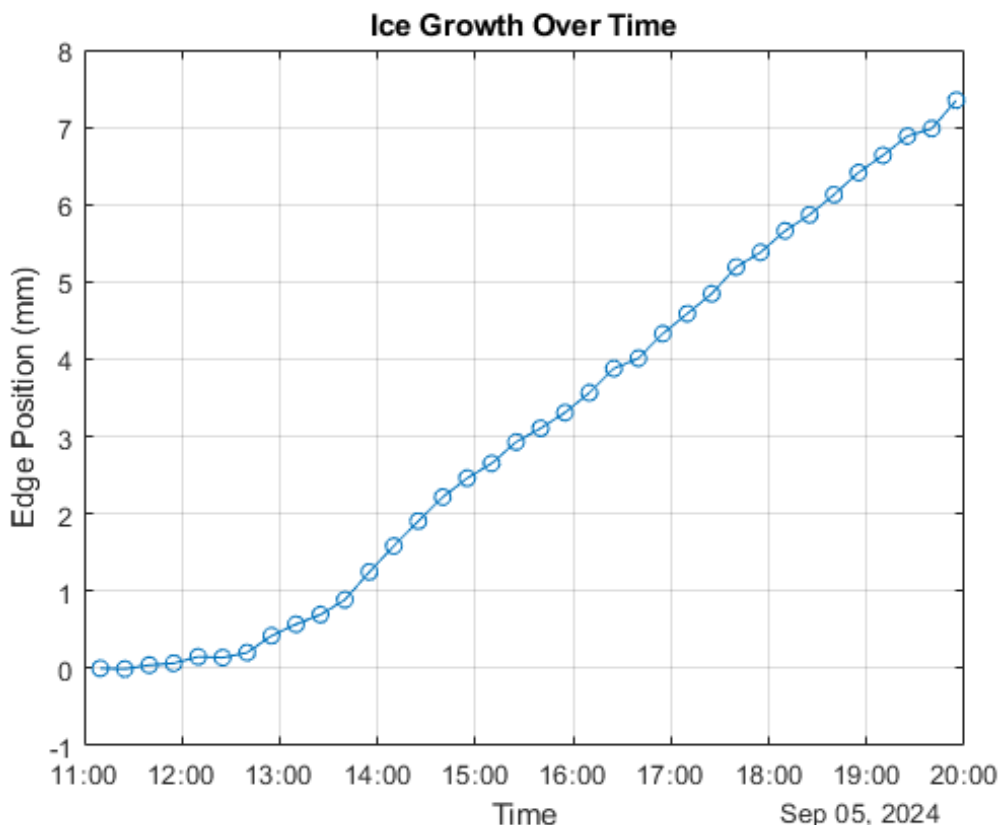
FIGURE 8.4: Deposition rate or ice growth over time inside the cold trap, showing the edge position over time with a magnitude equivalent to the ice frost thickness. This data is part of the LUWEX project, courtesy of Luca Kiewiet.

The pressure behaviour within the cold trap is illustrated in fig. 8.5, analysed at three key points:

1. Initial pressure increases as vapour enters the cold trap, peaking at 100 mbar (10 kPa) due to atmospheric pressure. *Note*: The low-pressure sensor, while highly accurate at low pressures, underestimates high-pressure readings, resulting in a 10 kPa measurement instead of 100 kPa.

2. A stable, low pressure is observed during nighttime when heaters are inactive, reducing sublimation inside the crucible. Once powered during the day, the heaters induce sublimation, causing a pressure rise that stabilises between points $2 \rightarrow 3$ at around 0.1 mbar (10 Pa).

3. This point represents a pressure increase from a 20°C temperature increment applied to the cartridge heaters.

A comparison with simulated results reveals a significant deviation, with the model's peak pressure reaching only 3 mPa, much lower than the 10 Pa observed between $2 \rightarrow 3$. This discrepancy is primarily attributed to the simplifications inherent in the 1D model, which will be discussed further. This section highlights the need for further examination of 1D modelling limitations, especially concerning pressure representation.
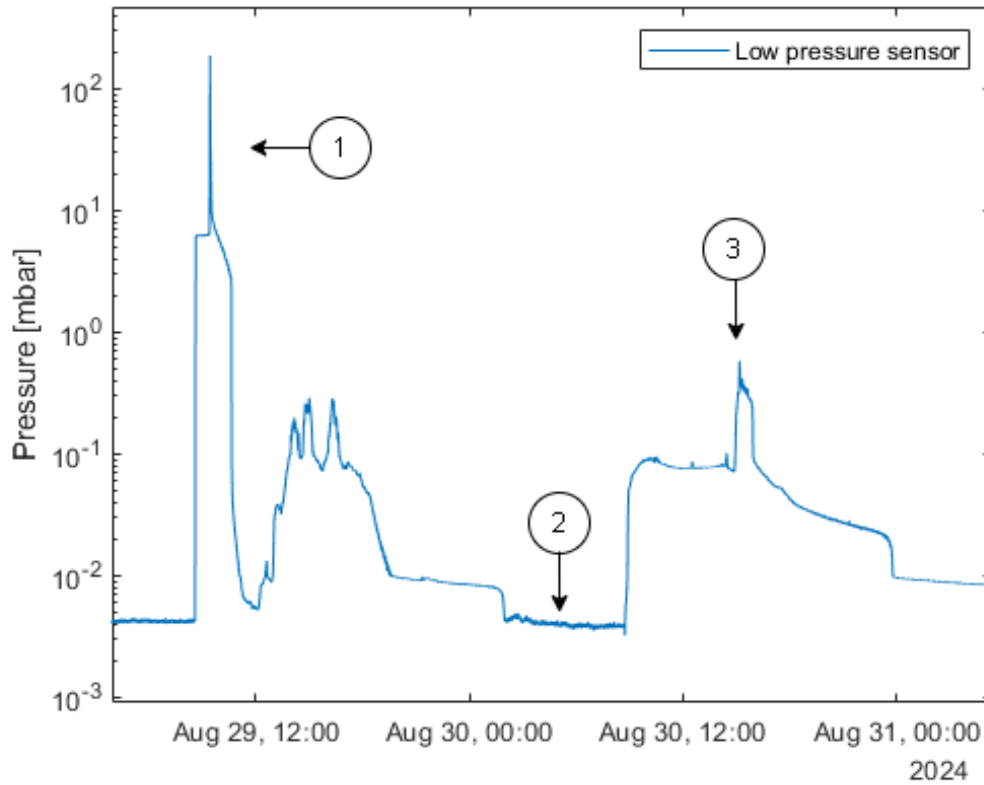
FIGURE 8.5: Pressure sensor readings inside the cold trap over time, showing low-pressure measurements from the LUWEX project, courtesy of Luca Kiewiet.

8.7 Step 6: Calibration and Model Adjustment

This step focuses on refining the model to enhance the correlation between simulation results and experimental data. The initial objective is to identify any major discrepancies between the model's predictions and the actual experimental results. Once these differences are observed, parameter tuning is conducted. This involves modifying essential parameters within the COMSOL model, such as power or heat flux inputs and phase transition time frames, as outlined in table 8.4—to better match the experimental findings. After making these adjustments, simulations should be rerun to confirm that the revised parameters lead to outputs that align more closely with the experimental data. Based on data for ice growth shown in fig. 8.4, parameters like the initial ice thickness, δ_{in}, and associated starting conditions can be modified. The existing settings establish the initial ice layer formed (at $t < 0$) over an approximate duration of one second. Extending this time interval can significantly alter the initial conditions, subsequently impacting the deposition rate shown in Fig. 6.7. By fine-tuning the initial conditions, changes in the asymptotic behaviour can be observed.

Note: The experimental data for ice growth over time does not cover the complete process up to delamination. This suggests that while the model's behaviour may remain valid, it might not accurately represent the initial phase of deposition.
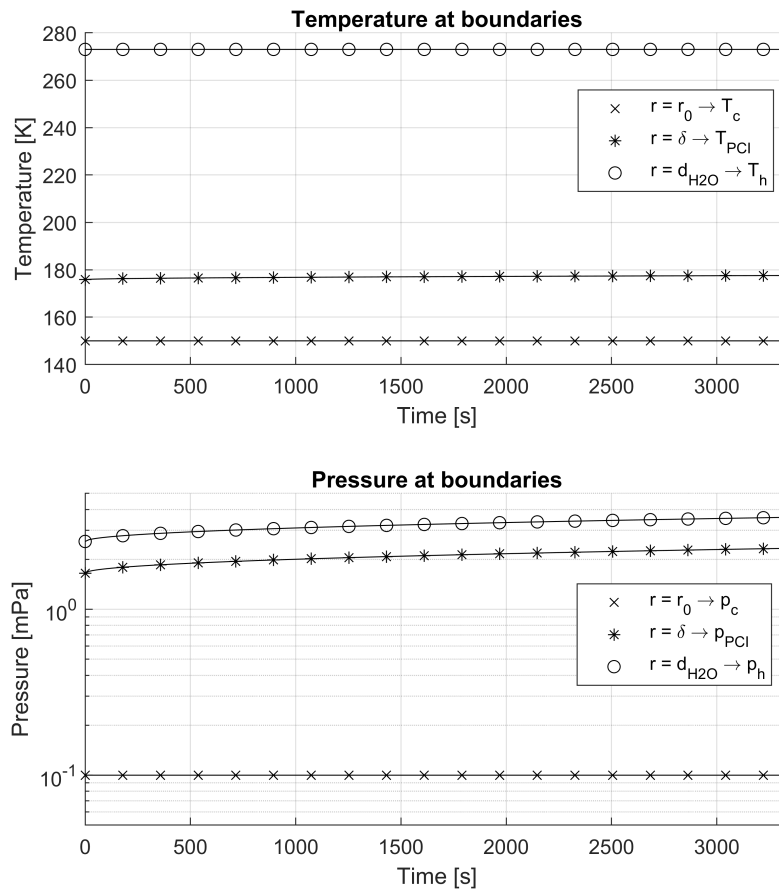
FIGURE 8.6: Simulated pressure and temperature at the boundaries within the cold trap, as represented in the mathematical model (refer to fig. 6.3).

8.8   Validation, Verification, and Conclusion

The final phase of model development focuses on thorough validation, verification, and detailed documentation to confirm the reliability and accuracy of the COMSOL models under various conditions. Validation will start with LUWEX-standard tests, supplemented by experiments conducted under different initial conditions to rigorously evaluate model robustness.

To move forward with validation, the issues identified in the deposition model outlined in section 6.5.1 must be addressed. A key consideration is whether the deposition process shows low sensitivity to fluctuations in molecular inlet flux, given that phase change may be more strongly influenced by pressure conditions. Experimental pressure data indicate a relatively stable behaviour during the transition from state $2 \rightarrow 3$, suggesting minimal sensitivity to inlet flux variations. This supports the hypothesis that deposition is primarily governed by pressure stability.

However, if adjustments to δ_{in} and initial conditions fail to yield consistent deposition behaviour, extending the 1D model becomes necessary. Ensuring that the mass conservation equation is fully applied and accounting for the impact of pressure variations would enhance the model's accuracy. Additionally, modelling ice deposition in two dimensions could be more straightforward, as the current simulation parameters struggle to accommodate density variations effectively (sublimation). Investigating molecular fluxes and their transient effects on deposition could elucidate any discrep-

Variable	Description	Unit
q_{int}	Heat flux at the boundary of ice (liquefaction)	W/m²
T_{PCI}	Temperature at PCI	K
m_{PCI}	Mass flux at PCI	kg/m²/s
T_h	Temperature of water vapour at inlet cold trap	K
T_c	Cooling temperature of cold finger	K
δ_{in}	Initial ice frost thickness	mm
P	Effective power input in sample (sublimation)	W
ΔT	Transition interval temperature	K

TABLE 8.4: Key parameters available for tuning in COMSOL models

ancies between the model and experimental observations. Upon completing the validation, the next step involves comprehensive documentation. This phase includes summarising experimental and simulation results, conducting error analysis, detailing model adjustments, design changes, and final validation outcomes. This documentation is crucial for understanding the model's performance and identifying opportunities for future improvements.

Following this, the validated parameters and configurations will be integrated into the COMSOL models to ensure they reflect the most accurate and up-to-date data, supporting ongoing refinements. This structured validation serves as a strategic plan for the LUWEX project, guiding future work. Although the experimental phase is ongoing, current progress has shown a clear correlation between the COMSOL models and experimental parameters. Future research should focus on refining the filling fraction to enhance the precision of thermal conductivity estimates for icy-regolith, aligning model outputs with experimental findings, and verifying the Volumetric Mixing Model described in sections 3.4.4 and 5.2.1 under specific conditions. The models, which cover sublimation, liquefaction, delamination, and deposition, demonstrate promising reliability in validating future experimental results. This approach ensures adaptability and supports continuous validation efforts throughout the water extraction process.

9 | Discussion & Future Work

Achieving **Sublimation** requires applying sufficient heat to the icy-regolith mixture to overcome the latent heat of sublimation. This study has shown that stirring significantly enhances the sublimation process, thereby reducing the heating time. However, the main challenge in this process lies in the poor thermal conductivity of regolith. As discussed in Chapter 8, the validated thermal conductivity of the icy-regolith mixture is even lower than expected, indicating that sublimation would take considerably longer than expected. In contrast, the conductivity of ice is much higher, suggesting that to optimise the process, it would be beneficial to reduce the porosity of the ice and aim for higher thermal conductivity values. Achieving a more uniform mixture of ice and regolith with improved thermal properties would drastically reduce the time required for sublimation.

From a modelling perspective, it was observed during the validation process that the volume filling fraction used in the thermal conductivity model of the icy-regolith mixture needs further revision. However, aside from this adjustment, the current rotating domain model of icy-regolith provides accurate results. To enhance the accuracy of the model further, additional interactions could be included, such as the effects of insulation materials, more detailed representations of stainless steel components, and the multi-body dynamics of the stirring mechanism. It is essential to recognise that each additional interaction or feature would increase the computational cost exponentially, making simulations more time-consuming. Despite this, the current model remains efficient in terms of CPU usage while still providing reliable and accurate results. This balance between accuracy and computational efficiency is crucial, especially when considering the practical application of the model.

The challenge in **deposition** lies in ensuring that the cold trap surfaces remain consistently cold enough to facilitate ice deposition without allowing vapour to escape into the surrounding environment. The current design of the cold trap is insufficient to cope with the high sublimation rates. To address this, the cold trap must be redesigned with a significantly larger control volume, ensuring that any velocity gradients along the flow path towards the phase change interface are minimised. This would result in a near-stationary domain of molecular fluxes, allowing for uniform deposition of ice across the entire surface of the cold trap. In turn, this would prevent any part of the cold surface from receiving more or less deposition, ensuring a homogeneous ice layer grows over time. To increase the amount of ice produced, the surface area of the cold trap must be maximised, and the current cold finger geometry is quite effective in this regard. When considering the process of delamination, the conical shape of the geometry ensures that the ice can more easily uncouple and fall away due to gravity. In summary, it would be optimal to have one specific cold surface inside a large control volume where water vapour enters. This design would minimise extreme molecular flux gradients, which currently hinder the deposition process. As it stands, the deposition rate has stabilised at approximately 50 grams per hour, which indicates substantial ice production in relation to the high sublimation rate of 296.9 grams per hour. This highlights the importance of redesigning the cold trap to facilitate continuous water capture, improving the efficiency of the process.

In terms of modelling the deposition process, careful consideration must be given to the initial conditions, as they significantly impact the overall process. The current deposition model would benefit from an extension to 2D modelling. Modelling 3D ice deposition under extreme vacuum

conditions, where free molecular flow is present, is practically infeasible due to the complexity and computational demands. Therefore, it is recommended to start by expanding the existing 1D model to a 2D version, which can replicate the behaviour of the current model. The boundary conditions used in the 1D model can be easily adapted and implemented into the 2D model, facilitating a smoother transition to more complex simulations.

Liquefaction, the process of transforming solid ice back into liquid water, presented no significant challenges in this study. The time required for the phase transition is relatively low, and heating the surrounding environment to facilitate the liquefaction of ice is straightforward. However, for lunar exploration missions, it is essential to minimise energy consumption for systems to ensure sustainability and optimal availability. This presents a challenge when considering the production of multiple batches of ice. If large masses of ice are to be liquefied, contact between the heated surface (in this study, a copper inlay) and the ice is necessary, as this significantly enhances thermal transfer through conduction. For smaller batches, the design of the liquefaction chamber must be revised to reduce the distance between the heated surface and the ice to minimise thermal losses. Optimising surface-to-surface radiation behaviour in such a design would improve the overall efficiency of the liquefaction process, ensuring that energy consumption remains low and that the system operates sustainably over extended periods.

10 | Conclusion

Over the past decade, significant advancements in space technology and exploration missions have confirmed the presence of water on the Moon, a discovery with implications for human life support and the establishment of a sustainable space environment. Water is crucial for sustaining the human presence in space, and it also offers a means to create rocket propellant through electrolysis, which separates water into hydrogen and oxygen. These elements, both integral to propulsion, exist on the Lunar surface both as isolated compounds and as water ice, embedded in the regolith. This utility places water at the core of ISRU strategies, which are essential for long-term space exploration and self-sufficient Lunar bases. This research investigates an optimised thermal extraction method for lunar water, specifically focussing on electrical heating, a more controllable and efficient approach compared to alternatives such as microwave heating. Although microwave techniques offer rapid heating, they face significant drawbacks, particularly in maintaining stable water vapour outgassing from the lunar regolith. Electrical heating has been selected for the process, using cartridge heaters installed within cylindrical rods that are inserted into a sample of regolith-ice mixture to initiate the sublimation stage. These rods are filled with magnesium oxide in their voids to optimise heat transfer efficiency. Additionally, a unique design feature is incorporated to improve heating performance: the rods are not only used as heating elements but are also rotated, further enhancing the heat distribution throughout the regolith. This rotation acted by a stirring mechanism that mobilises the regolith particles, significantly increasing the effective thermal conductivity. While regolith itself very poor thermal conductivity, this study has shown that this stirring mechanism enhances it by over 75% relative to baseline conductivity, thus accelerating the sublimation process. An analytical formula has been developed to quantify this effect, providing a calculation tool based on sample radius, rotation speed, and thermal properties (specific heat, baseline conductivity, and density), adaptable to various experimental setups. The result is a sublimation rate exceeding 296 grams per hour under optimal heating conditions (see table 10.1).

Once sublimated, the water vapour is directed to a secondary subsystem for capture. The primary objective in extracting water from regolith is capturing this vapour, as the end product in its gaseous form is not useful. Here, water undergoes another phase transition, deposition, transforming from vapour to solid ice on a cooled surface. The deposition process allows water vapour to transition on the surface until equilibrium is reached, at which point additional ice growth ceases. The deposition model requires expansion into a two-dimensional configuration due to the significant discrepancies between experimental results and simulations. However, the existing 1D model could still yield accurate results if initial conditions similar to those in the experimental setup are implemented. To release the accumulated ice, a delamination process is employed by heating the ice, resulting in a mass loss of only 7%. By gravitational force the ice is directed to the next subsystem: liquefaction. In this stage, the ice undergoes further heating to reach melting, converting to liquid water. While current simulations indicate that the applied heat flux for melting the ice remains minimal, the phase transition occurs rapidly. This suggests that as long as power input is sufficient to reach the energy threshold for phase change, liquefaction should not present significant issues. After the liquefaction phase, the resulting liquid water is directed to a storage system for subsequent purification. Given the likely presence of volatile compounds within the extracted water, purification is essential to meet the required standards for human consumption or potential use as a propellant.

Each subsystem has been designed and tested with the goal of achieving operational performance under conditions simulating the Lunar environment. Experiments were conducted in a thermal vacuum chamber, with pressures as low as $1 \cdot 10^{-6}$ mbar and temperatures reaching 140 K. Comprehensive multi-physics models support each experimental phase, allowing for analysis and validation of sublimation, deposition, and liquefaction stages. Additionally, the study extends the analysis of water vapour dynamics within the porous structure of the Lunar regolith, focusing on mass transfer via diffusion, with modelling revealing a diffusion coefficient of 0.185 mm^2/s. This finding surpasses previous estimates that relied solely on Knudsen diffusion, as it incorporates the molecular flux behaviour observed under high-vacuum conditions. Optimising and integrating these subsystems presented the greatest challenge, revealing complex dependencies between sublimation rates, deposition capacities, and liquefaction efficiency. For instance, a high sublimation rate may seem advantageous, yet becomes counterproductive if the system cannot subsequently capture and freeze the vapour at a matching rate. Currently, the cold trap's capacity cannot cope with the sublimation rates, causing the need for design improvements. Similarly, the liquefaction process completes within 200 seconds under ideal conditions, yet heating by radiative flux alone can take hours to bring ice to its melting point (273.15 K), indicating the need for more responsive heating solutions. Future work should address these design constraints, ensuring each stage operates within the overall system, a key step in refining ISRU technologies for practical applications.

In conclusion, this research addresses critical technical challenges in Lunar water extraction, each subsystem forming a link in ISRU-supply-chain that may eventually support a self-sustaining human presence on the Moon. With ongoing improvements in efficiency, the vision of a permanent Lunar base becomes attainable, positioning this study as a foundational contribution toward realising sustainable space exploration.

	Stage I	*Stage II*	*Stage III*
	Sublimation	**Deposition**	**Liquefaction**
Time [h]	16.1	0.7	1.0
Maximum Rate	296.9 [g/h]	50 [g/h]	2.5 [g/s]

TABLE 10.1: Summarised results for sublimation, deposition, and liquefaction processes. Sublimation rate is based on constant 400 W heating for rpm = 1; deposition occurs under optimised settings at stabilised conditions; liquefaction is achieved with $\varepsilon \mathcal{F} \approx 50$.

Bibliography

R. A. C. Bonales, L.J. and P. D. Sanz. Thermal conductivity of ice prepared under different conditions. *International Journal of Food Properties*, 20:610–219, 2017.

J. Brisset, T. Miletich, and P. Metzger. Thermal extraction of water ice from the lunar surface - a 3d numerical model. *Planetary and Space Science*, 193:105082, 2020. ISSN 0032-0633. doi: https://doi.org/10.1016/j.pss.2020.105082. URL https://www.sciencedirect.com/science/article/pii/S0032063320302956.

D. A. G. Bruggeman. Calculation of various physical constants of heterogeneous substances. i. dielectric constant and conductivity of mixed bodies from isotropic substances. *Annalen der Physik*, 416(7):636–664, 1935.

F. Brèque and M. Nemer. Frosting modeling on a cold flat plate: Comparison of the different assumptions and impacts on frost growth predictions. *International Journal of Refrigeration*, 69:340–360, 2016. ISSN 0140-7007. doi: https://doi.org/10.1016/j.ijrefrig.2016.06.010. URL https://www.sciencedirect.com/science/article/pii/S0140700716301724.

K. M. Cannon, D. T. Britt, T. M. Smith, R. F. Fritsche, and D. Batcheldor. Mars and lunar simulants developed by the exolith lab. *Planetary and Space Science*, 170:1–8, 2019. doi: 10.1016/j.pss.2019.01.008.

A. Colaprete. Detection of water in the lcross ejecta plume. *Science (New York, N.Y.)*, 330(6003): 463–468, 2010. URL https://doi.org/10.1126/science.1186986.

J. D. Cole, S. Lim, H. M. Sargeant, S. Sheridan, M. Anand, and A. Morse. Water extraction from icy lunar simulants using low power microwave heating. *Acta Astronautica*, 209:95–103, 2023. ISSN 0094-5765. doi: https://doi.org/10.1016/j.actaastro.2023.04.035. URL https://www.sciencedirect.com/science/article/pii/S0094576523002084.

COMSOL Multiphysics®. URL www.comsol.com.

J. Connolly and W. D. Carrier. Updating lunar subsurface geotechnical properties based upon nonlinear winkler modeling of apollo and lunahkod measurements. In *54th Lunar and Planetary Science Conference*, 2022. URL https://ntrs.nasa.gov/api/citations/20220018853/downloads/LPSC%202023%20Abstract_Connolly_Carrier_v2.pdf.

J. Connolly and W. D. Carrier. An engineering guide to lunar geotechnical properties. In *2023 IEEE Aerospace Conference*, pages 1–9, 2023. doi: 10.1109/AERO55745.2023.10115961.

I. A. Crawford. Lunar resources: A review. *Progress in Physical Geography: Earth and Environment*, 39(2):137–167, 2015. doi: 10.1177/0309133314567585. URL https://doi.org/10.1177/0309133314567585.

D. R. Criswell. Lunar solar power system: review of the technology base of an operational lsp system. *Acta Astronautica*, 46(8):531–540, 2000. ISSN 0094-5765. doi: https://doi.org/10.1016/S0094-5765(00)00015-1. URL https://www.sciencedirect.com/science/article/pii/S0094576500000151.

BIBLIOGRAPHY

E. S. A. (ESA). Heracles: Human-enhanced robotic architecture and capability for lunar exploration and science. Technical report, ESA, 2021. URL https://www.esa.int/Science_Exploration/Human_and_Robotic_Exploration/Exploration/HERACLES.

Exolith. Exolith simulants, 2023. URL https://exolithsimulants.com/collections/regolith-simulants. Accessed: 08.06.2023.

F. P. Fanale, J. R. Salvail, D. L. Matson, and R. H. Brown. Micro cold traps on the moon. *Nature Astronomy*, 5(1):169–175, 2021. ISSN 2397-3366. doi: 10.1038/s41550-020-1198-9. URL https://doi.org/10.1038/s41550-020-1198-9.

W. M. Farrell. Solar-storm/lunar atmosphere model (sslam): An overview of the effort and description of the driving storm environment. *NASA*, 2011. URL https://ntrs.nasa.gov/api/citations/20120012541.

K. Farries, P. Visintin, S. Smith, and P. Eyk. Sintered or melted regolith for lunar construction: state -of-the-art review and future research directions. *Construction and Building Materials*, 196, 05 2021. doi: 10.1016/j.conbuildmat.2021.123627.

D. W. Feldman. Lunar prospector finds evidence of ice at moon's poles. *NASA Press Release, 5 March 1998*, 1998. URL https://nssdc.gsfc.nasa.gov/nmc/spacecraft/display.action?id=1998-001A.

A. J. Flubacher, P. Leadbetter and J. A. Morrison. Heat capacity of ice at low temperatures. *The Journal of Chemical Physics*, 33/6:1751–1755, 1960.

J. A. Fountain and E. A. West. Thermal conductivity of particulate basalt as a function of density in simulated lunar and martian environments. *Journal of Geophysical Research (1896-1977)*, 75(20):4063–4069, 1970. doi: https://doi.org/10.1029/JB075i020p04063. URL https://agupubs.onlinelibrary.wiley.com/doi/abs/10.1029/JB075i020p04063.

G. R. Fowles and G. L. Cassiday. Analytical mechanics. *Journal of Applied Mechanics*, 44:98–106, 1977.

S. Fukusako. Thermophysical properties of ice, snow, and sea ice. 11(2), 1990.

B. F. G. Heiken, D. Vaniman. *Lunar Sourcebook: A User's Guide to the Moon.* 1991. URL https://www.sciencedirect.com/science/article/pii/S0094576500000151.

P. C. Goldstein, H. and J. Safko. *Classical Mechanics.* Addison-Wesley, Reading, Massachusetts, 2nd edition, 1980.

F. J. Guerrero-Gonzalez and P. Zabel. System analysis of an isru production plant: Extraction of metals and oxygen from lunar regolith. *Acta Astronautica*, 2023. URL https://api.semanticscholar.org/CorpusID:254330295.

N. Hab. *Modeling, Simulation and Comparison of Lunar Thermal Water Extraction Methods for Space Resource Utilization.* PhD thesis, Technical University of Munich, 2022.

G. Hao, S. Wang, H. Chen, W. Zhang, S. Jiang, and L. Li. Optimum energy efficiency in lunar in-situ water ice utilization. *Acta Astronautica*, 207:307–315, 2023. ISSN 0094-5765. doi: https://doi.org/10.1016/j.actaastro.2023.03.029. URL https://www.sciencedirect.com/science/article/pii/S0094576523001480.

P. Harris. *Space enterprise: living and working offworld in the 21st century.* 2008.

P. O. Hayne, A. Hendrix, E. Sefton-Nash, M. A. Siegler, P. G. Lucey, K. D. Retherford, J.-P. Williams, B. T. Greenhagen, and D. A. Paige. Evidence for exposed water ice in the moon's south polar regions from lunar reconnaissance orbiter ultraviolet albedo and temperature measurements. *Icarus*, 255:58–69, 2015. ISSN 0019-1035. doi: https://doi.org/10.1016/j.icarus.2015.03.032. URL https://www.sciencedirect.com/science/article/pii/S0019103515001335. Lunar Volatiles.

L. He, C. Wang, G. Zhang, Y. Pang, and W. Yao. A novel auger-based system for extraterrestrial in-situ water resource extraction. *Icarus*, 367:114552, 2021. ISSN 0019-1035. doi: https://doi.org/10.1016/j.icarus.2021.114552. URL https://www.sciencedirect.com/science/article/pii/S0019103521002256.

D. P. Hearth. *Center for Space Construction*. 1989. URL https://nssdc.gsfc.nasa.gov/planetary/factsheet/moonfact.html.

M. Heitkamp. Design and development of a lunar water extraction system for future isru technologies. Technical report, University of Twente, 2023.

D. Hillel. *Soil and Water: Physical Principles and Processes*. Academic Press, New York, 1971.

R. Hodges, J. Hoffman, and F. S. Johnson. The lunar atmosphere. *Icarus*, 21(4):415–426, 1974. ISSN 0019-1035. doi: https://doi.org/10.1016/0019-1035(74)90144-4. URL https://www.sciencedirect.com/science/article/pii/0019103574901444.

A. O. Hudson, T. L. and N. Schorghofer. Heat capacity of ice at low temperatures. *J. Geophys. Res. Planets*, 114/E1:E00A03, 2009.

E. S. Huetter, Koemle, N. I., G. Kargl, and E. Kaufmann. Determination of the effective thermal conductivity of granular materials under varying pressure conditions. *Journal of Geophysical Research: Planets*, 113(E12), 2008. doi: https://doi.org/10.1029/2008JE003085. URL https://agupubs.onlinelibrary.wiley.com/doi/abs/10.1029/2008JE003085.

G. H. P. S. Hörz F., R. Grieve and A. Binder. Lunar surface processes. *Lunar Sourcebook, Cambridge University Press, Cambridge.*, 1991.

K. Ikeya, F. J. Guerrero-Gonzalez, L. Kiewiet, M.-A. Cardin, J. Cilliers, S. Starr, and K. Hadler. Hybrid lunar isru plant: a comparative analysis with carbothermal reduction and water extraction. *ArXiv*, abs/2408.04936, 2024. URL https://api.semanticscholar.org/CorpusID:271843053.

L. Jakaite. About us, n.d. URL https://strike-dip.com/about/. Accessed: 2024-11-08.

F. S. Johnson and J. M. Carroll. Vacuum measurements on the lunar surface. *Journal of Vacuum Science and Technology*, 9:450, 1972.

L. M. Johnson. Atmospheric effects on lunar observations: Implications for telescopic observations and communication. *lanetary and Space Science*, 184, 2020.

A. Jones. China to launch 1st-ever sample return mission to moon's far side in 2024. 2023. URL https://www.space.com/china-moon-far-side-sample-return-mission-2024.

C. Kalis. Design of a water capturing system for thermal extraction of water on the moon. *Technical University Delft*, 2024. URL https://resolver.tudelft.nl/uuid:9f49b75a-d4f3-47ad-bf4a-4d75c2333ce6.

L. Kiewiet, N. M. Hab, F. M. Marchese, R. Freer, and P. Zabel. Trade-off and optimization for thermal lunar water extraction system. *International Astronautical Federation*, 2022.

K. J. Kossacki. Sublimation of porous granular ice in vacuum. *Icarus*, 368:114613, 2021. ISSN 0019-1035. doi: https://doi.org/10.1016/j.icarus.2021.114613. URL https://www.sciencedirect.com/science/article/pii/S0019103521002785.

J. LAGE. The fundamental theory of flow through permeable media from darcy to turbulence††dedicated in memory of my dear friend and father-in-law, mr. fernando d'olne soares de barros, 1902–1997. In D. B. INGHAM and I. POP, editors, *Transport Phenomena in Porous Media*, pages 1–30. Pergamon, Oxford, 1998. ISBN 978-0-08-042843-7. doi: https://doi.org/10.1016/B978-008042843-7/50001-5. URL https://www.sciencedirect.com/science/article/pii/B9780080428437500015.

BIBLIOGRAPHY

L. D. Landau and E. M. Lifshitz. Mechanics. *Course of Theoretical Physics, Volume 1*, pages 92–101, 1976.

S. Li. Direct evidence of surface exposed water ice in the lunar polar regions. *Proceedings of the National Academy of Sciences of the United States of America*, 115(36), 2018. ISSN 8907-8912. doi: https://doi.org/10.1073/pnas.1802345115.

M. R. Li S. Quantitative mapping of hydration in lunar pyroclastic deposits: Insights into water from the lunar interior. *45th Lunar and Planetary Science Conference*, 2014.

S. Lim, S. Reeve, E. Lekuona, A. Garbayo, T. Le Toux, A. Morse, J. Bowen, and M. Anand. Challenges in the microwave heating of lunar regolith – analysis through the design of a microwave heating demonstrator (mhd) payload. *Advances in Space Research*, 69(1):751–760, 2022. ISSN 0273-1177. doi: https://doi.org/10.1016/j.asr.2021.10.038. URL https://www.sciencedirect.com/science/article/pii/S0273117721007985.

H. Lin, S. Li, R. Xu, Y. Liu, X. Wu, W. Yang, Y. Wei, Y. Lin, Z. He, H. Hui, H. He, S. Hu, C. Zhang, C. Li, G. Lv, L. Yuan, Y. Zou, and C. Wang. In situ detection of water on the moon by the chang'e-5 lander. *Science Advances*, 8(1):eabl9174, 2022. doi: 10.1126/sciadv.abl9174. URL https://www.science.org/doi/abs/10.1126/sciadv.abl9174.

Z. Liu, J. Li, C. Yang, X. Wang, J. Xiao, L. Wang, and S. Meng. Cold sintering: A promising in situ resource utilisation strategy to densify lunar regolith simulants for construction applications. *Materials Design*, 238:112674, 2024. ISSN 0264-1275. doi: https://doi.org/10.1016/j.matdes.2024.112674. URL https://www.sciencedirect.com/science/article/pii/S0264127524000467.

K. M. Luchsinger, N. J. Chanover, and P. D. Strycker. Water within a permanently shadowed lunar crater: Further lcross modeling and analysis. *Icarus*, 354, 2021. URL https://www.sciencedirect.com/science/article/pii/S0019103520304322.

LUWEX. Validation of lunar water extraction and purification technologies for in-situ propellant and consumables production, 2022.

A. Mann. China's chang'e program: Missions to the moon. 2019. URL https://www.space.com/43199-chang-e-program.html.

A. Martinez and M. A. Siegler. A global thermal conductivity model for lunar regolith at low temperatures. *J. Geophys. Res. Planets*, 126/10:297, 2021.

H. G. H. McKay D. S., Fruland R. M. Grain size and the evolution of lunar soils. *Proceedings, 5th Lunar and Planetary Science Conference*, pages 887–906, 1974.

V. D. T. McKay D. S., Heiken G. H and F. B. M. The lunar regolith, in the lunar sourcebook. *Cambridge University Press, New York NY*, pages 285–356, 1991.

T. S. McKechnie, J. P. Ramsey, and W. J. Witt. Development of a new lunar highland simulant for isru applications. *Journal of Aerospace Engineering*, 33(4):04020032, 2020. doi: 10.1061/(ASCE)AS.1943-5525.0001093.

J. B. M. Mellon, M. T. and S. E. Postawko. The persistence of equatorial ground ice on mars. *J. Geophys. Res.*, 102/E8:19357–19369, 1997.

A. Nafsun. Heat transport through the active layer of the moving bed in rotary drums. *12th International Conference on Heat Transfer, Fluid Mechanics and Thermodynamics*, pages 373–379, 2016.

NASA. Cost analysis of transporting resources to the moon. *NASA Technical Reports*, 2020. URL https://www.nasa.gov/mission_pages/exploration/moon-transport-cost.html.

NASA. The Lunar South Pole. 2023a.

NASA. The moon; future missions. *Lunar and Planetary Science*, 2023b.

NASA. Draper lunar lander, 2024. URL https://nssdc.gsfc.nasa.gov/nmc/spacecraft/display.action?id=DRAPER. Accessed: 2024-11-08.

S. Noble. The lunar regolith. *NASA gov*, 2019.

M. Piquette, M. Horányi, and S. A. Stern. Laboratory experiments to investigate sublimation rates of water ice in nighttime lunar regolith. *Icarus*, 293:180–184, 2017. ISSN 0019-1035. doi: https://doi.org/10.1016/j.icarus.2017.04.017. URL https://www.sciencedirect.com/science/article/pii/S0019103516306789.

C. Purrington, G. Sowers, and C. Dreyer. Thermal mining of volatiles in lunar regolith simulant. *Planetary and Space Science*, 222:105550, 2022. ISSN 0032-0633. doi: https://doi.org/10.1016/j.pss.2022.105550. URL https://www.sciencedirect.com/science/article/pii/S0032063322001362.

D. P. R. L. R. Pappa, G. Rose. Solar power for lunar pole missions. 20200000285, 2020. URL https://ntrs.nasa.gov/api/citations/20200000285.

H. Sargeant. *Water from Lunar Regolith: Reduction by hydrogen for a small-scale demonstration of in situ resource utilisation for the Moon*. PhD thesis, University of Central Florida, 2020.

H. Sargeant, S. Barber, M. Anand, F. Abernethy, S. Sheridan, I. Wright, and A. Morse. Hydrogen reduction of lunar samples in a static system for a water production demonstration on the moon. *Planetary and Space Science*, 205:105287, 2021. ISSN 0032-0633. doi: https://doi.org/10.1016/j.pss.2021.105287. URL https://www.sciencedirect.com/science/article/pii/S0032063321001264.

J. B. M. O. T. M. m. Schieber, G. L. Indirect solar receiver development for the thermal extraction of h20(v) from lunar regolith: heat and mass transfer modeling. *Acta Astronautica*, 190/3:365–376, 2022.

L. M. Shulman. The heat capacity of water ice in interstellar or interplanetary conditions. *AA*, 461(1):187–190, 2004.

A. O. C. E. m. Siegler, M. 'measurements of thermal properties of icy mars regolith analogs. *J. Geophys. Res.*, 117/E3, 2012.

J. Smith. Thermal control strategies for lunar exploration. *Journal of Spacecraft and Rockets*, 55:498–512, 2018.

H. Song, J. Zhang, D. Ni, Y. Sun, Y. Zheng, J. Kou, X. Zhang, and Z. Li. Investigation on in-situ water ice recovery considering energy efficiency at the lunar south pole. *Applied Energy*, 298:117136, 2021. ISSN 0306-2619. doi: https://doi.org/10.1016/j.apenergy.2021.117136. URL https://www.sciencedirect.com/science/article/pii/S0306261921005766.

G. F. Sowers and C. B. Dreyer. Ice mining in lunar permanently shadowed regions. *New Space*, 2019.

G. F. Sowers and C. B. Dreyer. *Thermal Mining of Ices on Cold Solar System Bodies*. NASA Innovative Advanced Concepts (NIAC), 2020.

E. J. Speyerer and M. S. Robinson. Persistently illuminated regions at the lunar poles: Ideal sites for future exploration. *Icarus*, 222(1):122–136, 2013. ISSN 0019-1035. doi: https://doi.org/10.1016/j.icarus.2012.10.010. URL https://www.sciencedirect.com/science/article/pii/S0019103512004174.

P. D. Spudis. *The Geology of Multi-Ring Impact Basins: The Moon and Other Planets*. Cambridge University Press, Cambridge, 1996.

K. R. Symon. *Mechanics*. Addison-Wesley, 3rd edition, 1971.

L. A. Taylor, C. M. Pieters, A. D. Patchen, D.-H. S. Taylor, R. V. Morris, L. P. Keller, and D. S. Mckay. Mineralogical and chemical characterization of lunar highland soils: Insights into the space weathering of soils on airless bodies. *Journal of Geophysical Research*, 115, 2010. URL https://api.semanticscholar.org/CorpusID:12635751.

J. Thangavelautham. Challenges and opportunities in lunar exploration: A review. *Advances in Space Research*, 69(1):246–263, 2022.

P. Vacuum. Pfeiffer vacuum technologies. https://www.pfeiffer-vacuum.com/global/en, 2024. Accessed: 2024-11-08.

H. Wache. Thermal conductivity measurements of dry and icy lunar regolith simulants. *Institute of Geophysics and Extraterrestrial Physics*, 2024.

S. Wang, P. Guo, and L. Li. Numerical simulation revealing the impact of drilling-based mining equipment structure on water ice extraction from lunar soil. *Acta Astronautica*, 213:431–437, 2023. ISSN 0094-5765. doi: https://doi.org/10.1016/j.actaastro.2023.09.039. URL https://www.sciencedirect.com/science/article/pii/S0094576523005040.

T. G. Wasilewski. Lunar thermal mining: Phase change interface movement, production decline and implications for systems engineering. *Planetary and Space Science*, 199:105199, 2021a. ISSN 0032-0633. doi: https://doi.org/10.1016/j.pss.2021.105199. URL https://www.sciencedirect.com/science/article/pii/S0032063321000386.

T. G. Wasilewski. Lunar thermal mining: Phase change interface movement, production decline and implications for systems engineering. *Planetary and Space Science*, 199:105199, 2021b. ISSN 0032-0633. doi: https://doi.org/10.1016/j.pss.2021.105199. URL https://www.sciencedirect.com/science/article/pii/S0032063321000386.

S. M. A. Woods-Robinson, R. and D. A. Paige. A model for the thermophysical properties of lunar regolith at low temperatures. *J. Geophys. Res. Planets*, 124/7:1989–2011, 2019.

L. Xin. China planning to offer more space for foreign equipment on future chang'e 8 moon mission. 2023. URL https://www.scmp.com/news/china/science/article/3236807/china-planning-offer-more-space-foreign-equipment-future-change-8-moon-mission.

L. Yang, Y. Li, and Y. Zhang. Numerical investigation of the ground-based thermal environment experimental approaches to reveal the ice-sublimation phenomenon inside lunar regolith. *Acta Astronautica*, 205:295–309, 2023. ISSN 0094-5765. doi: https://doi.org/10.1016/j.actaastro.2023.02.013. URL https://www.sciencedirect.com/science/article/pii/S0094576523000656.

H. Yano, A. Kieda, and I. Mizuno. The fundamental solution of brinkman's equation in two dimensions. *Fluid Dynamics Research*, 7(3):109–118, 1991. ISSN 0169-5983. doi: https://doi.org/10.1016/0169-5983(91)90051-J. URL https://www.sciencedirect.com/science/article/pii/016959839190051J.

P. Zhang, W. Dai, R. Niu, G. Zhang, G. Liu, X. Liu, Z. Bo, Z. Wang, H. Zheng, C. Liu, H. Yang, Y. Bai, Y. Zhang, D. Yan, K. Zhou, and M. Gao. Overview of the lunar in situ resource utilization techniques for future lunar missions. *Space: Science & Technology*, 3:0037, 2023. doi: 10.34133/space.0037. URL https://spj.science.org/doi/abs/10.34133/space.0037.

C. Zhou. Chang'e-5 samples reveal high water content in lunar minerals. nature communications. *Nature communications*, 13(5336), 2022. doi: https://doi.org/10.1038/s41467-022-33095-1.

M. T. Zuber. The moon's gravitational field from lunar prospector and grail. *Icarus*, 281:376–386, 2016.

Appendix | A

Fundamentals of Fluid Dynamics

§A.1 The equation of motion

§A.2 The equation of continuity

§A.3 The equation of energy

§A.4 Derivation of ordinary differential equation

The appendix presents a set of equations that form the foundational principles of fluid dynamics. These equations are essential for understanding the behaviour of fluids and include key concepts such as continuity, momentum conservation, and energy equations. Each equation is discussed in the context of its application and relevance to fluid flow analysis, offering a comprehensive overview of the mathematical framework underlying fluid dynamics.

§A.1 The equation of motion

The basic equation for fluid motion is the well-known Naviér-Stokes equation. Momentum conservation for a fluid can be written as follows:

$$\rho\frac{\partial \mathbf{v}}{\partial t} + \rho\mathbf{v}(\nabla \cdot \mathbf{v}) = -\mathbf{v}(\nabla \cdot \rho\mathbf{v}) - \nabla p - \nabla \cdot \tau + \rho\mathbf{g} \tag{1}$$

§A.2 The equation of continuity

The basic equation for fluid motion is the well-known Naviér-Stokes equation. Momentum conservation for a fluid can be written as follows:

$$\rho\frac{\partial \mathbf{v}}{\partial t} + \rho\mathbf{v}(\nabla \cdot \mathbf{v}) = -\mathbf{v}(\nabla \cdot \rho\mathbf{v}) - \nabla p - \nabla \cdot \tau + \rho\mathbf{g} \tag{2}$$

§A.3 The equation of energy

The general heat equation is given by:

$$\rho C_p\Big(\frac{\partial T}{\partial t} + \mathbf{v} \cdot \nabla T\Big) = k\nabla^2 T - T\alpha\nabla \cdot \mathbf{v} - \tau : \nabla\mathbf{v} \tag{3}$$

§A.4 Derivation of ordinary differential equation

Suppose the density ρ is constant and term $\tau : \nabla\mathbf{v}$ can be neglected. *Note*: for systems with large velocity gradients this term cannot be neglected. Since the density is constant, $d\rho/dt = 0$, which can be substituted in eq. 2:

$$\nabla \cdot \rho\mathbf{v} = 0 \Rightarrow \boxed{\nabla \cdot \mathbf{v} = 0} \tag{4}$$

If above is substituted in equations 3 and 2, the equation of heat and momentum, respectively, becomes:

$$\rho C_p\Big(\frac{\partial T}{\partial t} + \mathbf{v} \cdot \nabla T\Big) = k\nabla^2 T \Rightarrow \boxed{\frac{1}{\alpha}\Big(\frac{\partial T}{\partial t} + \mathbf{v} \cdot \nabla T\Big) = \nabla^2 T} \tag{5}$$

and

$$\rho\frac{\partial \mathbf{v}}{\partial t} = -\nabla p - \nabla \cdot \tau + \rho\mathbf{g} \tag{6}$$

Appendix | B

Modelling and Programming

§B.1 Analytic Functions

§B.2 Ice Deposition Model, 1D

§B.3 Ice Liquefaction Model, 1D

§B.4 Enhancement of thermal conductivity

§B.5 Diffusivity, 2D

§B.6 Sublimation Model, 3D

§B.9 Additional coding

This appendix provides a comprehensive overview of the modelling approaches and programming techniques utilized in this study. The sections detail the development and implementation of various models and computational methods critical to simulating the complex thermal and phase-change behaviours associated with water extraction processes. Each section focuses on a distinct aspect of the modelling work, showcasing analytical methods, 1D and multi-dimensional simulations, and solver strategies.

§B.1 Analytic Functions

Thermal and physical properties are defined as temperature-dependent functions. In this section, these functions are displayed in a well-defined temperature range.
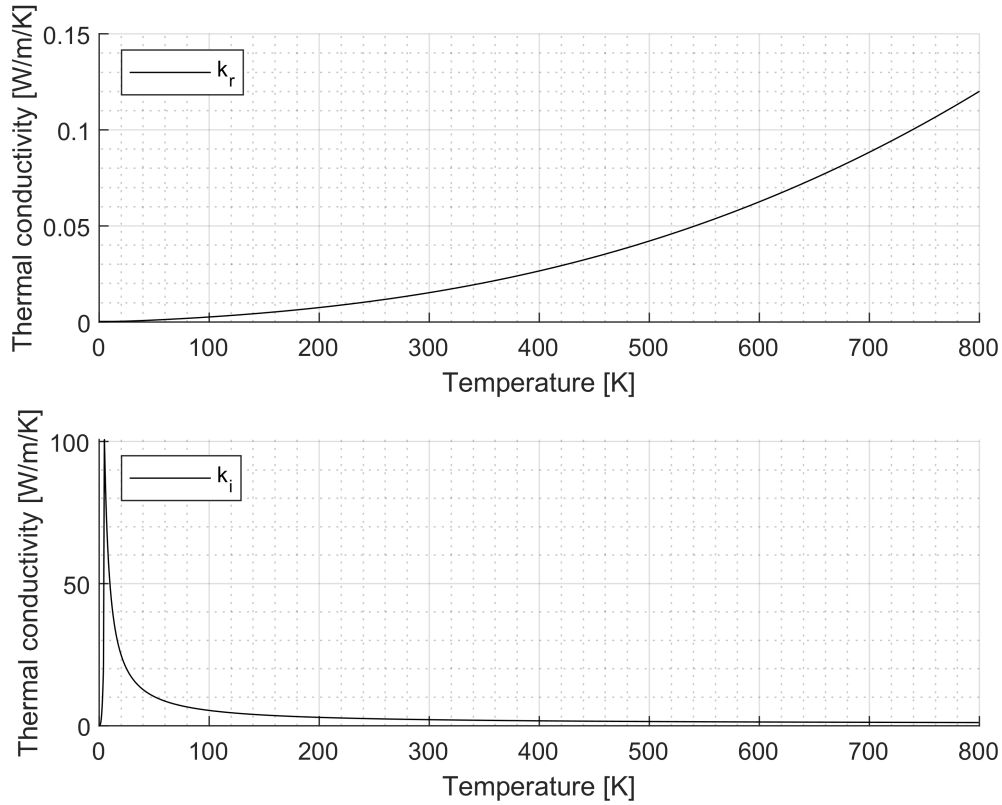

FIGURE 1: 1: Thermal conductivity of regolith with respect to the temperature, adapted from Hab [2022] and further derived to a simplified cubic polynomial:$k_r = 1.03e - 10T^3 + 8.605e - 8T^2 + 1.54e - 5T + 9.09e - 5$, valid for T = [0 800] with residual error < 1e-5; Thermal conductivity of ice with respect to the temperature, defined as: $k_i = 488.19/T + 0.4685$, valid for T = [5 800]

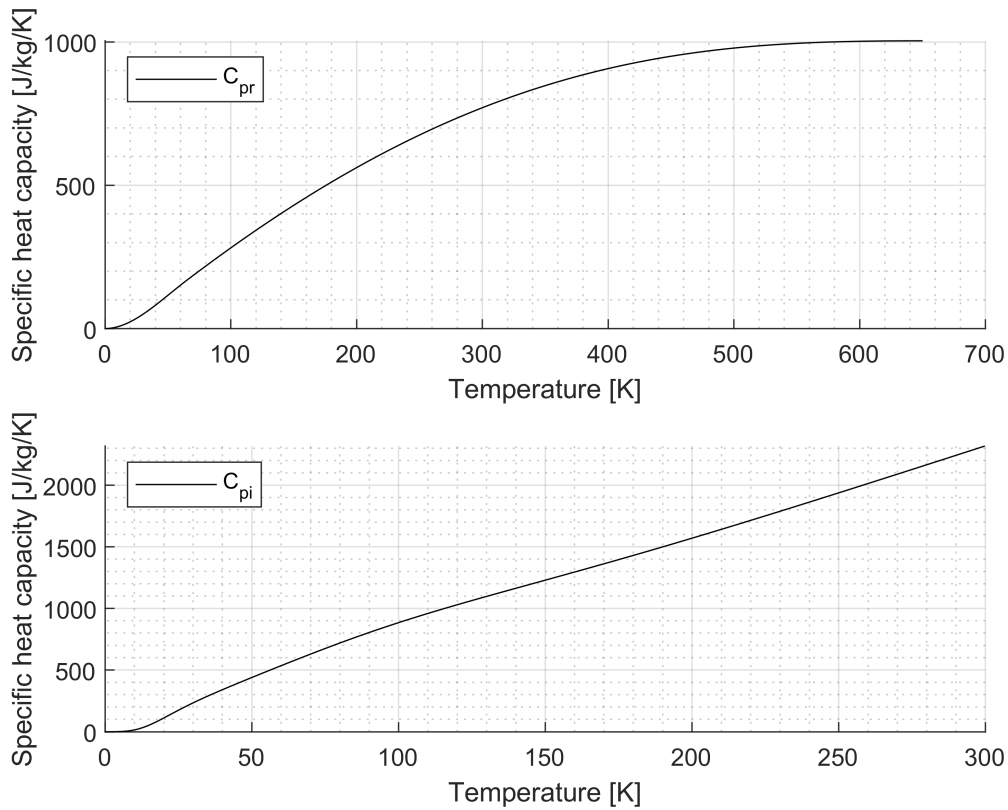FIGURE 2: 1: Specific heat capacity of regolith, adapted from Hab [2022] and further derived to a simplified quadratic polynomial: $C_{pr} = 3.87e - 9T^4 - 4.14e - 6T^3 - 0.0020T^2 + 3.64T - 58.40$, valid for T $= [0.2\ 650]$ 2: Thermal conductivity of ice with respect to the temperature, adapted from Hab [2022] and further simplified to: $C_{pi} = -7.73T(\exp{(-0.0013T^2)} - 1) \cdot 0.0085T^6 \exp{(-3T^{0.5})} + 2.0825e - 7T^4 \exp{(-0.0497T)} + 1$, valid for T $= [0\ 300]$
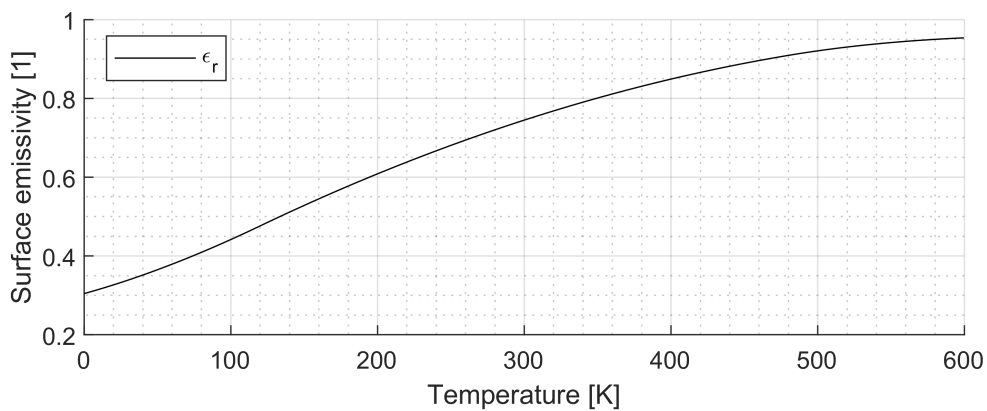

FIGURE 3: Surface emissivity of regolith, adapted from Hab [2022] and defined as: $\epsilon_r = -1.6080e - 6T^2 + 0.0022T + 0.2394$, valid for T $= [40\ 600]$.
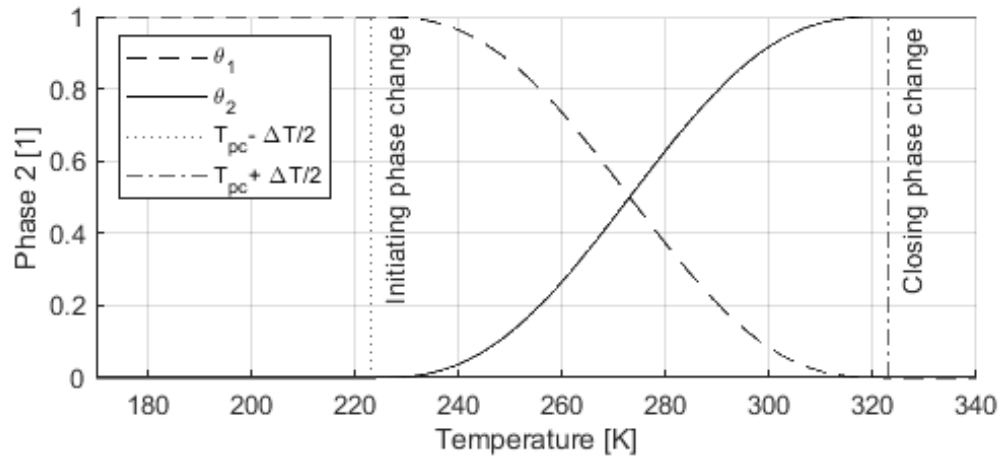
FIGURE 4: Smooth heaviside step function defining the phase transition from phase 1 to phase 2 or $\theta_2 = \alpha_{1 \to 2}$ satisfying $\theta_1 + \theta_2 = 1$; it describes a continuous transition within the transition interval $\Delta T = 100$ K around the phase transition temperature $T_{pc} = 273.15$ K.
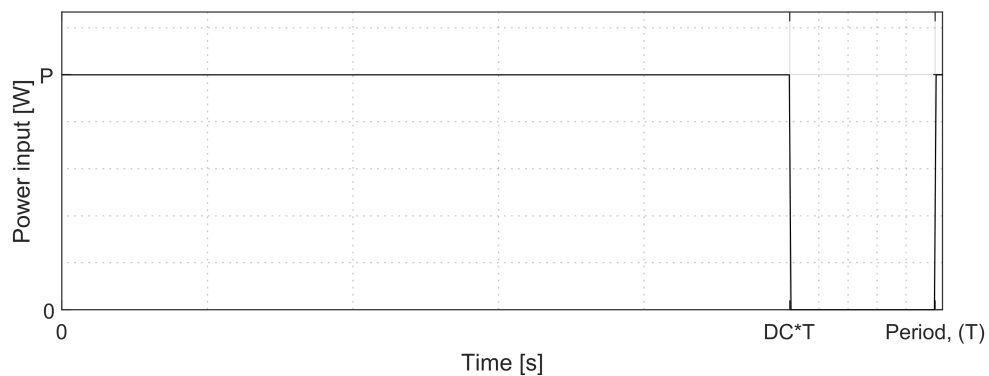

FIGURE 5: Periodic wave form describing the fraction of one period T in which the power signal P is active. Duty cycle (DC) is expressed as a ratio of the pulse width, in which the signal is active, to the period; above is merely an example of a periodic function applying to a system parameter.

§B.2 Ice Deposition Model, 1D

The provided code snippet defines a computational model for simulating phase change processes involving frost and vapour domains. It includes initial temperature calculations for frost and vapour regions, density computations for solid and fluid states, and velocity calculations for phase boundaries. The code sets weak constraints for pressure control (PCI) at various nodes, defines dependent variables like displacement and pressure, and outlines the use of a linear and a non-linear solver with a constant Newton method for iterative convergence, using a damping factor ($\zeta = 0.9$).

§B.3 Ice Liquefaction Model, 1D

In the figure below, the inner copper geometry of the liquefaction chamber is depicted. Only this part of the geometry is covered by heating cables to facilitate the phase transition. To determine the radiative heat flux reaching the ice domain, the view factor is calculated. The view factor is
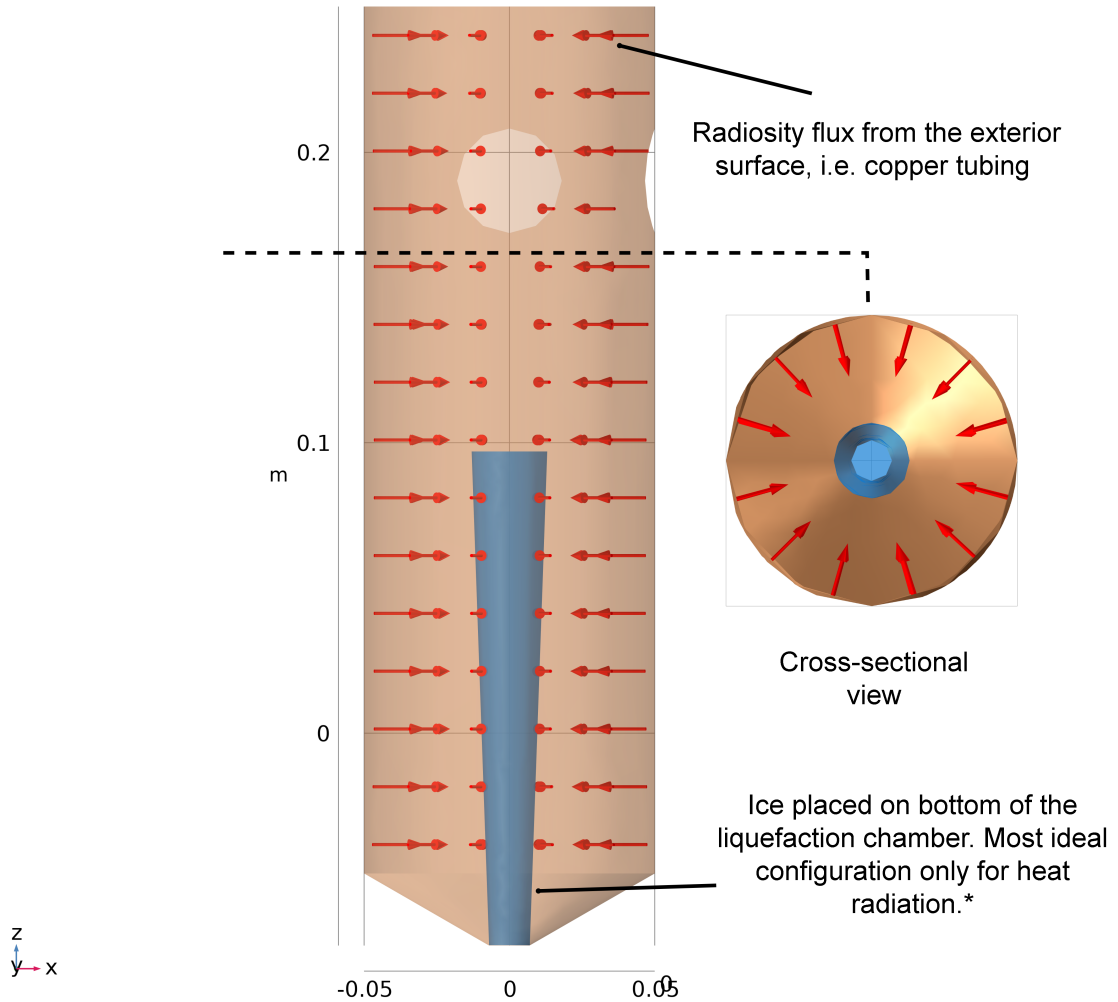

FIGURE 6: Model geometry of the inner liquefaction chamber, with an ice cone placed at the center. *An ideal configuration would have the ice cone directly in contact with the copper tubing to promote heat conduction via contact points.

computed for each evaluation point along the boundaries, which have both an upper and a lower side that can be exposed to radiation. In this model, the liquefaction chamber radiates inward, while the ice radiates outward. The operator I evaluates the mutual surface irradiation based on both the upper and lower surfaces, which are active for all boundaries with surface-to-surface radiation features. The I_u and I_d operators compute the radiative heat flux on the upper and lower surfaces of the boundary, respectively. The expression_upside and expression_downside represent the radiosity expressions for the upper and lower surfaces that irradiate the boundary where the operators are evaluated. To compute the geometric view factor, such as $F_{ext \to int}$, the following integration is defined:

$$F_{ext \to int} = \frac{\int_{S_{int}} I_u(ext, 0)dS}{A_{ext}} \tag{7}$$

Here, S_{int} and S_{ext} represent the interior and exterior surfaces, while A_{int} and A_{ext} are the corresponding surface areas. Integration in the numerator is evaluated over the ice cone, which radiates only from the upper surface. Consequently, $I_d(,)$ is a zero value, simplifying the integrand to $I_u(0, \text{expression\_upside})$. Furthermore, because the outer surface of the liquefaction chamber radiates only from the lower side, it may seem that expression_downside should be ext. However, since the liquefaction chamber is modelled as a 3D solid, radiation from the inner surface on the upper side results in the correct radiative heat flux toward the ice cone. Hence, expression_downside should instead be $I_u(ext, 0)$.

§B.4 Enhancement of thermal conductivity

To represent all the thermal conductivity components in a 3D visualisation, one needs to consider the complete 3x3 thermal conductivity tensor:

$$\mathbf{K} = \begin{pmatrix} k_{xx} & k_{xy} & k_{xz} \\ k_{yx} & k_{yy} & k_{yz} \\ k_{zx} & k_{zy} & k_{zz} \end{pmatrix}$$

and the heat flux tensor:

$$\dot{\mathbf{q}} = \begin{pmatrix} q_{xx} & 0 & 0 \\ 0 & q_{yy} & 0 \\ 0 & 0 & q_{zz} \end{pmatrix}$$

For simplicity, one assumes negligible off-diagonal heat flux values, which reduces computational complexity by approximating these terms as zero. However, for more comprehensive models, such as those involving the Lunar regolith where anisotropic properties could be significant, these terms may need to be accounted for. To derive the heat flux tensor, Fourier's law for heat conduction is applied:

$$\dot{\mathbf{q}} = -\mathbf{K}\nabla T$$

where ∇T is the temperature gradient vector:

$$\nabla T = \begin{pmatrix} \frac{\partial T}{\partial x} \\ \frac{\partial T}{\partial y} \\ \frac{\partial T}{\partial z} \end{pmatrix}$$

Expanding the expression for $\dot{\mathbf{q}}$ yields:

$$\dot{\mathbf{q}} = \begin{pmatrix} \dot{q}_x \\ \dot{q}_y \\ \dot{q}_z \end{pmatrix} = - \begin{pmatrix} k_{xx} & k_{xy} & k_{xz} \\ k_{yx} & k_{yy} & k_{yz} \\ k_{zx} & k_{zy} & k_{zz} \end{pmatrix} \begin{pmatrix} \frac{\partial T}{\partial x} \\ \frac{\partial T}{\partial y} \\ \frac{\partial T}{\partial z} \end{pmatrix}$$

Breaking down each component:

$$\dot{q}_x = -(k_{xx}\frac{\partial T}{\partial x} + k_{xy}\frac{\partial T}{\partial y} + k_{xz}\frac{\partial T}{\partial z})$$

$$\dot{q}_y = -(k_{yx}\frac{\partial T}{\partial x} + k_{yy}\frac{\partial T}{\partial y} + k_{yz}\frac{\partial T}{\partial z})$$

$$\dot{q}_z = -(k_{zx}\frac{\partial T}{\partial x} + k_{zy}\frac{\partial T}{\partial y} + k_{zz}\frac{\partial T}{\partial z})$$

When examining thermal conduction within a 3D volume, such as a sample of Lunar regolith, the thermal conductivity tensor must be integrated over the entire domain to capture the directional dependence of heat transfer. The anisotropic nature of regolith can cause k_{xx}, k_{yy}, and k_{zz} to vary, with cross-terms (k_{xy}, k_{xz}, etc.) indicating interactions between axes. Consider §B.6, which details the 3D Sublimation Model for calculating enhanced effective thermal conductivity k_{eff}. The focus on integrating across vectors of $\mathbf{K}$ allows the study to verify thermal conduction effects and account for rotational influences on the sample. To illustrate the analysis, consider a 3D cube with equal side lengths, represented in Figure 7. This visualisation helps demonstrate how the thermal conductivity is approached by calculating the heat flux $\dot{q}$ and the temperature gradient ∇T between parallel boundaries in all directions. The approach shown in fig. 7 uses a systematic analysis where 64 samples are tested to iteratively calculate the impact of positional variations throughout the sample volume. Each sample is assessed by measuring the heat flux across the cube. This indicates that thermal conductivity calculations are valid across the entire domain of Lunar regolith, ensuring consistency and equivalence in all tensor vectors. This is particularly important given the rotational effects of the sample.
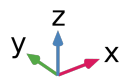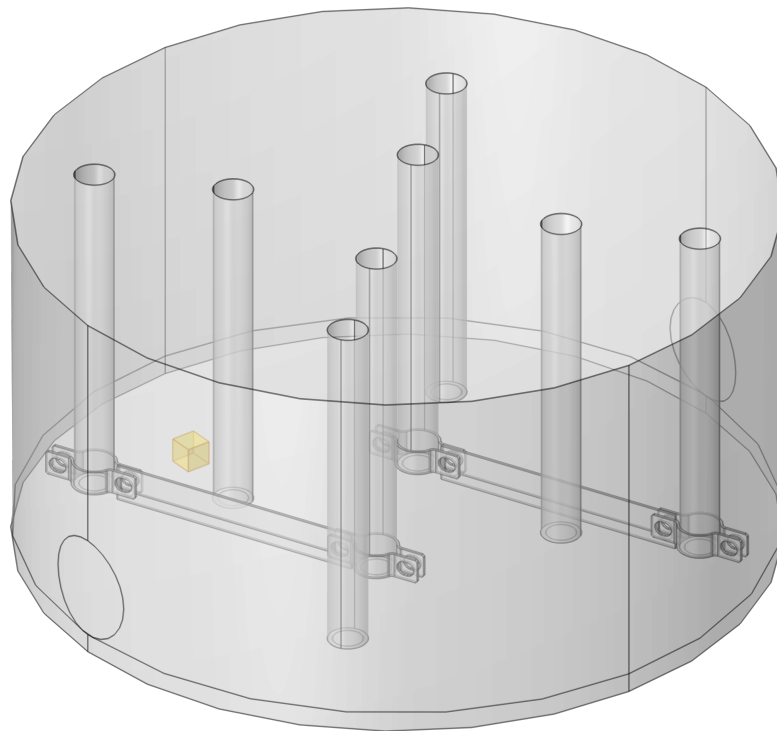
FIGURE 7: Thermal conductivity assessment through heat flux $\dot{q}$ and temperature gradient ∇T calculations between the cube's parallel boundaries; dimensions of the cube are 10x10x10 mm.

§B.5 Diffusivity, 2D

This passage outlines how to evaluate the diffusion coefficient D for free molecular flow within a regolith structure using simulations. The coefficient is calculated based on the molecular flux $\mathbf{J}$ across the boundary Γ and the concentration gradient $\Delta\phi$ between the inlet and outlet:

$$D = \int \mathbf{J} \, d\Gamma \frac{1}{\Delta\phi},$$

where $\Delta\phi$ is the concentration difference, expressed in mol/m^3, derived from flux measurements at the inlet and outlet.

- Geometry and Dimensions: The simulated geometry of the regolith has dimensions $L \times H = 140 \times 70$ microns, with $\Delta x = L$ and $\Delta y = H$.

- Inlet: Located at $x = L$ with a pressure $p = 0.11$ Pa, obtained from the 3D Sublimation Model and related to the section on pressure build-up.

- Outlet: Positioned at $x = 0$, with $p = 0$ to focus on pressure deviation $\Delta\psi$, which is critical for analysing flow behaviour.

- Symmetry: Applied at $y = 0$ and $y = H$, maintaining consistency in boundary conditions.

The diffusion process in free molecular flow depends on precise local pressure and temperature assessments within the pores. This detailed calculation enhances the understanding of transport properties in small-pore structures and informs the overall modelling of molecular diffusion. Figure 8 illustrates the molecular flux distribution across the porous regolith slab. This visualisation, generated through image processing techniques (explained in Appendix B.6), aids in comprehending how flux and concentration gradients behave under specific boundary conditions.
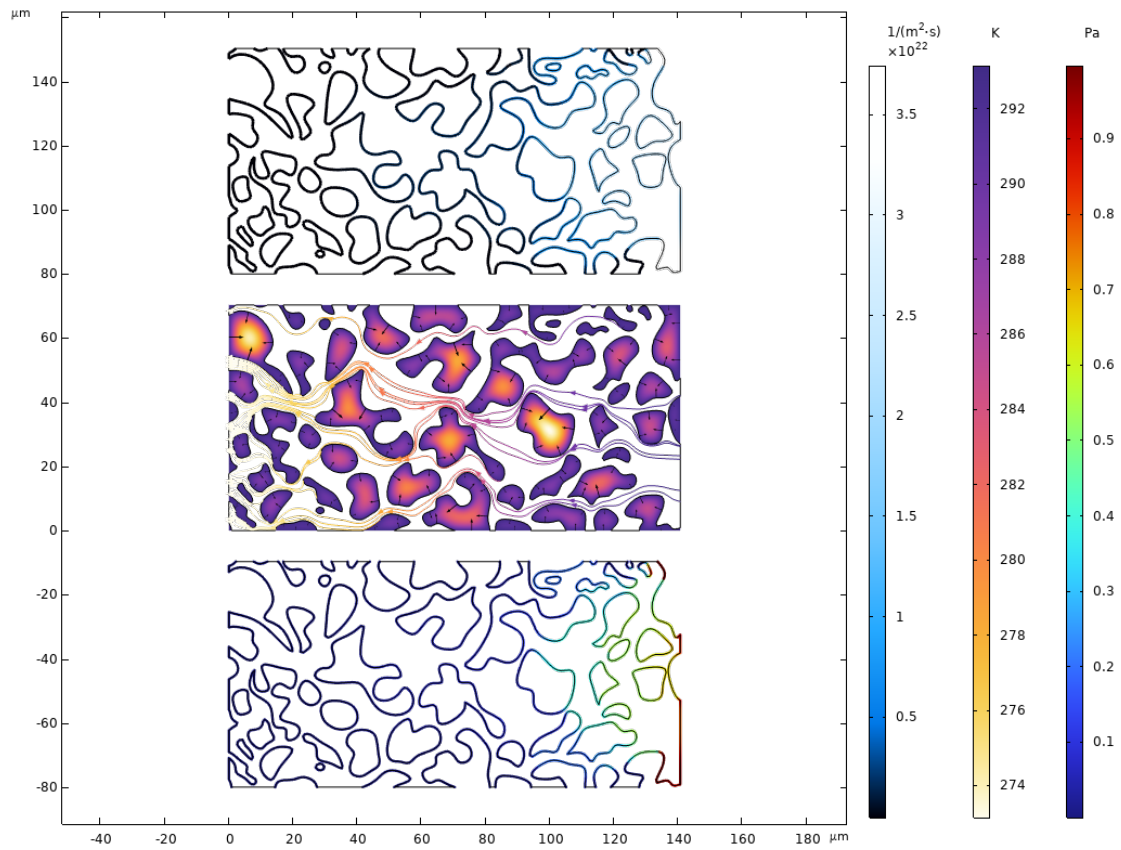
FIGURE 8: A porous slab (140 μm $\times$ 70 μm) of regolith with water vapour flow through mean pore size of 8.59 μm. Image processing in MATLAB was used to calculate this pore size, in alignment with Model I Definition. High molecular flux at the inlet reduces toward the outlet, with flux calculations restricted to boundary regions due to the free molecular flow assumption.

§B.6 Sublimation Model, 3D

The initial step involved developing a two-dimensional model of the regolith-ice mixture, focusing on parameters such as thermal conductivity, heat diffusion rate, and sublimation rate through the cylindrical boundary of the sample. *Note*: The model does not assume that the sample's thickness is significantly larger than its radius, hence $R \sim H_0$, where H_0 represents the initial thickness. This thickness is defined precisely and aligns with 3D model representations. Additionally, the 2D model serves as a basis for exploring the analytical function of the active power signal P, as shown in Fig. 5. The use of 2D modelling is advantageous due to its reduced computational time compared to 3D modelling. For context, a 3D sublimation model, with an analytically active power signal over a duration of $t = 0$ to $t = 40$ hours, would take over five days to compute using a 20 GHz processor running at 99% capacity.

In the 3D sublimation model, the volume shown in fig. 7 represents the icy-regolith mixture. This setup excludes the stirring mechanism, cartridge heaters, crucible housing, and other components depicted in figs. 4.1 and 4.3, which are extruded from the model's volume. Heat is applied to the boundary surfaces of the rods, whose surface area is denoted by A_{rod}. Consequently, only the domain of the icy-regolith mixture remains. The mixture is treated as a fluid to accommodate the phase transition from ice to water vapour. Modelling it as a solid would preclude the simulation of water vapour outgassing. Once the phase change temperature T_{pc} is reached, the water vapour escapes through the regolith's pores, eventually exiting at the top surface (at $z = z_{LVL}$) of the domain.
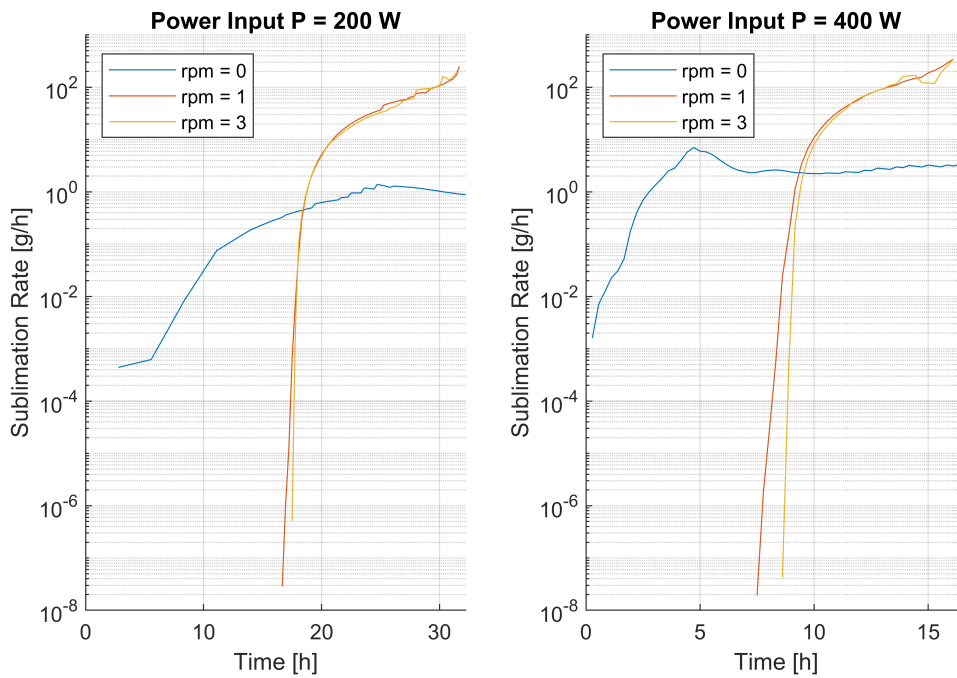

FIGURE 9: Sublimation rates for input power of 200 W and 400 W; the sublimation rate are given on a logarithmic scale to visualise the difference in no rotor and rotor, i.e. rpm = 0 and rpm > 0, respectively.

§B.7 Additional Coding

A porous medium of Lunar regolith can be displayed as below figure. It shows the irregular shapes of the particles including the pores for which a MATLAB code is obtained determining the mean pore size and particle size distribution. This analysis begins with the processing of an
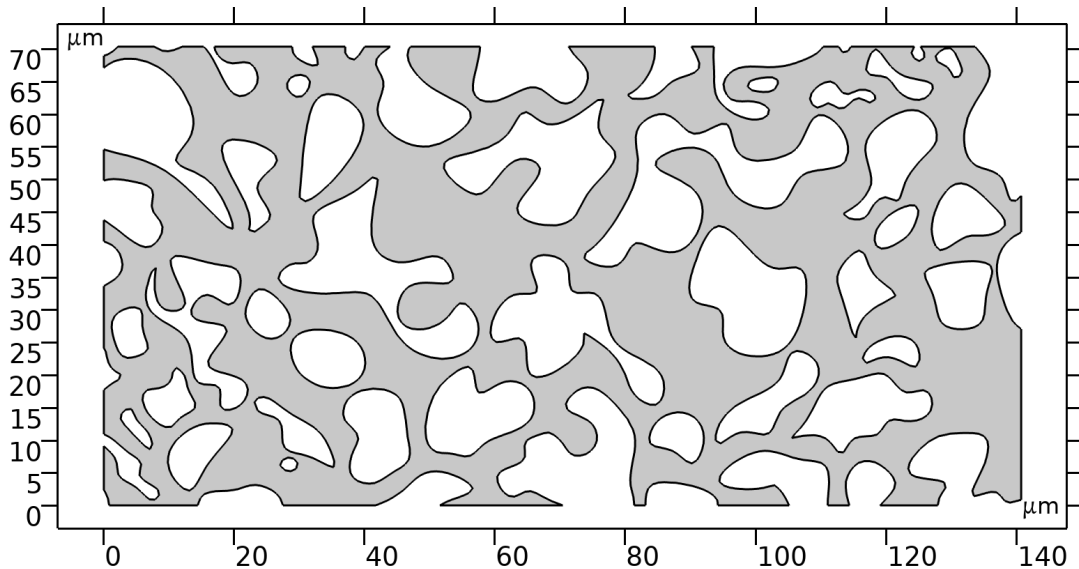

FIGURE 10: Porous medium of Lunar regolith, an example of irregular shaped particles. An image created by [COMSOL Multiphysics®] and adapted to current study; scale in this example is L x H = 140 x 70 μm

image representing a porous material to identify the pore structure and compute the Knudsen number. The process involves several steps including image processing, morphological operations to enhance pore detection, and the calculation of pore size distribution. The Knudsen number is then calculated using two methods based on the mean free path of water vapour in the porous medium.

1. The image is first loaded and, if necessary, converted to grayscale. Then, the 'imbinarize' function is used to convert the grayscale image into a binary image, where white areas represent solid material, and black areas represent pores. To refine the pore detection, morphological operations are applied. Specifically, the image is eroded using a disk-shaped structuring element to separate connected pores and then dilated to restore the original size. S

2. The connected components in the binary image are labelled using 'bwlabel', and the 'regionprops' function is used to extract properties of these labelled regions, including area, equivalent diameter, and centroid. The equivalent diameters of the pores are extracted, and these values are converted from pixels to microns using a pixel-to-real-world conversion factor. The equivalent pore diameters are then used to construct a histogram, showing the particle size distribution. The mean pore size is also calculated as the average of the equivalent diameters.

3. The Knudsen number (Kn) is calculated using two methods based on the mean free path of water vapour molecules, which depends on the properties of the gas and the porous material.

Once the mean free path is calculated using both methods, the Knudsen number is determined by dividing the mean free path by the characteristic pore size d (in microns). This provides insights into the flow regime within the porous medium. For Kn < 1, the flow is typically continuum, while for Kn > 10, the flow is free molecular. The particle size distribution is plotted as a histogram, and the mean pore size is calculated from the extracted pore diameters. The Knudsen numbers are

computed using both the viscosity-based and molecular diameter-based methods. These results characterise the flow regime in the porous material and help determine whether the flow is continuum or free molecular. In conclusion, this analysis successfully identifies and measures the pore
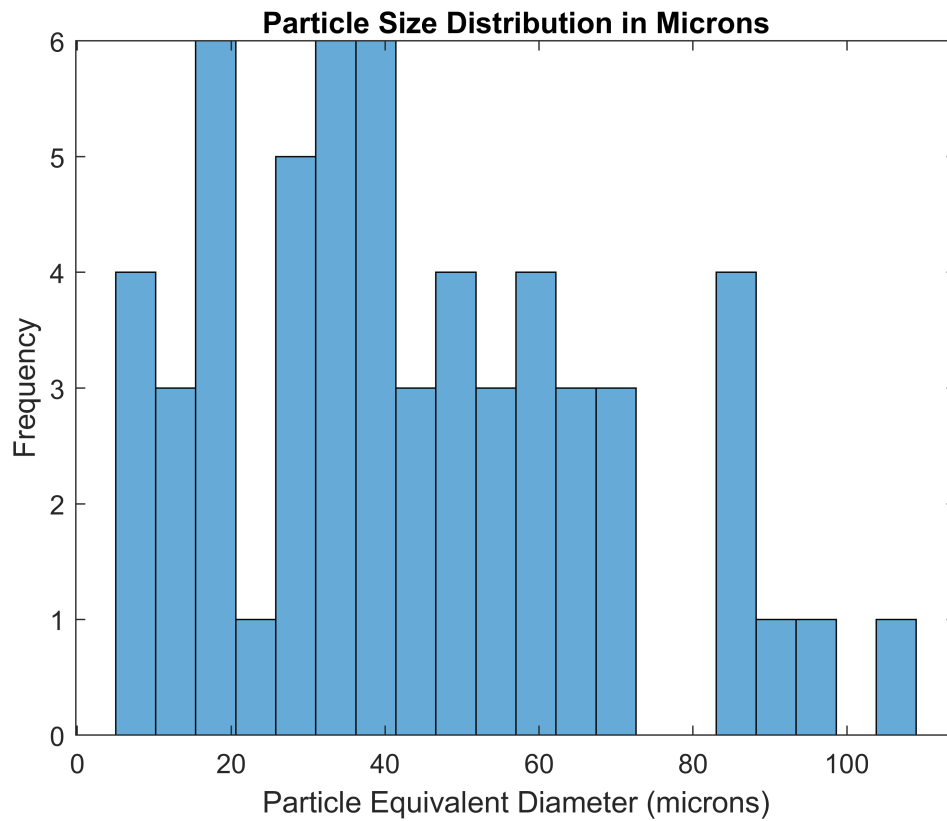

FIGURE 11: The particle size distribution has a mean size of 43.6 μm, while the mean pore size is 423 μm. It is crucial to understand the relationship between the scaling factors $L \times H$ and how they influence the accurate identification and measurement of pore and particle sizes in the regolith.

structure of the material and calculates the Knudsen number, which provides critical information about the flow behaviour in the porous medium.

Appendix | C

Mathematical Topics

§C.1 The Clapeyron–Clausius equation

§C.2 The Interquartile Range Method

§C.3 Curve Fitting

In this appendix we summarise information on mathematical topics (other than vectors and tensors) that are useful in this study.

§C.2 The Interquartile Range Method

Outlier detection is a critical process in data analysis, especially when dealing with experimental data where inaccuracies or anomalies can skew results. In thermal conductivity studies, such as those involving data from COMSOL simulations, it is essential to identify and remove outliers to ensure the accuracy of the calculated thermal properties. The Interquartile Range (IQR) method is a widely used statistical technique for this purpose, offering a robust means of detecting outliers by considering the spread and distribution of the data.

The MATLAB script attached is designed to process thermal conductivity data, detect and remove outliers, and visualise the results to facilitate further analysis. The steps involved include data loading, cleaning, thermal conductivity calculation, outlier detection using the IQR method, and subsequent data visualization:

1. The script begins by loading the thermal conductivity data (k_{xx}, k_{yy}, k_{zz}) and temperature values using the 'ReadData()' function. The data is stored in a matrix format, where each matrix corresponds to a different component of thermal conductivity.

2. The thermal conductivity for each data point is then calculated using the formula:

   $$k_i = \sqrt{k_{xx}^2 + k_{yy}^2 + k_{zz}^2}$$

   This results in a matrix k_i representing the effective thermal conductivity for each temperature point.

3. The first quartile (Q1) and third quartile (Q3) of the thermal conductivity data are calculated using the 'prctile()' function. Q1 represents the 25th percentile, and Q3 represents the 75th percentile of the data.The Interquartile Range (IQR) is computed as the difference between Q3 and Q1:

   $$\text{IQR} = Q3 - Q1$$

4. The lower and upper bounds for outlier detection are calculated using the IQR:

   $$\text{Lower Bound} = Q1 - 1.5 \times \text{IQR}$$

   $$\text{Upper Bound} = Q3 + 1.5 \times \text{IQR}$$

5. Any data points below the lower bound or above the upper bound are classified as outliers.

By applying the IQR method, the script effectively identifies and removes outliers, ensuring that the subsequent analysis of thermal conductivity is based on accurate and reliable data. This process is crucial for maintaining the integrity of experimental results and drawing meaningful conclusions from the data:
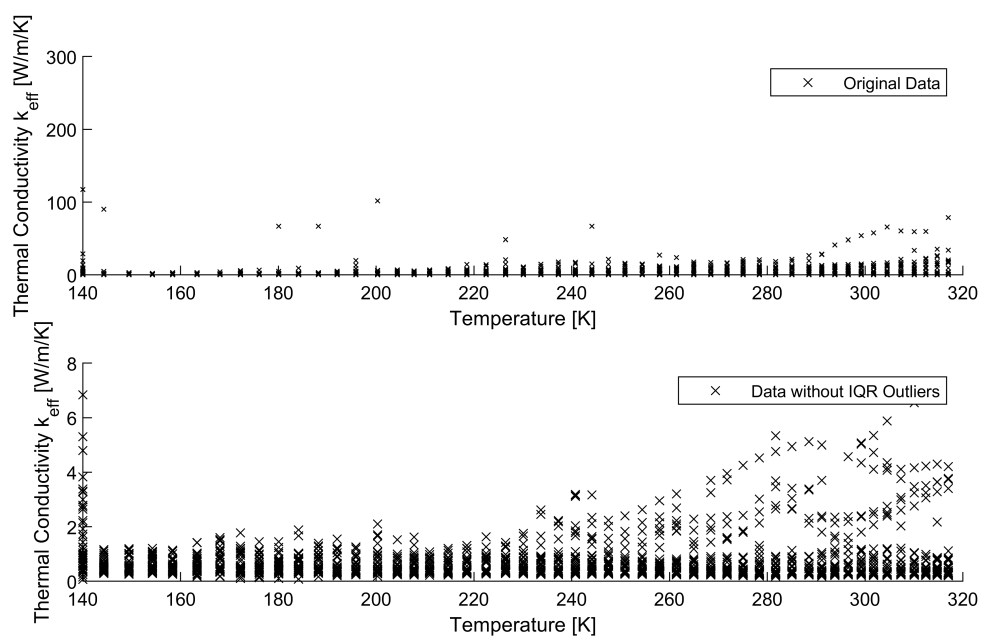
FIGURE 12: Removing the outliers using the IQR method resulting in accurate data analysis.

§C.3 Curve Fitting

The MATLAB script presented here implements a process, focusing on the curve fitting and optimization of thermal conductivity data after outlier removal. The script begins by reading and preparing the data, including the removal of outliers using the Interquartile Range (IQR) method. Subsequently, it performs curve fitting using an optimization routine to determine the parameters that best fit the data. The results, including the original data points, fitted curve, and baseline thermal conductivity, are visualized to provide insights into the thermal behaviour of the material:

1. The script begins by loading and preparing the data using a previously defined 'IQR()' function, which processes thermal conductivity data to remove outliers.

2. Following this, the script identifies and removes columns that contain NaN values, which have resulted from the outlier removal process. The cleaned data matrix is then averaged across the remaining columns to obtain a single vector representing the thermal conductivity at each temperature.

3. The baseline thermal conductivity function, $k_r(T)$, is defined as a polynomial function of temperature T as described in fig. 1.

4. The script proceeds to fit the cleaned thermal conductivity data to a model that includes the baseline function $k_r(T)$ and an additional term representing the contribution of a specific physical process. For clarification, the model is:

$$k_{\text{eff}}(T) = k_r(T) + C \times \rho \times c_p(T) \times \omega \times r^2$$

5. The function **fit_k_eff** performs the optimization to find the best-fit value of C using the 'fminunc' function, which minimises the error between the model's predictions and the measured thermal conductivity data. The optimization process iteratively adjusts C to minimise the sum of squared differences between the fitted and measured values.

6. The specific heat capacity, $C_{pr}(T)$, is modelled as a polynomial function of temperature according to fig. 2.

7. The script calculates the error between the fitted model and the actual measured data using the **compute_k_eff** function. This function computes the fitted thermal conductivity values and then calculates the sum of squared errors as a measure of the fit's accuracy.

The curve fitting and optimization process described in this script is essential for accurately modelling thermal conductivity as a function of temperature. By removing outliers, defining a baseline function, and optimizing the fit of the experimental data to a theoretical model, the script ensures that the derived parameters, such as the fitting constant C, are reliable of the thermal properties of regolith.